

# Hierarchical Coordinated Fast Frequency Control using Inverter-Based Resources for Next-Generation Power Grids

by

Etinosa Ekomwenrenren

A thesis  
presented to the University of Waterloo  
in fulfillment of the  
thesis requirement for the degree of  
Doctor of Philosophy  
in  
Electrical and Computer Engineering

Waterloo, Ontario, Canada, 2023

© Etinosa Ekomwenrenren 2023

## Examining Committee Membership

The following served on the Examining Committee for this thesis. The decision of the Examining Committee is by majority vote.

External Examiner:       Sairaj Dhople  
                                  Professor,  
                                  Dept. of Electrical and Computer Engineering,  
                                  University of Minnesota

Supervisor(s):             John W. Simpson-Porco  
                                  Professor,  
                                  Dept. of Electrical and Computer Engineering,  
                                  University of Toronto

Internal Member:         Claudio Canizares  
                                  Professor,  
                                  Dept. of Electrical and Computer Engineering,  
                                  University of Waterloo

Internal Member:         Michael Fisher  
                                  Professor,  
                                  Dept. of Electrical and Computer Engineering,  
                                  University of Waterloo

Internal-External Member: Jatin Nathwani  
                                  Professor,  
                                  Dept. of Civil and Environmental Engineering,  
                                  University of Waterloo

### **Author's Declaration**

I hereby declare that I am the sole author of this thesis. This is a true copy of the thesis, including any required final revisions, as accepted by my examiners.

I understand that my thesis may be made electronically available to the public.

## Abstract

The proportion of inverter-connected renewable energy resources (RES) in the grid is expanding, primarily displacing conventional synchronous generators. This shift significantly impacts the objective of maintaining grid stability and reliable operations. The increased penetration of RESs contributes to the variability of active power supply and a decrease in the rotational inertia of the grid, resulting in faster system dynamics and larger, more frequent frequency events.

These emerging challenges could make traditional centralized frequency control strategies ineffective, necessitating the adoption of modern, high-bandwidth control schemes. In this thesis, we propose a novel hierarchical and coordinated real-time frequency control scheme. It leverages advancements in grid monitoring and communication infrastructure to employ local, flexible inverter-based resources for promptly correcting power imbalances in the system. We solve two research problems that, when combined, yield a practical, real-time, next-generation frequency control scheme. This scheme blends localized control with high-bandwidth wide-area coordination.

For the first problem, we propose a layered architecture where control, estimation, and optimization tasks are efficiently aggregated and decentralized across the system. This layered control structure, comprising decentralized, distributed, and centralized assets, enables fast, localized control responses to local power imbalances, integrated with wide-area coordination.

For the second problem, we propose a data-driven extension to the framework to enhance model flexibility. Achieving high accuracy in system models used for control design is a considerable challenge due to the increasing scale, complexity, and evolving dynamics of the power system. In our proposed approach, we leverage collected data to provide direct data-driven controller designs for fast frequency regulation.

The devised scheme ensures swift and effective frequency control for the bulk grid by accurately re-dispatching inverter-based resources (IBRs) to compensate for unmeasured net-load changes. These changes are computed in real-time using frequency and area tie power flow measurements, alongside collected historical data, thus eliminating reliance on proprietary power system models. Validated through detailed simulations under various scenarios such as load increase, generation trips, and three-phase faults, the scheme is practical, provides rapid, localized frequency control, safeguards data privacy, and eliminates the need for system models of the increasingly complex power system.

## Acknowledgements

I wish to express my profound gratitude to my supervisor, Professor John Simpson-Porco, for his exceptional mentorship and unwavering support throughout my research journey.

I extend my sincere appreciation to my Ph.D. Committee members for their valuable insights and recommendations: Professors Claudio Canizares and Michael Fisher from the Department of Electrical and Computer Engineering at the University of Waterloo; Professor Jatin Nathwani from the Department of Civil and Environmental Engineering at the same university; and Professor Sairaj Dhople from the Department of Electrical, Computer, and Energy Engineering at the University of Minnesota.

I am also indebted to Professor Christopher Nielsen from the Department of Electrical and Computer Engineering at the University of Waterloo, and Professor Baris Fidan from the Department of Mechanical and Mechatronics Engineering at the same university. Their insightful comments and suggestions meaningfully enriched my research.

I am grateful for the financial support received from the Queen Elizabeth II Graduate Scholarship in Science and Technology (QEII-GSST) and the Electric Power Research Institute (EPRI) under project No. 10009168: Wide-Area Hierarchical Frequency and Voltage Control for Next Generation Transmission Grids Natural Sciences and Engineering. My gratitude also extends to Evangelos Farantatos, Mahendra Patel, Aboutaleb Haddadi, and Lin Zhu from EPRI, and Hossein Hooshyar from the New York Power Authority (NYPA). The opportunity to work with these esteemed professionals and their invaluable advice considerably enhanced my research experience.

Lastly, I would like to offer special thanks to my friends, Zhiyuan Tang and Illyas Farhat, for their unwavering support and encouragement.

## **Dedication**

This is dedicated to my parents, in recognition of their tireless efforts and steadfast support.

# Table of Contents

Examining Committee	ii
Author's Declaration	iii
Abstract	iv
Acknowledgements	v
Dedication	vi
List of Figures	x
List of Tables	xii
<b>1 Introduction</b>	<b>1</b>
1.1 Motivation . . . . .	1
1.2 Research Objectives . . . . .	2
1.3 Contributions . . . . .	3
1.3.1 Contribution #1: Hierarchical Fast Frequency Control Architecture for Transmission Systems . . . . .	4
1.3.2 Contribution #2: Data-Driven Extension to Hierarchical Coordinated Fast Frequency Control Framework . . . . .	5
1.4 Related Contributions . . . . .	6
1.5 Thesis Outline . . . . .	6

<b>2</b>	<b>Background and Literature Review</b>	<b>8</b>
2.1	Frequency Control (Regulation) in Power Systems . . . . .	8
2.2	Overview of Inverter-Based Resources in Frequency Regulation . . . . .	10
2.3	Hierarchical Coordinated Fast Frequency Control for Transmission Systems	11
2.4	Data-Driven Extension to Hierarchical Coordinated Fast Frequency Control Framework . . . . .	14
<b>3</b>	<b>Hierarchical Coordinated Fast Frequency Control using Inverter-Based Resources</b>	<b>16</b>
3.1	Introduction . . . . .	17
3.2	An Internal Model Control Approach for Local Area-Based Frequency Control	17
3.2.1	Local Disturbance Estimator for the LCA . . . . .	19
3.2.2	System Frequency Response LCA Modelling . . . . .	22
3.2.3	Nominal Stability and Perfect Disturbance Rejection . . . . .	22
3.3	Mathematical Formulation for Optimal Power Allocation . . . . .	24
3.3.1	Stage 1: Local Redispatch of IBRs . . . . .	25
3.3.2	Stage 2: Coordination Layer for Inter-Area IBR Response . . . . .	25
3.3.3	Privacy-Preserving Distributed Implementation of Stage 2 . . . . .	26
3.4	Simulation Studies . . . . .	28
3.4.1	Scenario #1: Disturbance with Sufficient Local Resources . . . . .	31
3.4.2	Scenario #2: Disturbance with Insufficient Local Resources . . . . .	33
3.4.3	Scenario #3: Symmetric Three-Phase Fault . . . . .	34
3.4.4	Scenario #4: Loss of Generator . . . . .	35
3.4.5	Scenario #5: Parameter Variation . . . . .	36
3.4.6	Scenario #6: Coordination of IBRs and Conventional Generators . . . . .	38
3.4.7	Scenario #7: Test on Larger Power System . . . . .	38
3.5	Summary . . . . .	41

<b>4</b>	<b>Data-Driven Extension to Hierarchical Coordinated Fast Frequency Control Framework</b>	<b>43</b>
4.1	A Data-Driven Control Approach for Area-Based Fast Frequency Control . . . . .	43
4.1.1	Brief Background on Data-Driven System Representation . . . . .	44
4.1.2	Design #1: Linear Data-Driven Disturbance Estimator . . . . .	45
4.1.3	Design #2: Optimization-Based Data-Driven Disturbance Estimator	48
4.1.4	Specialization to Area-Based Fast Frequency Control using Inverter-Based Resources . . . . .	49
4.2	Simulation Studies . . . . .	50
4.2.1	Offline Data Collection and Controller Tuning . . . . .	52
4.2.2	Simulation Scenarios . . . . .	53
4.2.3	Scenario #1: Step Load Changes . . . . .	54
4.2.4	Scenario #2: High Renewable Resource Fluctuations . . . . .	57
4.2.5	Scenario #3: Symmetric Three-Phase Fault . . . . .	58
4.2.6	Scenario #4: Loss of Generator . . . . .	61
4.3	Summary . . . . .	62
<b>5</b>	<b>Conclusion</b>	<b>64</b>
5.1	Summary . . . . .	64
5.2	Future Research Directions . . . . .	66
	<b>References</b>	<b>68</b>
	<b>APPENDICES</b>	<b>78</b>
<b>A</b>	<b>Proofs</b>	<b>79</b>
A.1	Proofs From Section 3 . . . . .	79
A.2	Proofs From Section 4 . . . . .	82
<b>B</b>	<b>Illustrative Example of Allocation Based on Electrical Distance</b>	<b>84</b>

# List of Figures

3.1	Cyber-physical system illustrating frequency control approach. . . . .	18
3.2	Block diagram of area control structure for each LCA. Black dashed lines denote sampled signals. . . . .	19
3.3	Response to 63 MW load change at bus 8; the IBR power plots correspond to the case of 300ms delay. . . . .	31
3.4	Tie-line power flow deviations following a 63 MW load change at bus 8 in area two. . . . .	32
3.5	Response to 130 MW load change at bus 8. . . . .	33
3.6	Plot of net tie-line flows following a 130 MW load change at bus 8. . . . .	33
3.7	Frequency response to three-phase fault. . . . .	34
3.8	Plots of load estimate and IBR outputs following a three-phase line-to-ground fault at bus 8 in area 2. . . . .	35
3.9	Response to loss of generator G2. . . . .	36
3.10	Response with variations in model parameters. . . . .	37
3.11	Response to 63MW load change at bus 8 with redispatch of both SGs and IBRs. . . . .	38
3.12	Plot of net tie-line flows following a 63 MW load change at bus 8 with redispatch of both SGs and IBRs. . . . .	39
3.13	5-area 68-bus test system. . . . .	39
3.14	Response to 300 MW load change at bus 33. . . . .	40
3.15	Plot of net tie-line flows following a 300 MW load change at bus 33. . . . .	40
3.16	Response to 450 MW load change at bus 33. . . . .	41

3.17	Plot of net tie-line flows following a 450 MW load change at bus 33. . . . .	42
4.1	Three-LCA test system. . . . .	51
4.2	Persistently exciting IBR set-point change for data collection phase. . . . .	53
4.3	Frequency and disturbance estimate during a 14 MW load change at bus 8 in Area 2. . . . .	55
4.4	Zoomed-in frequency plot of the contingent area showing the control alternatives during a 14 MW load change at bus 8 in Area 2. . . . .	55
4.5	Tie-line deviation and active power profiles during a 14 MW load change; dashed lines in the lower plots indicate the responses under model-based estimation. . . . .	56
4.6	Frequency and disturbance estimate during a 60 MW load change at bus 8 in Area 2. . . . .	56
4.7	Zoomed-in frequency plot of the contingent area showing the control alternatives during a 60 MW load change at bus 8 in Area 2. . . . .	57
4.8	Tie-line deviation and active power profiles during a 60 MW load change; dashed lines in the lower plots indicate the responses under model-based estimation. . . . .	58
4.9	Solar irradiance and wind power data representing suitably scaled slices of data on 31 July 2010 and 15 Aug 2019 from [1] and [2] repositories. . . . .	59
4.10	Frequency and disturbance estimate during high renewable resource fluctuations in multiple areas. . . . .	59
4.11	Zoomed-in frequency plot during high renewable resource fluctuations in multiple areas. . . . .	60
4.12	Tie-line deviation and active power profiles during high renewable resource fluctuations in multiple areas.; dashed lines in the lower plots indicate the responses under model-based estimation. . . . .	60
4.13	Frequency and disturbance estimate during a three-phase fault in Area 2. . . . .	61
4.14	Tie-line deviation and active power profiles during a three- phrase fault in Area 2; dashed lines in the lower plots indicate the responses under model-based estimation. . . . .	62
4.15	Frequency and disturbance estimate during a generator G4 loss in Area 3. . . . .	63

# List of Tables

3.1	Tie-line parameters for 3-area system; 100 megavolts ampere (MVA) base.	29
3.2	Generator and IBR Data. . . . .	29
3.3	SFR model parameters for LCA estimator design. . . . .	30
3.4	SFR model parameters for Scenario #5. . . . .	37
4.1	Root Mean Square Error for Control Alternatives. . . . .	61





# Chapter 1

## Introduction

### 1.1 Motivation

The grid is changing and conventional monitoring and control paradigms will, necessarily, have to evolve too. The major drivers of this modernization are the need to decarbonize the power sector, enhance grid visibility, and improve operational efficiency.

Spurred by climate change concerns, the world is moving towards a low-carbon future, and countries have set ambitious climate change targets in order to limit the global temperature rise [3]. Decarbonizing the power sector is essential in meeting these climate change goals and requires raising the share of renewables in the world's primary energy supply from the current 15% to 65% [4]. The increasing penetration of these intermittent and variable renewable energy sources (RES, mostly inverted-connected wind and solar plants), which are mostly displacing fossil-fuel-powered conventional synchronous generators, is significantly affecting the goal of maintaining grid stability and reliable operations.

Additionally, the present grid lacks visibility, with the unavailability of real-time high resolution information necessary to make critical decisions hampering situational awareness and resulting in blackouts [5]. Improving grid visibility will require advances in remote sensing with the use of global positioning system (GPS) synchronized phasor measurements units (PMUs) in the transmission grids[6] and Smart Meters (SMs) and Remote Terminal Units (RTUs) on the customer-facing side [7].

Furthermore, the current grid has inefficient power storage resulting in the real-time matching of supply with demand, leading to high strain on the infrastructure during peak demand hours and the need for an increasingly fast ramp up of generation [8]. Remedying

this will require the integration of energy storage and improvements in the ability of utilities to adjust customer’s load demands along with finer control over distributed energy resources.

The increasing penetration of RESs coupled with real-time power demand and supply matching and lack of grid visibility bring new challenges to traditional frequency control strategies. These challenges include increased variability of active power supply, reduced overall inertia, and increased spatial heterogeneity of inertia, leading to faster system frequency dynamics along with larger and more frequent frequency control events [9, 10, 11, 12].

These aforementioned challenges may render conventional frequency control strategies ineffective, necessitating the use of modern, high-bandwidth control schemes. These high-bandwidth control schemes will become increasingly feasible as the grid modernizes, with communication infrastructure playing a dominant role [6, 13]. Advances in remote communication and sensing with the use of global positioning system (GPS) synchronized phasor measurements units (PMUs) will allow for improved monitoring and protection [6], enabling fast control actions using IBRs to quickly compensate disturbances [13].

In order to fully leverage these technologies, however, power system control will need to evolve away from the conventional centralized paradigm. The next-generation grid will contain large numbers of geographically dispersed sensors and actuators that need to be coordinated in a fast and reliable way, while maintaining data privacy of the multiple actors involved. Additionally, with the increased integration of information and communication technology, the cyber-physical system will be vulnerable to cyber-attacks, which will be exacerbated by a centralized control architecture with only a single point of failure. These issues highlight the shortcomings of the centralized paradigm. In this work, we propose a novel hierarchical coordinated real-time frequency control scheme that exploits these improvements in modern grid monitoring and communication infrastructure by utilizing local, flexible inverter-based resources to quickly correct power imbalances arising in the system.

## 1.2 Research Objectives

The primary objective of this work is to design and validate a next-generation frequency control scheme. This scheme would feature decentralized actors granted authority within smaller, defined regions of the broader transmission system. Such a system requires a hierarchical architecture that decentralizes control and optimization authority further while integrating new sensors and actuators.

The design must also incorporate built-in model flexibility, minimizing the quantity and the quality of the required system model information. This is crucial because ensuring high accuracy in the system model is a significant challenge due to the increasing scale, complexity, and changing dynamics of the power system. Furthermore, the scheme needs to address emerging issues resulting from the heightened penetration of renewable energy resources, such as increased spatial heterogeneity of inertia.

These key attributes lead us to the main research objectives of this work, which we will explore in more detail below.

1. **Hierarchical architecture:** In modern grids, sensing ability and control authority is dispersed over many more devices than in the past, making decentralization important in managing the information flows. In this work, we seek a layered architecture wherein control, estimation, and optimization tasks are aggregated and decentralized across the system efficiently. The candidate layered control architecture would provide for fast, localized control in response to local power imbalances with wide-area coordination and would consist of decentralized, distributed, and centralized assets. The layered architecture results in greater flexibility in designing the constituent layers, while the local handling of information allows for faster speed and efficiency of control response, greater data privacy, reduced latency and communication payload, and reduced vulnerability to cyber-attacks.
2. **Data-driven modelling:** As mentioned earlier, due to the increasing complexity and scale of the power system, it is very difficult to obtain sufficiently accurate system models for control design. Hence, there is a need to minimize the amount of model information required for design purposes. In this work, in order to overcome this obstacle, we will pursue a data-driven control framework, whereby measured data is used in place of any explicit model in our designs. This will improve the adaptability of the design to realistic system conditions, resulting in faster control actions together with a reduction in the incidence of parameter tuning.

The research objectives above are complementary and can be combined to provide a practical, real-time next-generation frequency control scheme.

## 1.3 Contributions

Based on the research objectives discussed in Section 1.2, we outline our main contributions in this work.

### 1.3.1 Contribution #1: Hierarchical Fast Frequency Control Architecture for Transmission Systems

In the first part of this work, we propose a layered control architecture, consisting of decentralized, distributed, and centralized asset control, whereby the bulk electricity transmission system is partitioned into geographically small (e.g., several substations) local control areas (LCAs), within which high-bandwidth low-latency measurements are available for local decision making. Within each LCA, a *disturbance estimator* processes frequency and area tie power flow measurements (using a dynamic model of the LCA) in order to detect frequency events. The estimator generates a real-time estimate of the net unmeasured active power imbalance within the LCA, and an allocation mechanism optimally redispatches local IBRs to correct the imbalance. In situations where local resources are insufficient, a higher-level coordinating controller facilitates the provision of additional power support from neighboring LCAs. In Section 3.4, our results are extensively validated via simulations on two detailed power system models; several scenarios are examined, including load increases, generation trips, and three-phase faults.

The novelty of our methodology lies in the rapid and accurate re-dispatch of fast IBRs to compensate unmeasured net-load changes, and in the layered control architecture, which enables fast, localized control in response to local power imbalances with supplementary wide-area coordination. This hierarchical architecture provides flexibility in designing the constituent layers, while local handling of information allows for faster speed and efficiency of control response. Our scheme has the following appealing characteristics:

1. *Practicality*: the design for each LCA is based only on a simple aggregated area model, although the designer is free to incorporate a more detailed model if one is available. This is advantageous, since owing to the increasing power system scale, complexity and changing dynamics, ensuring the accuracy of complex system models is a major challenge in practice. All controller computations are either linear update rules or small, simple optimization problems. Furthermore, due to the robustness against model uncertainty provided by the feedback configuration, the scheme affords the designer a large margin of error in the accuracy of this model, which is indispensable in practice as even lumped parameters can be difficult to estimate; see Section 3.4.5. Finally, the design can be retrofit onto existing systems.
2. *Localized and fast control*: The local control loops take into account local communication delays, inertia, and primary frequency response characteristics, and use only local measurements of frequency and line power flows. An upshot of this localized use of measurements is the minimization of latency. This use of local measurements

together with the more granular partitioning of the system, allows for the quick localization of net power imbalance and redispatch of fast-acting IBRs for its correction, resulting in fast frequency regulation.

3. *Multi-area data privacy*: Potentially sensitive information such as device limits, set-points, and available spare capacity of resources in an LCA are not shared with either the central controller or the neighboring LCAs. Furthermore, computation of control actions for the additional power adjustments are done *within* each LCA (3.14), with the central controller providing minimal coordination between LCAs.

### 1.3.2 Contribution #2: Data-Driven Extension to Hierarchical Coordinated Fast Frequency Control Framework

For the initial development of the LCAs in the first part of this work, we consider a simplified, low-order dynamic model for the controller designs. The model is parameterized by several coefficients (such as total inertia, total primary response, and damping constants), which can be updated in an online fashion if needed. This modeling choice is made based on the assumption that reliable and highly accurate system models would be too difficult to obtain in practice.

Unfortunately, despite these efforts to minimize the amount and quality of system model information required, it may be the case that accurate parameter values for use in the models cannot be easily obtained in practice with reasonable effort, or cannot be accurately updated as system conditions change. Therefore, in the later part of this work, we provide direct data-driven controller designs which enable the IBRs to participate in providing geographically localized fast frequency control. The key components in our approach are novel designs for *data-driven disturbance estimators*: dynamic algorithms which provide online estimates of the net real power imbalance within a specified control area. Local IBRs are then quickly redispatched within their operating limits to eliminate the imbalance.

In Section 4.1 we present two data-driven disturbance estimator designs. Both designs are based directly on recorded system data, and do not require a parametric system model. The two designs trade off between simplicity and robustness/performance. The first design uses a simple linear update law to estimate the disturbance, and requires tuning of only a single parameter; we provide theoretical guarantees supporting this design. The first design serves as a stepping stone to our second approach, which is an optimization-based estimation procedure. The second design has a higher computational burden, requiring

the solution of a convex optimization problem at each time-step, but (i) is less sensitive to noise in the recorded data, (ii) is less sensitive to strong nonlinearity in the system dynamics (e.g., governor deadbands), and (iii) shows superior performance in simulation studies. As the formulations are general, we outline specifically how these methods are applied to the frequency control problem under consideration. Compared, for instance, to the recent data-driven load-frequency controller proposed in [14], we do not make the strong assumption that a measurement of net load demand is available; our approach is based only on direct measurements of area frequency and net power flow out of the control area.

In Section 4.2, we extensively validate our designs via simulations on a detailed non-linear three-area power system. Several scenarios are examined, including load increases, heavy renewable penetration, generation trips, and three-phase faults. The tests demonstrate that our approach provides fast and effective frequency control for the bulk grid, and even outperforms our model-based design in Section 3.

## 1.4 Related Contributions

In references [15, 16], we proposed a measurement-based voltage controller and validated it through comprehensive simulations. This controller coordinates fast-acting inverter-based resources (IBRs) and other traditional power sources to prevent voltage violations and maintain voltages within the desired limits in grids dominated by IBRs. Like the frequency control architecture mentioned above, this scheme also takes advantage of the recent advancements in wide-area communication and monitoring by employing real-time, measurement-based feedback control.

In [17], we outlined detailed integration procedures to combine the novel frequency controller discussed in this thesis with the voltage controller proposed in references [15, 16] into a unified control framework. This integration approach allows both controllers to utilize IBRs simultaneously with minimal conflict and adverse interactions.

## 1.5 Thesis Outline

The remainder of this thesis is organized as follows. Chapter 2 presents a brief background and literature review related to the research objectives. In Chapter 3, we present our novel hierarchical fast frequency control scheme, which uses a simplified dynamic model of each

LCA for controller design purposes. We then provide a data-driven extension to the scheme in Chapter 4. Finally, Chapter 5 concludes the work, providing a summary of the work undertaken in this thesis and outlining possible future research directions.

# Chapter 2

## Background and Literature Review

Motivated by environmental concerns, the share of renewable energy resources (mostly inverted-connected wind and solar plants) in the transmission grid is currently rising. However, this poses significant technical challenges to the goal of maintaining grid stability and operational constraints. First, the intermittency and variability of renewable generation can result in increased net load variability in the system [18]. Additionally, RES are displacing traditional synchronous generators from the power grid, along with the stored kinetic energy they provide through inertia. The ensuing reduction in the system rotational inertia can significantly impact power system operation and stability, resulting in large frequency deviations, faster frequency dynamics, and heterogeneous inertia distribution throughout the system [9, 10, 11, 12]. Low-inertia stability issues are now manifesting in the real world; for example, the increasing penetration of inverter-connected RES has been blamed for the recent power system blackout in South Australia [19].

Therefore, to maintain and improve the functionality and operation of the power system in this more uncertain environment, critical services such as automatic control, estimation, and optimization systems must be fast and localized, and be increasingly geographically coordinated using high-bandwidth communications. In what follows, we provide a brief review of relevant literature for frequency control in transmission grids and discuss some works relevant to the research problems being considered in this Ph.D. research.

### 2.1 Frequency Control (Regulation) in Power Systems

Our contemporary electrical grid operates on the principle of real-time energy generation aligning with real-time consumer demand, as there is limited practical energy storage

currently available [20]. Central to this power system is the production of electricity at a stable, synchronized Alternating Current (AC) frequency, measured in cycles per second, or Hertz (Hz). This specific frequency, referred to as the nominal frequency, is vital to the smooth operation of the power grid. Failure to maintain this nominal frequency can lead to damaging outcomes such as equipment damage and, in worst-case scenarios, a full-scale power system collapse [21].

The maintenance of this system frequency, a critical aspect of power system stability, is typically managed using a blend of inertia response and automatic control [22]. Generators in the synchronous grid store kinetic energy, primarily due to the rotational momentum of their rotors. Through their electrical coupling to the power system, these generators provide a level of inertia to the rotation frequency. As a result, when a disturbance causes frequency fluctuations, the initial resistance comes from the inertia of these generators. This physical response slows the speed of frequency changes, a characteristic referred to as the Rate of Change of Frequency (RoCoF).

After the initial inertia response, an automatic control system is deployed to restore and stabilize the frequency. This control system is divided into primary, secondary, and tertiary stages [20].

The primary control stage is often the first line of defense after a disturbance. Its rapid response, typically within seconds, adjusts the power generation in proportion to frequency changes, providing an immediate stabilizing effect on the power system frequency.

The secondary control stage follows, with the primary aim of restoring the system frequency to its nominal value and freeing up resources assigned to primary control. This secondary control (or secondary regulation) is typically implemented using Automatic Generation Control (AGC). The AGC involves generating control signals from a centralized control center. These signals regulate the active power output, modifying it in real-time to align with projected demand fluctuations.

Finally, the tertiary control phase aims at long-term system stability. This phase is geared towards the long-term stability of the system. It replenishes the power reserves used during the primary and secondary control stages, ensuring that enough capacity is available for any future disturbances. Tertiary control also corrects the power balance over larger interconnected areas and assists in minimizing the operating cost by calling on the most economical generating units first.

## 2.2 Overview of Inverter-Based Resources in Frequency Regulation

Introducing Renewable Energy Sources (RESs), particularly at higher penetration levels, typically results in new challenges in conventional system frequency control operation, as previously discussed.

The first issue arises due to the low or non-existent inertial responses [11] typically exhibited by inverter-based RESs. These resources are usually connected to the AC grid by power electronic converters, which effectively decouple them. As these Inverter-Based Resources (IBRs) replace conventional synchronous generators with high rotational inertia, the inertia of the entire grid decreases. This reduced inertia causes a marked increase in the Rate of Change of Frequency (RoCoF) of the power system [9], resulting in significant deviations even for small generation-loading mismatches. Recent advances have been made in virtual inertia emulation services to address this issue [11, 23]. In these schemes, grid-forming inverters deliver an inertia-like response proportional to the RoCoF [20].

Secondly, the increased penetration of inverter-based RESs leads to a decrease in the number of conventional generating units providing reserve power for primary and secondary control. This results in higher frequency deviations [9], necessitating the involvement of IBRs in frequency regulation operations. Currently, most standards, such as IEEE1547 and FERC order 842 in the US, require IBRs to include power-frequency droop to support the grid's primary frequency response. This is expected to become a norm in all new IBR installations worldwide [24].

For IBRs to participate in secondary frequency regulation, they need to be dispatchable within specified limits. It's encouraging to note that the technology already exists to make existing IBRs dispatchable [25, 26]. There is a growing expectation for IBRs to provide active power ancillary services in the future, especially as energy storage technologies advance and become more prevalent. This expectation is partly driven by regulations and requirements imposed by system operators in areas with high renewable energy penetration. For instance, Denmark's Transmission System Operators (TSOs), Eltra and Elkraft, require wind plants to track power set points [27].

In some cases, IBRs can be made dispatchable, as seen in direct active power control (APC) in wind turbines and the co-location of renewable resources with energy storage. On the individual wind turbine level, this control is achieved through power electronics, modifications to the generator torque, blade pitch angle, or various other patented schemes, as detailed in [26, 28]. TSO power set-point commands can also be followed collectively across a wind plant as demonstrated in [29] and in successful field tests conducted by

the Spanish TSO [30]. Finally, IBRs could contribute to active power regulation through output curtailment [31]. For example, the electricity output of wind farms may be slightly reduced to provide a quick-access energy reserve. This strategy is often more cost-effective than the alternative, which involves maintaining traditional power plants, such as steam or combined cycle gas turbines (CCGT), in a partially operational state to provide a similar reserve. This is because, unlike these conventional power plants, wind farms don't incur ongoing fuel costs. Furthermore, under certain grid conditions characterized by minimum generation ("min-gen") requirements, renewable energy output might need to be reduced to accommodate the power output from these conventional plants, which must maintain a certain minimum operational level. This scenario is more cost-intensive due to the significant start-up, shut-down, and minimum load maintenance costs associated with conventional power plants.

Determining the market mechanisms for such secondary frequency regulation ancillary services is a current topic of discussion in the literature [26, 32, 33, 34, 35]. One promising structure, which we have assumed in this work, is to have dedicated IBRs with secondary frequency reserves available for prompt dispatch. Compensation to the IBRs for providing these reserves, based on capacity and performance, could be procured through long-term agreements similar to those for voltage support ancillary services [36].

## 2.3 Hierarchical Coordinated Fast Frequency Control for Transmission Systems

A key objective in power system operations is the maintenance of a stable system frequency and the quick restoration of power balance [21]. However, as previously mentioned, the increasing penetration of inverter-connected renewable energy resources (RESs) [37] is resulting in adverse effects on power system frequency regulation [19], due to its increase net-load variability and the faster frequency dynamics it induces in the system [18, 9, 10, 11, 12], making it increasingly difficult for system operators to maintain frequency within acceptable limits, such as the extreme variations noted by the California Independent System Operator in the so-called 'duck chart' [38].

There has been extensive research into the negative dynamic effects of reduced inertia in the power system due to increased renewables, with suggested solutions such as virtual inertia emulation and services [23, 9, 10, 11, 12]. Equally important to consider is the problem of maintaining the average frequency close to nominal during normal operation, with regulation performance being quantified by regulatory authorities in Control

Performance Standards [39, 40]. This task is getting more difficult as, due to the faster frequency dynamics induced by the IBRS, if the load imbalances in the system are not rectified promptly, the faster (and larger) frequency deviations and transient power flows may result in the inadvertent activation of automatic protection devices, hindering the adherence to the performance standards. To better address this, it is essential to consider the local system inertia, primary control response, and primary control deadband, as these have the greatest effect on the average frequency deviations [41]. Hence, this fosters the need for localized fast frequency control strategies, which take into cognizance the local system model and parameter information. Traditionally, the Automatic Generation Control (AGC) system employs a centralized approach to maintain average frequency deviations within desired limits for each balancing authority area. This is achieved by generating control signals at a central control center. However, the extensive size of the balancing authority areas can lead to significant time delays for measurements to be sent to the control center, processed, and then returned to the power-generating stations as actuation signals. These delays are often exacerbated by the considerable communication delays prevalent in today’s power system communication infrastructure, as noted in [6, 42]. Moreover, the large geographical size makes maintaining an accurate dynamic system model challenging. As a result, the AGC system relies on traditional frequency bias constant methods [43], which, while somewhat effective, can limit its speed and usefulness for rapid frequency control. Hence, conventional frequency control strategies may not be effective, necessitating the use of modern, high-bandwidth control schemes. These high-bandwidth control schemes will become increasingly feasible as the grid modernizes, with communication infrastructure playing a dominant role [6, 13]. Advances in remote communication and sensing with the use of global positioning system (GPS) synchronized phasor measurements units (PMUs) will allow for improved monitoring and protection [6], enabling fast control actions using IBRs to quickly compensate disturbances [13].

If parametric models are readily accessible, then *modern* model-based controller design approaches may be used to facilitate these fast frequency control actions. Approaches to fast frequency control can be roughly divided into three categories: model predictive control (MPC), adaptive control, and miscellaneous methods for coordinated dispatch. Control schemes based on MPC have been proposed in several studies [44, 45, 46, 47]. Although MPC-based approaches have the desirable feature of constraint satisfaction during transients, this benefit relies heavily on accuracy of the system model, and the resulting control laws place a heavy communication burden for real-time implementation. Due to the increasing power system scale, complexity and changing dynamics, ensuring this high accuracy in the system model is a major challenge in practice.

Traditional frequency control based on automatic generation control (AGC) [48, 49]

usually requires extensive tuning of the AGC’s PI controllers to obtain good performance and stable operation. Authors in [50] propose an adaptive controller that seeks to automate this tuning process by computing and applying a correction in real time. Other adaptive approaches [51, 52], aim to tackle the frequency control problem by minimizing the need for a system model by using techniques based on dynamic programming and artificial intelligence. However, it is usually difficult to assess the stability of these controllers. There has also been high-profile failures of implemented adaptive controllers [53].

The final category seeks to provide frequency support to the system by utilizing fast acting inverter-based resources. Researchers in [11, 54, 55] have utilized IBRs for virtual inertia and primary frequency control support. Authors in [56] have proposed a load frequency controller which provides frequency control by adjusting the setpoints of distributed energy resources by means of direct observation of active power generation and consumption. Despite this method’s advantages over the traditional AGC, it requires a high degree of monitoring infrastructure and total grid visibility.

Another approach in the same category is the wide-area monitoring and control scheme proposed by researchers in [12, 57]. In the scheme, a central authority, operating on a slow time-scale, coordinates and optimizes geographically dispersed local controllers, which receive measurements from PMUs and dispatch controllable active power resources to mitigate the effect of disturbances. However, the work does not investigate the stability or robustness of the scheme. Furthermore, although measurements are collected regionally, control is still based on a system-wide frequency estimate, which may not effectively address the issue of inertia heterogeneity. Finally, the central authority, as it receives the status and resource limits of all resources, has system-wide visibility which raises privacy issues and may limit the distributed implementation.

In this work, we consider a novel, real-time, layered frequency control scheme that exploits the improvements in modern grid monitoring and communication infrastructure by utilizing local, flexible inverter-based resources to quickly correct active power imbalances arising in the system, thereby minimizing the average system frequency deviation. This scheme addresses the shortcomings of the aforementioned strategies by relying on simple nominal models of the system, being amenable to standard analytical analysis of stability and performance, utilizing mostly local information that is easily accessible, and safeguarding data ownership and privacy.

## 2.4 Data-Driven Extension to Hierarchical Coordinated Fast Frequency Control Framework

As alluded to previously, it is important to build model information flexibility into the control scheme in order to improve its adaptability to real-world implementation. Due to the increasing power system scale, complexity, and changing dynamics, ensuring this high accuracy in the system model is a major challenge in practice [58]. Additionally, it may be the case in practice that reliable values for these model parameters cannot be obtained with reasonable effort, or cannot be accurately updated as system conditions change, ultimately limiting the performance of model-based designs. For example, simulations in 3.10 show deterioration in control performance (e.g., post-disturbance settling time and overshoot) when there are parametric mismatches between the true system model and the model used for design.

Data-driven or data-based controller design methods provide a promising alternative in this regard. Proposals to address the issue of power system frequency control using data-driven control can be broadly divided into two categories: indirect and direct. In an indirect approach, historical data from the power system is used to explicitly identify a system model, and a controller is then designed based on that model (e.g., [59, 60]). The indirect approach has the advantage of providing an explicit, interpretable model of the system, which can aid in understanding the particular frequency response dynamics. However, even selecting an appropriate parametric model to fit is a difficult trial-and-error process, particularly in modern power systems with diverse and quickly evolving components. Additionally, there is evidence that the intermediate identification step may lead to poorer closed-loop performance than recent direct approaches [61].

In a direct data-driven or model-free approach, a frequency controller is designed directly based on recorded or online real-world data, without explicit identification of a system model. One broad approach in this category is adaptive dynamic programming or reinforcement learning [62, 63, 64, 65]. Here, control actions are taken to maximize some form of cumulative reward. However, reinforcement learning approaches are limited by their sensitivity to hyper-parameter selection, the complex training process required to determine the weight coefficients of the trained agent, which in turn relies on a significant amount of historical sampled data [66, 67].

In contrast with reinforcement learning, a suite of alternative direct data-driven control approaches have recently appeared [68, 66, 69, 14], and derive from a branch of control theory called behavioral systems [70, 71]. These techniques allow for direct control while being sample efficient, and often come with rigorous performance guarantees. While the

specific controllers differ between approaches (e.g., model-predictive [66], linear-quadratic, [69] etc.), these approaches all rely on the so-called *fundamental lemma* of behavioral systems, which states that a single recorded trajectory is sufficient to capture the underlying dynamic model of the system if the input signal is rich enough to excite all system modes [70]. Our proposed data-driven controller is based on this principle.

# Chapter 3

## Hierarchical Coordinated Fast Frequency Control using Inverter-Based Resources

In this chapter, we delve into the specifics of our innovative hierarchical coordinated fast frequency control scheme that utilizes inverter-based resources. The chapter is structured as follows:

Section 3.1 provides a concise introduction to our two-layer local-global inverter-based resource (IBR) control scheme, which offers a rapid and localized response to frequency events.

Section 3.2 discusses the local disturbance estimation and rejection control loop, a concept loosely grounded on the principle of internal model control. This control loop processes local measurements to generate a real-time disturbance estimate, signifying the imbalance of local generation and net load, and swiftly re-dispatches local IBRs to correct this imbalance. Supporting theoretical analysis for the design procedure is also presented in this section.

In Section 3.3.1, we frame the local re-dispatching of IBRs, stemming from the produced disturbance estimate, as a simple optimization problem.

Section 3.3.2 introduces a higher-level central coordinating controller, designed for situations when local control area (LCA) IBR resources prove insufficient. This controller facilitates the transfer of additional power from electrically close neighboring areas on a slower time scale.

Finally, Section 3.4 validates our results extensively via simulations conducted on two detailed power system models. Several scenarios are examined in this section, including load increases, generation trips, and three-phase faults.

## 3.1 Introduction

The increasing share of inverter-connected renewable energy resources (RES), which is mostly displacing conventional synchronous generators, has increased the variability of active power supply and reduced the rotational inertia in the grid, resulting in faster system dynamics along with larger and more frequent frequency events.

To mitigate these challenges, a fast, area-based hierarchical control strategy is proposed. The overall hierarchical IBR control architecture is sketched in Figure 3.1. Our scheme has the following appealing characteristics: (i) fast local response to local disturbances, (ii) localized use of measurements to minimize latency, (iii) flexibility in the fidelity of dynamic model information required for design, (iv) heterogeneity of system inertia and primary response is directly accounted for by each LCA controller, (v) minimal communication between control areas, and (vi) no single point of failure, as the majority of control has been localized. We provide more details below.

## 3.2 An Internal Model Control Approach for Local Area-Based Frequency Control

We assume that the power system is partitioned into small local control areas (LCAs), with the goal being for local resources in each area to correct local net load imbalances. These areas should ideally have access to, or be near, fast-acting inverter-based resources (IBRs). The premise is that these IBRs, due to their proximity, can facilitate quick control measures. These resources are not necessarily large wind or solar plants, they could also be energy-storage powered installations or other fast-acting and dispatchable resources. This shrinking of the spatial scale permits increasing decentralization of control actions, and is enabled by the expected deployment of more sensing and inverter-based resources within the system. The overall hierarchical IBR control architecture using a three-area power system is sketched in Figure 3.1. The power system consists of 18 buses, 36 transmission lines, and 15 generators. The generators consist of 5 conventional synchronous generators, 4 wind generation plants (WT), and 6 generating units representing generic inverter-based

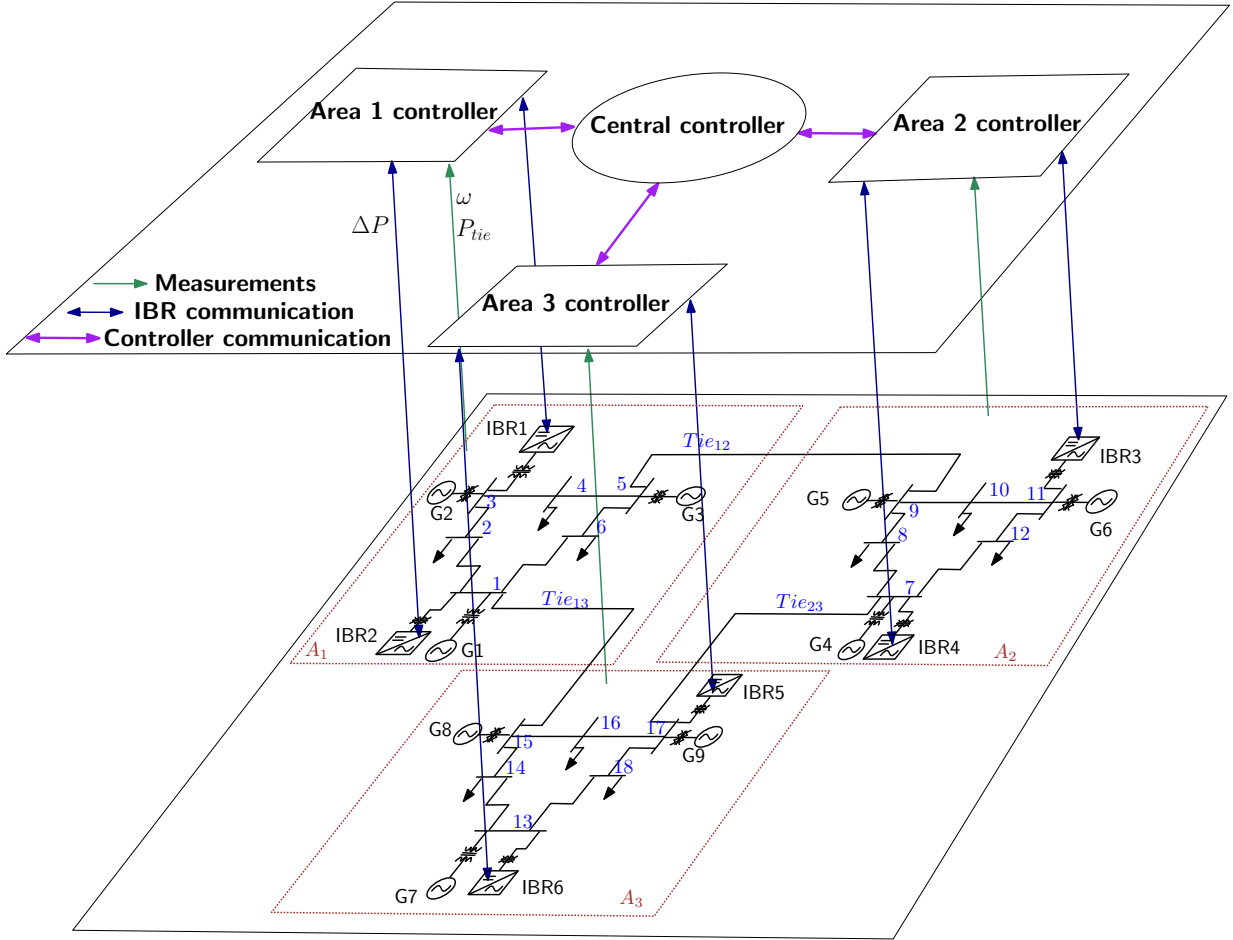


Figure 3.1: Cyber-physical system illustrating frequency control approach.

resources whose inertias are fully decoupled from the grid. Our design involves a local controller for each area, which acts on power and frequency measurements and re-dispatches IBRs to correct local net-load load imbalances. Finally, a central controller coordinates the activities of all LCA controllers in the system to ensure satisfaction of the global objectives.

In this section, we focus on just one such area. Our goal is to design an area-wise decentralized controller which uses only local measurements to correct any power imbalance within the LCA by quickly re-dispatching local IBRs. Our design is based on the idea of disturbance estimation and rejection, and can be interpreted as an implementation of the classical internal model control (IMC) paradigm [72] for internally stable systems.

Our local controller design is based on the block diagram shown in Figure 3.2. The local

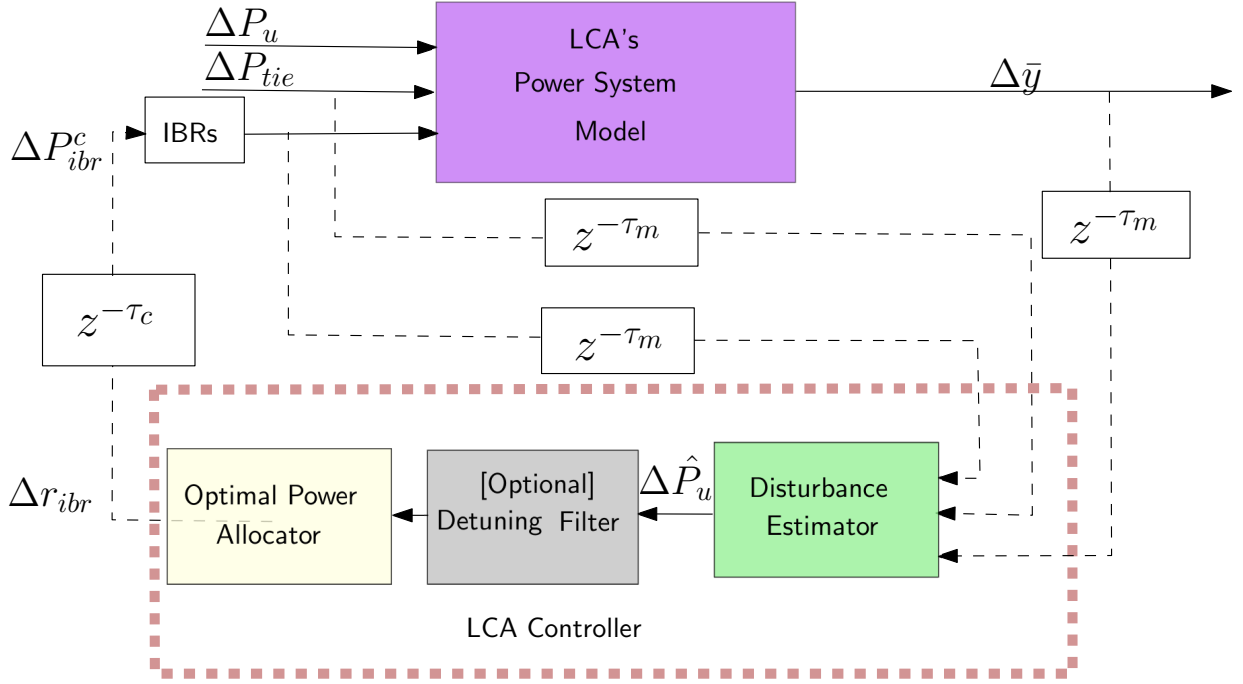


Figure 3.2: Block diagram of area control structure for each LCA. Black dashed lines denote sampled signals.

frequency controller consists of the disturbance estimator, optional detuning filters, and a power allocator. The disturbance estimator processes system measurements to produce an estimate  $\Delta \hat{P}_u$  of the unmeasured net active power change in the LCA, relative to the current dispatch point. This imbalance is then allocated to IBRs within the area. We detail the design of disturbance estimator and detuning filter here, while covering optimal power allocation in the next section.

### 3.2.1 Local Disturbance Estimator for the LCA

The starting point for disturbance estimation is a nominal (small-signal) dynamic model of the LCA dynamics at the current dispatch point. As each LCA represents a very small part of the overall interconnection, it is reasonable that a dynamic model can be locally built and maintained; the accuracy of this nominal model may vary based on the level of detailed system component models available, and one may even wish to fit this model from historical or experimental data. For practical reasons, it is desirable to use the simplest

model which captures the primary frequency response dynamics for design purposes, and as such, we restrict our attention to *lumped LCA models*, where all power injections are assumed to occur at a single electrical point. We generically express the lumped small-signal model of the LCA as

$$\Delta \dot{x} = \tilde{A} \Delta x + \tilde{B}_1 \Delta P_{\text{ibr,tot}}^c + \tilde{B}_2 (\Delta P_{\text{tie}} + \Delta P_{\text{u}}) \quad (3.1)$$

where  $\tilde{A}$  is a Hurwitz stable matrix. In (3.1),  $\Delta x$  is the internal state vector of the area, which could model, for example, generator, load, and IBR dynamics. The control input  $\Delta P_{\text{ibr,tot}}^c$  is the sum of all command changes to IBRs. The measurable disturbance  $\Delta P_{\text{tie}}$  is the sum of all deviations in LCA tie flows, and  $\Delta P_{\text{u}}$  is the net unmeasurable active power imbalance in the LCA. The model (3.1) is a general state-space representation of any LCA model that can be used for *design purposes*, as illustrated in Figure 3.2, and is distinct from the detailed models of the test power systems used in validating the proposed scheme, which are discussed in Section 3.4. We discretize (3.1) using the zero-order-hold method with a chosen sampling period  $T_s$ , yielding a discrete-time model

$$\Delta x^{k+1} = A \Delta x^k + B_1 \Delta P_{\text{ibr,tot}}^{c,k} + B_2 (\Delta P_{\text{tie}}^k + \Delta P_{\text{u}}^k), \quad (3.2)$$

where  $A$  is Schur stable and  $k$  is the sampling instant index. The IBR commands  $\Delta P_{\text{ibr,tot}}^{c,k}$  are subject to communication delays, which for modelling purposes we assume are fixed at  $\tau_c$  sample periods. This can be integrated directly into the model by appending extra states  $\Delta \eta_c$  governed by

$$\Delta \eta_c^{k+1} = A_c \Delta \eta_c^k + B_c \Delta r_{\text{ibr,tot}}^k, \quad \Delta P_{\text{ibr,tot}}^{c,k} = C_c \Delta \eta_c^k, \quad (3.3)$$

where  $(A_c, B_c, C_c)$  is a state-space realization of a  $\tau_c$ -step delay. The unknown net active power imbalance is modelled via a difference equation with unknown initial condition [73, 74]. The simplest choice is the constant disturbance model

$$\Delta P_{\text{u}}^{k+1} = \Delta P_{\text{u}}^k. \quad (3.4)$$

More complex versions of (3.4) require only minor extensions. Moreover, if some load changes are measurable in real-time, this can also be incorporated by adding appropriate feedforward signals to the IBR commands; the details are omitted. The vector of system measurements that we can use for estimation are

$$\Delta \bar{y}^k = C \Delta x^k. \quad (3.5)$$

These measurements should include frequency deviation, but may include other variables such as power outputs and voltages, if available. Measurement delays are again incorporated by appending extra states  $\Delta\eta_m$  as

$$\Delta\eta_m^{k+1} = A_m\Delta\eta_m^k + B_m\Delta\bar{y}^k, \quad \Delta y^k = C_m\Delta\eta_m^k \quad (3.6)$$

where  $(A_m, B_m, C_m)$  is a state-space realization of a  $\tau_m$ -step delay for each measurement. Combining (3.2)–(3.6), the overall model of the LCA with states  $\Delta\xi = (\Delta x, \Delta P_u, \Delta\eta_c, \Delta\eta_m)$ , inputs  $\Delta v = (\Delta r_{\text{ibr,tot}}, \Delta P_{\text{tie}})$ , and delayed measurements  $\Delta y$  is given by

$$\Delta\xi^{k+1} = \mathcal{A}\Delta\xi^k + \mathcal{B}\Delta v^k, \quad \Delta y^k = \mathcal{C}\Delta\xi^k \quad (3.7)$$

where  $\mathcal{C} = [0 \ 0 \ 0 \ C_m]$  and

$$\mathcal{A} = \begin{bmatrix} A & B_2 & B_1C_c & 0 \\ 0 & 1 & 0 & 0 \\ 0 & 0 & A_c & 0 \\ B_mC & 0 & B_mC_c & A_m \end{bmatrix}, \quad \mathcal{B} = \begin{bmatrix} 0 & B_2 \\ 0 & 0 \\ B_c & 0 \\ 0 & B_m \end{bmatrix}.$$

The following result (proof in Appendix A.1) establishes that this extended model is detectable.

**Proposition 3.2.1** (Detectability of Area Model (3.7)). *Assume that  $A$  is Schur stable and that  $\begin{bmatrix} A^{-1} & B_2 \\ C & 0 \end{bmatrix}$  has full column rank. Then  $(\mathcal{C}, \mathcal{A})$  is detectable.*

The rank condition in Proposition 3.2.1 stipulates that the transfer matrix from  $\Delta P_u$  to  $\Delta\bar{y}$  has no transmission zeros at  $z = 1$ ; this will hold as long as a frequency deviation from within the LCA is one of the measured variables. It follows from linear systems theory that we can design a dynamic state estimator [75] for (3.7):

$$\begin{aligned} \Delta\hat{\xi}^{k+1} &= \mathcal{A}\Delta\hat{\xi}^{k+1} + \mathcal{B}\Delta v^k + \mathcal{L}(\mathcal{C}\Delta\hat{\xi}^k - \Delta y^k) \\ \Delta\hat{P}_u^k &= [0 \ 1 \ 0 \ 0] \Delta\hat{\xi}^k, \end{aligned} \quad (3.8)$$

where  $\mathcal{L}$  is the estimator gain matrix which can be designed by, e.g., linear-quadratic optimal methods. The estimator produces the desired running estimate  $\Delta\hat{P}_u^k$  of the unknown net active power imbalance, which can now be allocated to the IBRs.

**Remark 3.2.2** (Detuning for Robust Stability). *In the presence of significant model uncertainty, one may wish to “slow down” the overall control loop to ensure robust closed-loop stability at the cost of decreased controller bandwidth. This can be achieved by passing the estimated unmeasured net active power change  $\Delta\hat{P}_u^k$  through a discrete low-pass filter*

$$F_{\text{detune}}[z] = \frac{1 - e^{-T_s/\tau_f}}{z - e^{-T_s/\tau_f}} \quad (3.9)$$

with filter time constant  $\tau_f > 0$ , and then allocating the result to IBRs.  $\square$

### 3.2.2 System Frequency Response LCA Modelling

For design purposes, a simple and effective model for the LCA dynamics is the following two-state *system frequency response* (SFR) model proposed in [76, 77], which describes the machine mechanical and turbine-governor response. The frequency model represents the averaged system frequency response when all generating units and frequency-responsive loads are viewed as a single aggregate unit. The model, which can be easily put into the general form (3.1), is<sup>1</sup>

$$\begin{aligned} 2H\Delta\dot{\omega} &= -(D + \frac{1}{R_I})\Delta\omega + \Delta P_m - \Delta P_u - \Delta P_{\text{tie}} + \Delta P_{\text{ibr,tot}}^c \\ T_R\Delta\dot{P}_m &= -\Delta P_m - R_g^{-1}(\Delta\omega + T_R F_H \Delta\dot{\omega}), \end{aligned} \quad (3.10)$$

where  $\Delta\omega$  [p.u.] is the area frequency deviation,  $\Delta P_m$  [p.u.] is the mechanical power change,  $H$  [s] is the inertia constant,  $T_R$  [s] is the reheat time constant,  $D$  [p.u.] is the load damping,  $F_H$  the fraction of total power generated by the high pressure turbine,  $R_g$ ,  $R_I$  [p.u.] are the generator and IBRs primary droop constants respectively, where we have simplified the IBRs drop control scheme by eliminating the time constants, since they are significantly faster than the ones of the conventional generators [78].

### 3.2.3 Nominal Stability and Perfect Disturbance Rejection

From Section 3.2.1, the controller for each LCA embeds a dynamic model of the LCA in order to produce a running estimate  $\Delta\hat{P}_u^k$  for the local unmeasured disturbance. It follows by more-or-less standard observer-based control theory that if the total IBR power  $\Delta P_{\text{ibr,tot}}^{c,k}$  in (3.2) is set equal to the disturbance estimate  $\Delta\hat{P}_u^k$  produced by (3.8), then the closed-loop system (3.2)–(3.8) will be internally stable and any constant disturbance will be eliminated, i.e.,  $\Delta\hat{P}_u^k \rightarrow \Delta P_u$  as  $k \rightarrow \infty$ . In other words, the design always achieves *nominal* stability and asymptotically eliminates any load net-load imbalance.

Perhaps surprisingly, the net-load mismatch will still be eliminated even when the LCAs are interconnected as in Figure 3.1 — and will occur irrespective of the model mismatch between the true system and the model used in designing the estimator — as long as the interconnected closed-loop system is stable. To demonstrate this, suppose that the linear

---

<sup>1</sup>We have assumed that most of the generating units are reheat steam turbine units and that the dominant time constants are the reheater time constant and the inertia constant; these assumptions can be easily modified.

time-invariant (LTI) model

$$\begin{aligned}\Delta x_p^{k+1} &= A_p \Delta x_p^k + \sum_j B_{p,j} (\Delta P_{\text{ibr,tot},j}^k - \Delta P_{u,j}^k) \\ \Delta q_i &= (\Delta P_{\text{tie},i}, \Delta \bar{y}_i)\end{aligned}$$

describes the *true* linearized and discretized multi-area power system with measurements  $q_i$  for LCA  $i$ , where  $A_p$  is Schur stable. The aggregated IBR inputs  $\Delta P_{\text{ibr,tot},i}^k$  to this model are set equal to the estimates produced by the LCA disturbance estimators (3.8), which are themselves designed using *any* approximate model (e.g., the SFR model (3.10)) of the LCA. We can then show the following; the proof is in Appendix A.1.

**Theorem 3.2.3 (Perfect Disturbance Rejection).** *Consider the closed-loop system described above, and assume that the system is internally stable. Then for any constant unmeasured net-load disturbances  $\{\Delta P_{u,j}\}$ , it holds for each LCA  $i$  that  $\Delta P_{\text{ibr,tot},i}^k = \Delta \hat{P}_{u,i}^k \rightarrow \Delta P_{u,i}$  as  $k \rightarrow \infty$ .*

Given Theorem 3.2.3, the key issue becomes whether closed-loop *dynamic* stability and performance is maintained in the presence of model uncertainty, i.e., robust stability and performance. We make two comments. First, robust closed-loop stability can always be achieved by lowering the controller bandwidth as described in Remark 3.2.2; see, e.g., [72]. This will guarantee stability at the possible cost of decreased control performance. Second, while we omit the details, we have used modern robust control tools [79] to examine stability robustness of the design without controller detuning, when the estimator is designed based on an SFR-type model (3.10). We have observed guaranteed stability and acceptable performance under up to 10% joint variation in  $H$ ,  $T_R$ , and  $R_g$ . Robust control analysis typically results in conservative guarantees, meaning that much more variation can be tolerated in practice before lowering the control bandwidth becomes necessary. We verify these conclusions on a detailed test system in Section 3.4.5.

**Remark 3.2.4 (Key differences with AGC).** *There are several key differences between our proposed approach and the traditional power system frequency control (primary control plus the AGC).*

**Spatial scale** *In contrast to the large traditional balancing authority areas considered in AGC, which typically contain hundreds of buses and generation sites, the LCAs we consider can be considerably smaller. Many LCAs would be contained within a single balancing authority area, each LCA containing, for instance, several substations. This smaller spatial scale permits further localization of control actions.*

**Model information** While maintaining an accurate dynamic model would be prohibitively difficult to do for an entire balancing authority area, the small scale of LCAs permits estimation and continued maintenance of at least a crude dynamic LCA model, accounting for aggregate inertial and primary control/turbine-governor effects. Incorporation of this model (3.2) into the LCA controller design enables substantially faster estimation of net imbalances compared to the classical frequency bias constant methods used in AGC.

**Temporal scale** The improved local model information described above enables faster and more accurate estimation of local net active power imbalances than is possible in AGC. By combining this fast estimation with fast-acting IBRs as the primary source of compensating power, our scheme is capable of providing fast frequency control within seconds, as opposed to the traditional AGC time scale of minutes.

**Inter-LCA coordination** The AGC is balancing-authority-wise decentralized; no communication occurs during online operation between balancing authorities. As the LCAs considered in our scheme are much smaller than balancing authority areas, it becomes more important to coordinate and share resources between areas when required. The second layer in our proposed control hierarchy achieves this in a fashion that preserves information privacy between areas. We note that this higher coordination layer of our controller is not itself conceptually analogous to AGC, as the objective is explicitly to procure power from adjacent LCAs in an efficient and privacy-preserving manner.

As a final point, we wish to emphasize that the proposed scheme is fully backward-compatible with AGC; both can be implemented on the same system — even if IBRs are integrated into AGC — as they operate on very different spatial and temporal scales.

□

### 3.3 Mathematical Formulation for Optimal Power Allocation

We now design a power allocation mechanism for the IBRs, completing the frequency controller design from Section 3.2. The net power imbalance estimate  $\Delta\hat{P}_u^k$  from the disturbance estimator is used to compute the active power reference for the IBRs in an LCA, subject to the device limits. In Section 3.3.1 we formulate this re-dispatch via a simple optimization problem, which is solved locally at each time step by the LCA controller; we call this stage one of the redispatch. If a very large disturbance occurs however, local resources may not be sufficient to maintain power balance. For this situation, in Section

3.3.2 we design a privacy-preserving higher-level coordination control layer to optimally coordinate IBR responses from nearby LCAs; we call this stage two of the redispatch.

### 3.3.1 Stage 1: Local Redispatch of IBRs

In stage one, at each sampling instant, the local resources are re-dispatched to compensate for the current net disturbance estimate in each LCA. Let  $\mathcal{A} = \{1, \dots, N\}$  index the LCAs, and let  $\mathcal{I}_i = \{1, \dots, m_i\}$  index the resources in LCA  $i$ . Let  $\mathcal{P}_{ij} = [\underline{P}_{ij}, \bar{P}_{ij}]$  denote the power set-point limits for resource  $j$  in area  $i$ . The new optimal power set-points  $\{P_{ij}^*\}_{j \in \mathcal{I}_i}$  for the resources in area  $i$  are computed at time step  $k$  via

$$\begin{aligned} & \underset{P_{ij} \in \mathcal{P}_{ij}}{\operatorname{argmin}} \quad f(P_{i1}, \dots, P_{im_i}, \varphi_i) \\ & \text{subject to} \quad \sum_{j \in \mathcal{I}_i} (P_{ij} - P_{ij}^{\text{ref}}) + \varphi_i = \Delta \widehat{P}_{u,i}^k \end{aligned} \quad (3.11)$$

where  $P_{ij}^{\text{ref}}$  denotes the nominal dispatch set-point for the  $j^{\text{th}}$  resource in area  $i$ . The equality constraint models local power balance. The slack variable  $\varphi_i$  ensures feasibility, and its optimal value  $\varphi_i^*$  represents the remaining power mismatch within the LCA after local redispatch, which will be used in Section 3.3. The objective function  $f$  captures the cost associated with utilizing the resources in the LCA for disturbance rejection; this may be a monetary cost, or may be designed for operational convenience. As our focus is not on economic or market aspects, for this work, we have selected the following cost function

$$f(P_{i1}, \dots, P_{im_i}, \varphi_i) = \sum_{j \in \mathcal{I}_i} \frac{1}{2} \left( \frac{P_{ij} - P_{ij}^{\text{ref}}}{\bar{P}_{ij} - P_{ij}^{\text{ref}}} \right)^2 + \lambda |\varphi_i|.$$

Minimization of  $f$  allocates power to the resources in proportion to their available headroom. When set large enough, the penalty parameter  $\lambda > 0$  ensures that  $\varphi_i^*$  is zero when local resources are sufficient to balance the local disturbance. Note that the limits of the devices and the current dispatch set-points are assumed to be available to the LCA controllers. Hence, resources at their maximum operating range and with no available headroom will not be dispatched. The optimization problem (3.11) can be solved very quickly and reliably at each sampling instant.

### 3.3.2 Stage 2: Coordination Layer for Inter-Area IBR Response

If local resources in LCA  $i \in \mathcal{A}$  are insufficient, then from Section 3.3.1, the local mismatch variable  $\varphi_i^*$  will be non-zero. The variables  $\varphi_i^*$  are communicated to a centralized controller

(Figure 3.1), which is tasked with computing an *aggregated* dispatch adjustment  $a_i^* \in \mathbb{R}$  for each LCA via the quadratic program (QP)

$$\min_{\{a_i\}_{i \in \mathcal{A}}} \sum_{i \in \mathcal{A}} q_i a_i^2 \quad (3.12a)$$

$$\text{s.t. } 0 = \sum_{i \in \mathcal{A}} (a_i - \varphi_i^*) \quad (3.12b)$$

$$0 \leq a_i \cdot \text{sign}\left(\sum_{i \in \mathcal{A}} \varphi_i^*\right), \quad i \in \mathcal{A} \quad (3.12c)$$

$$a_i + \sum_{j \in \mathcal{I}_i} P_{ij}^* \in \mathcal{P}_i, \quad i \in \mathcal{A} \setminus \{1\}. \quad (3.12d)$$

The weight  $q_i$  in the objective is designed as

$$q_i := \sum_{j \in \mathcal{A}} |Z_{ij}| w_j, \quad w_j := \frac{|\Delta \widehat{P}_{u,j}|}{\epsilon + \sum_{k \in \mathcal{A}} |\Delta \widehat{P}_{u,k}|}, \quad (3.13)$$

where  $Z_{ij}$  is the *effective impedance* [80] between LCAs  $i$  and  $j$ , with  $Z_{ii} \equiv 0$  and where  $\epsilon > 0$  is small to prevent division by zero. The intuition is that  $q_i$  is a weighted average of the distance from LCA  $i$  to LCAs where disturbances are significant; a small distance encourages power procurement from LCA  $i$ . In essence, areas that are electrically close to the load disturbance will be sourced for additional power. The effective impedance is computed based on a per-phase, per-unit equivalent of the connections between LCAs; see, e.g., [80]. The constraint (3.12b) ensures global power balance, while (3.12c) ensures all adjustments are made in the same direction. Finally, (3.12d) enforces aggregate power limits for each LCA, with the aggregate area constraint set  $\mathcal{P}_i$  defined as

$$\mathcal{P}_i = \left[ \sum_{j \in \mathcal{I}_i} \underline{P}_{ij}, \sum_{j \in \mathcal{I}_i} \overline{P}_{ij} \right].$$

To ensure feasibility of (3.12), the first LCA is treated as a slack area. Once (3.12) is solved, the aggregate IBR dispatch adjustments  $a_i^*$  for each LCA are disaggregated by each LCA by locally re-solving (3.11) with  $\Delta \widehat{P}_{u,i}$  replaced by  $\Delta \widehat{P}_{u,i} + a_i^*$ .

### 3.3.3 Privacy-Preserving Distributed Implementation of Stage 2

If all data in (3.12) is available to the central controller, then (3.12) can be directly solved. Information privacy of local IBR information may be an important factor however, and we therefore consider a distributed method solution in which more information is kept local to each LCA. Define the closed convex constraint sets

$$\mathcal{C}_{\text{bal}} := \{(a_1, \dots, a_N) \mid (3.12b) \text{ holds}\}$$

$$\mathcal{C}_i := \{a_i \mid (3.12c) \text{ and } (3.12d) \text{ hold}\},$$

and let  $\mathbb{I}_{\mathcal{C}}(x)$  denote the *indicator function* of a closed convex set  $\mathcal{C}$ , which is  $+\infty$  if  $x \in \mathcal{C}$  and zero otherwise. The problem (3.12) can be equivalently written as

$$\begin{aligned} \min_{\{a_i\}_{i \in \mathcal{A}}} \quad & \sum_{i \in \mathcal{A}} [q_i a_i^2 + \mathbb{I}_{\mathcal{C}_i}(a_i)] + \mathbb{I}_{\mathcal{C}_{\text{bal}}}(z_1, \dots, z_N) \\ \text{subject to} \quad & z_i = a_i, \quad i \in \mathcal{A}, \end{aligned}$$

where dummy variables  $z_i$  have been introduced. When written in this form, the problem now admits an iterative distributed solution via the *alternating direction method of multipliers* (ADMM) [81]. Each LCA receives the scalar computation variables  $(z_i^k, u_i^k)$  from the central controller, and locally computes a scalar update via the local optimization

$$a_i^{k+1} = \underset{a_i \in \mathbb{R}}{\text{argmin}} \quad q_i a_i^2 + \mathbb{I}_{\mathcal{C}_i}(a_i) + \frac{\rho}{2} |a_i - z_i^k + u_i^k|^2, \quad (3.14)$$

where  $\rho > 0$  is a penalty parameter. The value  $a_i^{k+1}$  is returned to the central controller, which performs the vectorized coordination update

$$\begin{aligned} z^{k+1} &= \text{Proj}_{\mathcal{C}_{\text{bal}}}(a^{k+1} + u^k) \\ u^{k+1} &= u^k + a^{k+1} - z^{k+1}, \end{aligned} \quad (3.15)$$

where Proj denotes the Euclidean projection onto the constraint set. The update (3.14) is a small convex quadratic program, while (3.15) is just a linear update; both can be solved quickly and reliably, and the iterates  $a_i^k$  will converge to the optimizer of (3.12). The following parameters are communicated from the LCAs to the central controller: (i) the power mismatch  $\varphi_i$  in the LCA, (ii) the estimate  $\Delta \widehat{P}_{u,i}^k$  of the net power imbalance in the LCA, and (iii) the current power adjustment from the LCA  $a_i^{k+1}$  during the ADMM loop iteration process. The central controller in turn sends a weight vector  $([w_j])$ , which is computed from the estimated load imbalances, a control flag indicating convergence, and the iteration variables  $(z_i^{k+1}, u_i^{k+1})$ . Communication occurs only between each LCA and the central coordinating control; LCAs do not communicate directly with one another. Hence, potentially sensitive information such as unit operating status, device limits, set-points, and available spare capacity of resources in an LCA are not shared with either the central controller or the LCA neighbors.

**Remark 3.3.1 (IBR Energy Sources and Markets).** *In this work we have not focused on the specific energy sources behind the dc links of the IBRs, but have considered a generic*

source, which could be dispatchable integrated battery + inverter-based resource solutions [82], or dispatchable active power controlled wind farms [34, 26, 30], photovoltaic (PV) systems [83, 84], or a combination. For our purposes, the key feature is that the source is dispatchable within specified limits, which may themselves change over time. It is pertinent to note that the technology already exists for these IBRs to be dispatchable [25, 26].

The controllers we design for each LCA require the IBRs to follow power set-point commands with limits. In the language of the current system, this is most similar to the concept of secondary frequency response reserves. We have assumed that these reserves can be quickly deployed, and have modelled a ramp time constant of 0.3 seconds for the IBRs used in our case studies. Determining the specific regulatory or market mechanism for providing such an ancillary service is outside the scope of this work, but is a topic of current consideration in the literature [26, 32, 33, 34, 35, 25]. Instead, we have assumed that dedicated IBRs with secondary frequency reserves are available in each LCA, and that these IBRs send their current set-points and device information, including limits, to the LCA controller. The capacity and performance-based compensation to the IBRs for providing these reserves could be procured through long term agreements similar to those for voltage support ancillary service [36]. Finally, we remark that we do not envisage that these dedicated IBRs will be providing power indefinitely after a frequency event. On a longer time-scale, generators can be ramped up through the usual AGC system and IBR injections can be correspondingly ramped down to pre-event values, freeing up fast resources for future frequency events.  $\square$

### 3.4 Simulation Studies

We illustrate our designs by applying them to the 3-LCA 9-machine power system shown in Figure 3.1 and the 5-LCA 68-bus system shown in Figure 3.13, both implemented in Simscape Electrical. Each LCA of the interconnected system in Figure 3.1 is based on the IEEE 3-machine 9-bus system [21], with the areas interconnected through identical tie-lines, whose parameters are given in Table 3.1.

In total, four out of the initial nine synchronous generators in the 3-LCA system have been replaced with an equal number of lower-inertia wind power farms, with the majority of the active power in the modified system now being supplied by renewable power generation. The larger power system in Figure 3.13 is the 5-area 68-bus IEEE benchmark model, with 16 synchronous generators and 86 transmission lines from [85]. All of the conventional power plants were modelled with sixth-order synchronous generators and includes detailed turbine-governor, excitation, and power system stabilizer (PSS) models, while the wind

Table 3.1: Tie-line parameters for 3-area system; 100 megavolts ampere (MVA) base.

Node 1	Node 2	R (p.u.)	X (p.u.)	B (p.u.)
1	15	0.05	0.20	0.15
5	9	0.05	0.20	0.15
7	17	0.05	0.20	0.15

power was modelled using Type 3, doubly-fed induction generator (DFIG) wind turbine systems. Two converter-based units, with droop control schemes, are present in each LCA for fast control, and include current limiters; system data is shown in Table 3.2. In selecting suitable test systems for this work, we have modified the 3-LCA 9-machine system to better represent the low-inertia, green next-generation power grid, while the larger 5-LCA system represents a more conventional grid with slower frequency dynamics owing to the predominance of SGs over inverter-based power resources.

Table 3.2: Generator and IBR Data.

Node	Gen. ID (and type)	Rating (MVA)	Dispatch (MW)
1,13	G1, G7 (Hydro)	247.50	72.24
1	IBR2 (Inverter-based resource)	50	15
3	G2 (Fossil-based)	192	126
3	IBR1 (Inverter-based resource)	50	25
5, 11, 17	G3, G6, G9 (Fossil-based)	128	85
7	G4 (Hydro)	247.5	71.99
7	IBR4 (Inverter-based resource)	50	20
9	G5 (Fossil-based)	192	133
11	IBR3 (Inverter-based resource)	50	10
13	IBR6 (inverter-based resource)	50	5
15	G8 (Fossil-based)	192	128
17	IBR5 (Inverter-based resource)	50	30

Each LCA disturbance estimator was designed based on the SFR model (3.10), with raw parameters taken from [21] and SFR parameters set based on the method in [76]. For the estimator design itself, time delays for both measurement and control signals were fixed at 200ms, and the estimator gain  $\mathcal{L}$  was tuned using standard linear-quadratic methods. Simulation tests were performed with measurement and control signal delays of 300ms and

500ms. The selection of 300 to 500ms delays is a somewhat pessimistic choice, based on worst-case delays for wide-area communication via high-speed Ethernet.

Both the LCA controllers in Section 3.2 and the central controller in Section 3.3 operate continuously with a fixed sampling period  $T_s = 25\text{ms}$ , which was selected based on what can be expected based on continued deployment of PMUs. At each sampling period the LCA controllers send the power mismatch  $\varphi_i^*$  to the central controller, which computes the total power mismatch  $\sum_{i \in \mathcal{A}} \varphi_i^*$ . If this is within a pre-defined tolerance ( $\approx 5\%$  of the spare capacity available in each area), then no further action is taken. When  $\sum_{i \in \mathcal{A}} \varphi_i^*$  exceeds the set tolerance, a flag is triggered and the centralized optimization in Section 3.3 is executed, either by directly solving (3.12) when information is centralized, or by beginning the iterations (3.14)–(3.15) when information privacy must be preserved.

Table 3.3: SFR model parameters for LCA estimator design.

Quantity	Value	Comment
$H$	Varies	Normalized area inertia constant
$T_R$	10 s	Reheat time constant
$R_g, R_I$	5%	Speed regulation
$F_H$	0.64	Frac. of power generated by high pressure turb.
$D$	0	Load damping coefficient
$T_s$	25 ms	Estimator sampling period
$\epsilon$	$10^{-9}$	Avoids division by zero in (3.13)
$\lambda$	100	Penalty coefficient in (3.11)
$\rho$	1	Penalty coefficient in (3.14)

In total we consider seven scenarios, where the first six scenarios are simulated on the three-LCA power system shown in Figure 3.1 and the last scenario involving two cases is validated on a larger five-LCA power system shown in Figure 3.13. The scenarios considered include: (i) a step load change in one LCA of the three-LCA system that can be fully compensated with only local resources, (ii) a larger step load change in the same LCA, where support from the other areas will be required, (iii) a symmetric three phase-to-ground fault, (iv) the loss of a generator, (v) the intentional introduction of extreme variations in the parameters used in the LCA estimator designs for all three LCAs, (vi) the redispatching of both synchronous generators and IBRs in response to a load change, and (vii) the re-simulation of scenarios I and II on the larger five-LCA power system.

All scenarios are compared against a baseline case without our supplementary control

scheme, wherein frequency support is provided only by conventional generators' inertia and by primary droop control action of both generators and IBRs. We emphasize that our scheme does not aim to supplant the primary control actions of the active power generating resources (which are mandated by regulations from system operators), nor does our scheme attempt to emulate conventional generator inertia. Instead, our scheme is an alternative proposal for how IBRs can enable fast frequency control.

### 3.4.1 Scenario #1: Disturbance with Sufficient Local Resources

In this scenario, a 63 megawatts (MW) load change is applied at bus 8 in area two at  $t = 2$ s. The disturbance is sufficiently small such that it can be compensated locally without coordination with other areas. The frequency response and IBR power setpoints are plotted in Figure 3.3, where we additionally compare the response to that obtained by augmenting the conventional droop-only with an aggressively-tuned AGC-type control which redistributes the IBRs. This AGC-style control is implemented individually for each Local Control Area (LCA). For example, in our system with three LCAs, we would have three distinct AGC schemes operating concurrently, instead of the traditional approach that uses a single AGC system for the whole system.

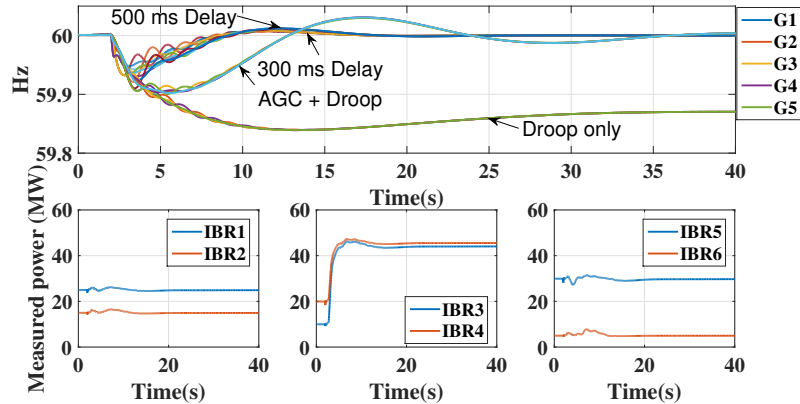


Figure 3.3: Response to 63 MW load change at bus 8; the IBR power plots correspond to the case of 300ms delay.

The frequency nadir and settling time with our controller are significantly improved compared to a conventional AGC + droop strategy, with similar performance observed up to 600ms of delay. The IBRs in area 2 quickly ramp up to compensate for the disturbance, while the IBRs in areas 1 and 3 do not significantly respond; the control action is fast

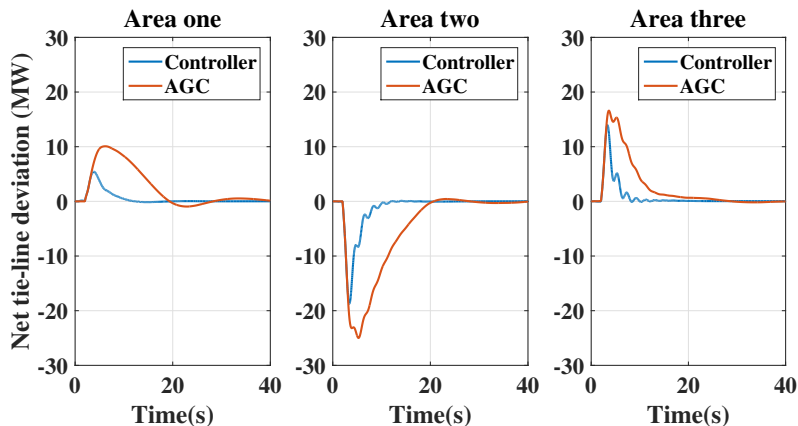


Figure 3.4: Tie-line power flow deviations following a 63 MW load change at bus 8 in area two.

and localized. As one would expect, the closed-loop performance of the scheme degrades slightly with increasing delay; since however we have explicitly included an expectation of 200ms of delay in the design phase (Section 3.2.1), the typical destabilizing effect of delays is largely mitigated.

Recall from Section 3.2.1 that each LCA controller is designed and implemented in an area-by-area decentralized fashion. In Figure 3.3, one can observe a slight increase in *inter*-area oscillations in the presence of our controller. A small-signal stability analysis was performed on the interconnected system, and we have observed a trade-off between the speed of the controller response and a degradation of the damping ration of this particular inter-area mode. This is perhaps not surprising, as the generator PSS units were tuned in the absence of our retrofit control scheme. If desired, this mode can be further damped by (i) re-tuning the PSS loops, or (ii) lowering the bandwidth of our control scheme, as described in Remark 3.2.2.

In Figure 3.4, we observe that the proposed scheme reduces the inadvertent power exchange from adjacent areas following the disturbance compared to the classical AGC-balancing mechanism. In this scenario where the contingent area has sufficient resources to correct the local imbalance, the proposed scheme results in significantly less energy borrowed from adjacent areas, thereby minimizing any incurred penalty and providing additional value to the operator.

### 3.4.2 Scenario #2: Disturbance with Insufficient Local Resources

This scenario is identical to the self-sufficient case, but a 130 MW load change is applied instead, which is sufficiently large to activate both stage one and stage two of our redispatch scheme. The dynamic responses for this case are shown in Figure 3.5.

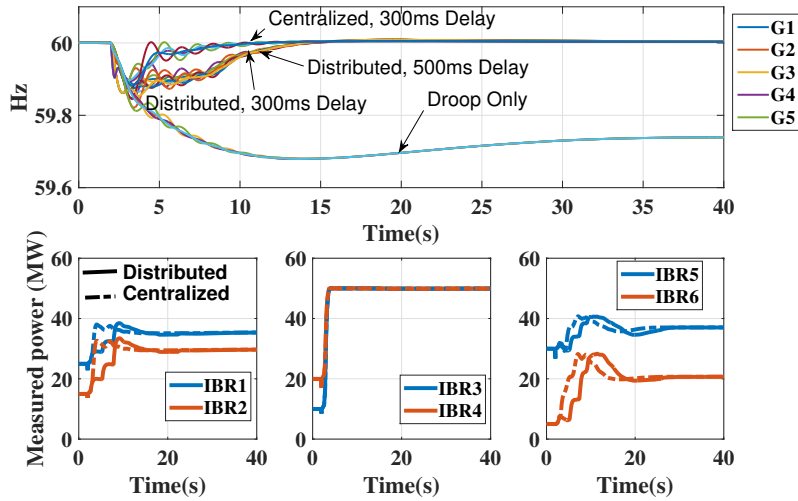


Figure 3.5: Response to 130 MW load change at bus 8.

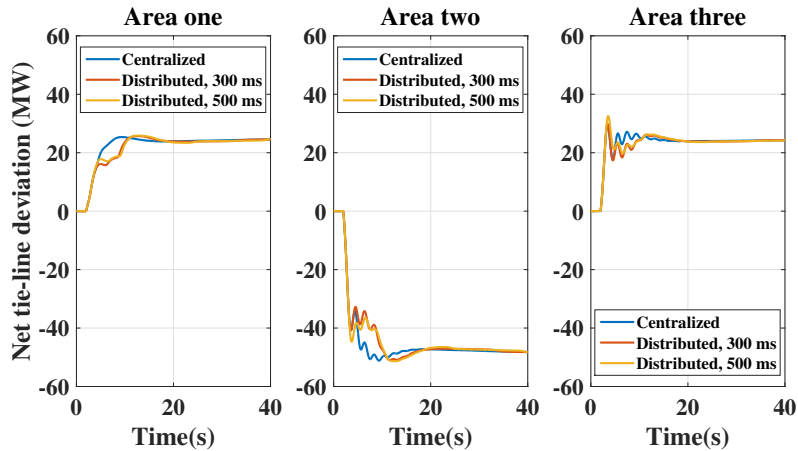


Figure 3.6: Plot of net tie-line flows following a 130 MW load change at bus 8.

Following the disturbance, the controller in the contingent area reacts and maxes out its IBR resources, which both have limits of 50 MW; as expected, the controllers in other

areas do not initially respond. Stage two activates after the total mismatch exceeds the specified tolerance of 20 MW; we plot the responses for both the centralized and distributed implementations of stage two (Section 3.3.3). As can be seen in Figure 3.5, the non-contingent areas supply additional active power to compensate for the disturbance, and the system frequency is eventually brought back to nominal value. We have considered a communication delay of 300 ms for the centralized implementation and both 300 ms and 500 ms delays for the distributed implementation. As the distributed implementation requires many iterations, each of which is subject to communication delays, it is noticeably slower than the centralized implementation. The responses therefore illustrate the speed-privacy trade-off between the centralized and distributed implementations. The net tie-line deviations from pre-disturbance values are plotted in Figure 3.6; a comparison with an AGC-type control has not been included in this case since, due to the insufficient IBRs' capacity in the contingent area, it will be impossible for the integral control of the AGC to restore the tie-line flows to their scheduled values.

### 3.4.3 Scenario #3: Symmetric Three-Phase Fault

For this scenario, a three-phase line-to-ground fault was introduced at bus 10 in area 2 at  $t = 2$ s; the fault was cleared after 0.1 secs. Figures 3.7 and 3.8 show the dynamic response of the system following the introduction of the fault.

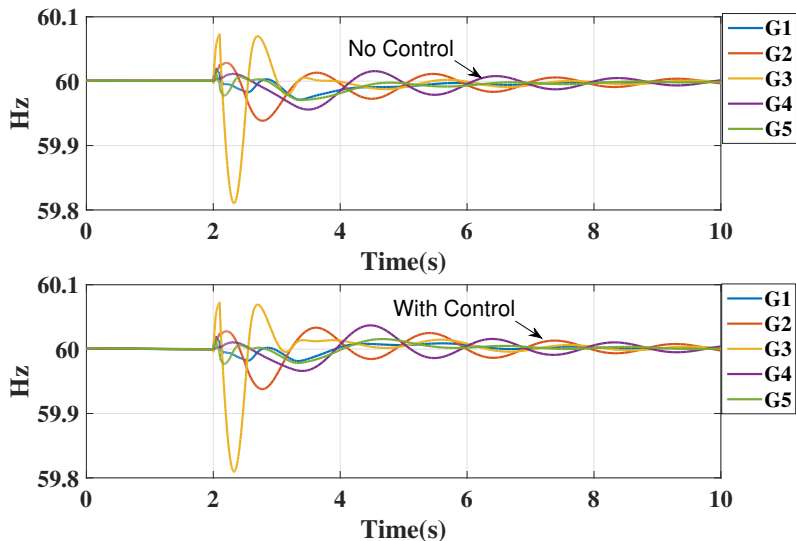


Figure 3.7: Frequency response to three-phase fault.

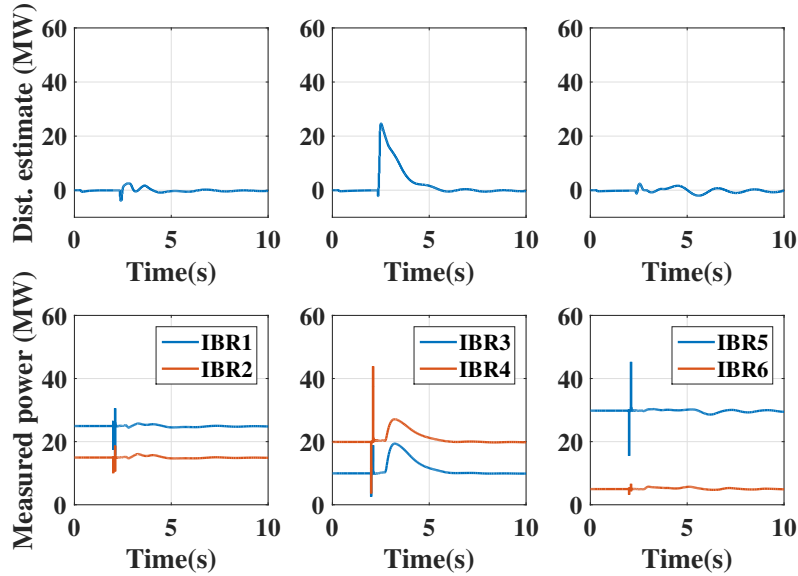


Figure 3.8: Plots of load estimate and IBR outputs following a three-phase line-to-ground fault at bus 8 in area 2.

From Figure 3.7, we see that our design does not alter the transient frequency behaviour of the system following the fault compared to the base case. As can be seen from Figure 3.8, the load estimates in the non-contingent areas are negligible, and the IBRs do not significantly respond. In the contingent area, there is a small transient disturbance estimate, which smoothly returns to zero with minimal IBR response. We conclude that the control strategy is able to detect ‘frequency events’ and ignore ‘non-frequency events’, which are desirable properties of fast frequency response schemes [12].

### 3.4.4 Scenario #4: Loss of Generator

In this scenario, we have simulated a loss of generator G2 in area 2 at  $t = 2$ s. The lost generator had a pre-fault dispatch of  $\approx 72$  MW. The response is plotted in Figure 3.9. Similar to Scenario #2, the controller in the contingent area maxes out its IBR resources following the generator loss, which resulted in a load imbalance of  $\sim 72$  MW. Controllers in other areas however do not provide additional support via stage two, as the remaining power mismatch does not exceed the specified tolerance of 20 MW. This scenario additionally illustrates the robustness of the method, as the LCA controller for area 2 is designed assuming that the inertia and primary response of generator G2 are present.

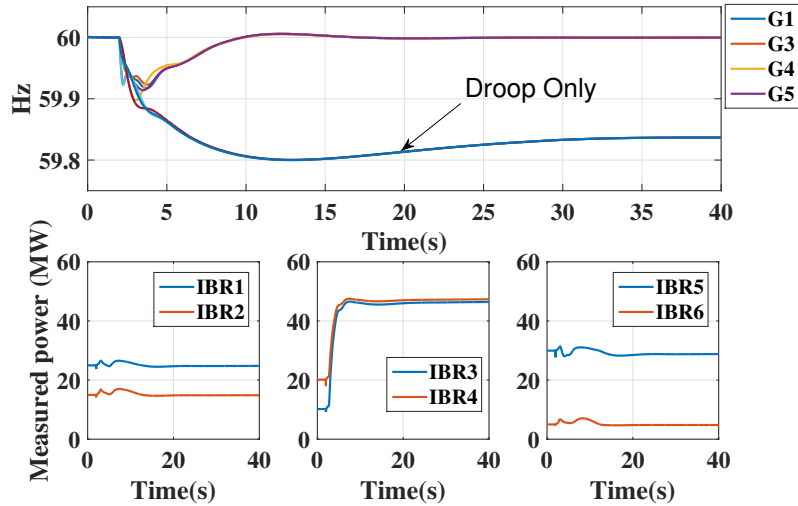


Figure 3.9: Response to loss of generator G2.

Despite this significant parameter variation, the control action is similar to that in Scenario #1.

### 3.4.5 Scenario #5: Parameter Variation

In this scenario we assess the controller's performance in the presence of extreme variations in the parameters used in the LCA estimator designs for all three areas; see Table 3.4. The disturbance is as in Scenario #1, with a communication delay of 300ms. The response is shown in Figure 3.10.

It can be seen from Figure 3.10 that the system remains stable despite these significant parameter variations, although the frequency response is degraded. Case 1 produces a more oscillatory response due to the underestimated turbine time constant, while Case 2 produces a larger overshoot due to the overestimated turbine constant. Consequently, this scenario illustrates the margin of error we are afforded in the model used for the LCA estimator design.

Table 3.4: SFR model parameters for Scenario #5.

Case	Quantity	Value
Base Case	$H$	nominal
	$T_R$	nominal
	$R_g$	nominal
	$R_I$	nominal
	$F_H$	nominal
Case 1	$H$	50% decrease from nominal
	$T_R$	80% decrease from nominal
	$R_g$	50% decrease from nominal
	$R_I$	50% decrease from nominal
	$F_H$	Same as nominal
Case 2	$H$	50% decrease from nominal
	$T_R$	60% increase over nominal
	$R_g$	10% increase over nominal
	$R_I$	10% increase over nominal
	$F_H$	65% decrease from nominal

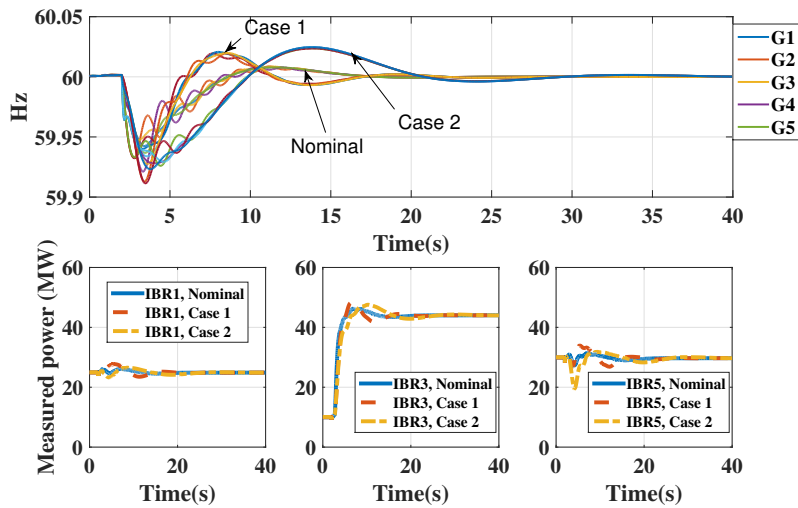


Figure 3.10: Response with variations in model parameters.

### 3.4.6 Scenario #6: Coordination of IBRs and Conventional Generators

While our control scheme is primarily intended for coordination and dispatch of fast IBRs, the optimal redispatch in Section 3.3.1 is in fact agnostic to the underlying source of power used to correct the imbalance. To illustrate the modularity and flexibility of our approach, in this scenario we consider both the conventional synchronous generators (SGs) and the IBRs in the optimal active power allocation of Section 3.3.1. The ratings of the SGs are as shown in Table 3.2, while the capacities of the IBRs were increased to 100 MVA to encourage more IBR participation for this particular test. A 63MW load change is applied at bus 8 in area two at  $t = 2$ s, and the system responses are shown in Figures 3.11, 3.12. Both IBRs and SGs are jointly redispatched according to Section 3.3.1; due to the slower response speed of SGs, the overall speed of the scheme is reduced compared to compensation using only IBRs. In summary, while SGs can be directly integrated into the proposed scheme, this will not necessarily lead to improved performance.

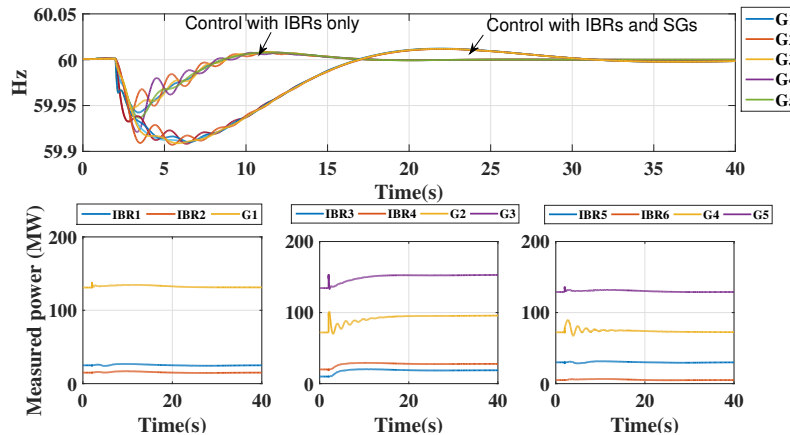


Figure 3.11: Response to 63MW load change at bus 8 with redispatch of both SGs and IBRs.

### 3.4.7 Scenario #7: Test on Larger Power System

To test the performance of the proposed scheme on a large power system, we repeat self sufficient and deficient scenarios (Scenarios #1 and #2) on the 5-LCA test system shown in Figure 3.13.

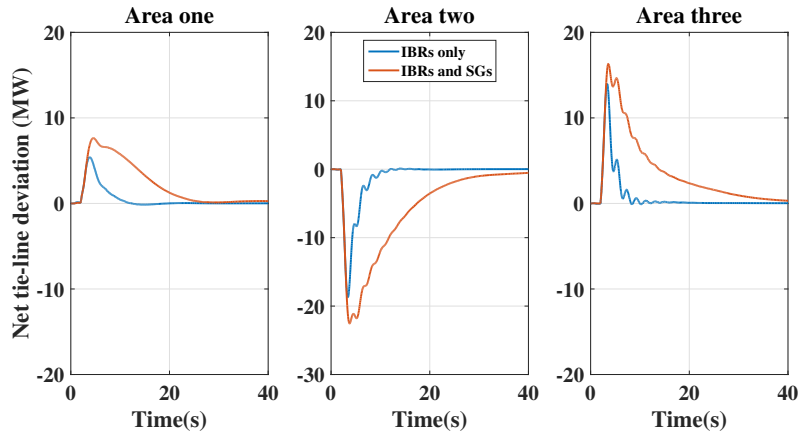


Figure 3.12: Plot of net tie-line flows following a 63 MW load change at bus 8 with redispatch of both SGs and IBRs.

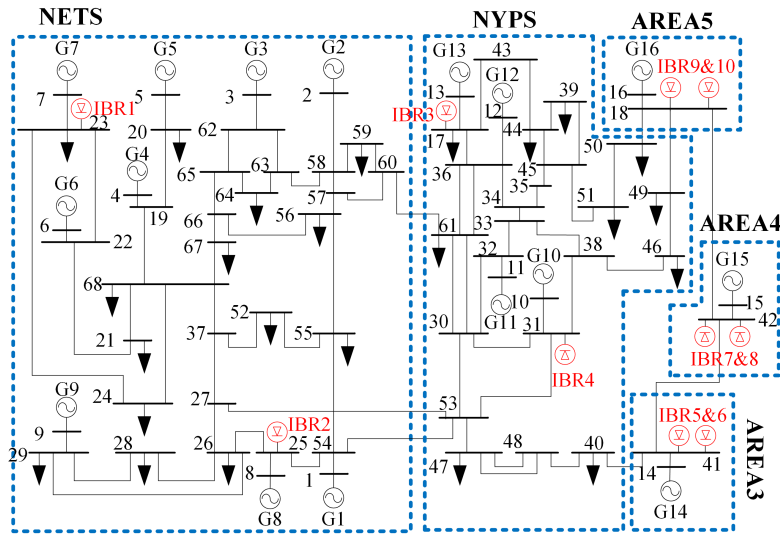


Figure 3.13: 5-area 68-bus test system.

For the self sufficient case, we introduce a 300 MW load change at bus 33 in the NYPS area at  $t = 2$ s. The frequency response, IBR power setpoints and net tie-line deviations are plotted in Figures 3.14, 3.15. It can be seen that the performance is similar to that obtained in the smaller 3-area system (Section 3.4.1), with the IBRs in the contingent area acting quickly to inject active power while those in the non-contingent areas remain close to their dispatch values, resulting in the restoration of the frequency and net tie-line

deviations to their pre-disturbance values significantly faster than an aggressively tuned traditional AGC. The controller shows good performance for both the 300 ms and 500 ms communication delays simulated. From Figure 3.15, we see that the scheme quickly restores the tie line power flows to their pre-disturbance values compared to the AGC-type scheme, minimizing inadvertent exchange between LCAs.

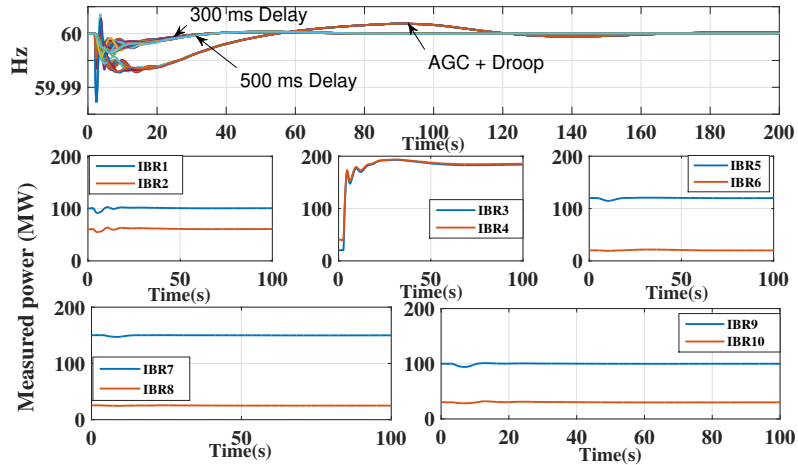


Figure 3.14: Response to 300 MW load change at bus 33.

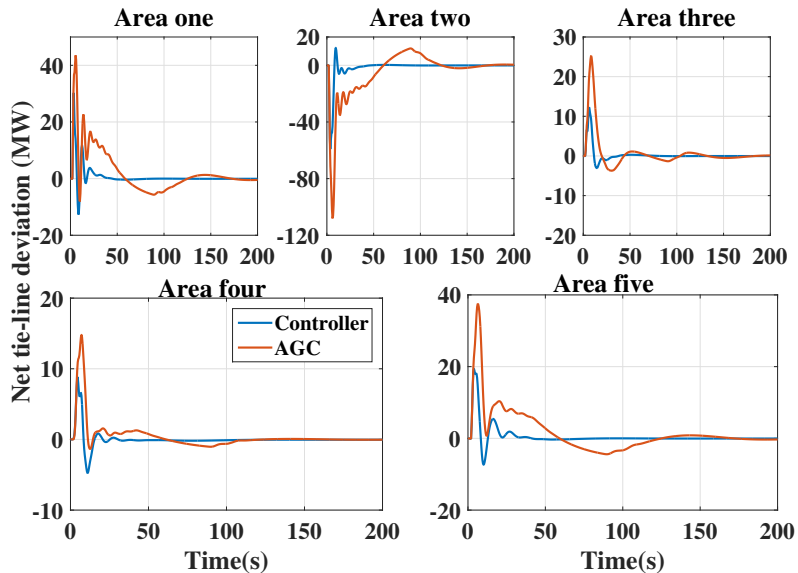


Figure 3.15: Plot of net tie-line flows following a 300 MW load change at bus 33.

We next consider the case where the resources in the contingent area are insufficient to correct a local load imbalance. Here, we introduce a 450 MW load change at bus 33 in the NYPS area at  $t = 2$ s. As can be seen in Figures 3.16, 3.17, the non-contingent areas supply additional active power to compensate for the disturbance after the IBRs in the contingent areas reach their limit and stage two is activated. Since the NETS area and area 5 are electrically closest to NYPS, more active power is sourced from them. The conclusions drawn in Section 3.4.2 still hold on the larger 68-bus system, with the centralized implementation being slightly faster and the controller showing robust performance under the simulated 300 ms and 500 ms communication delays scenarios.

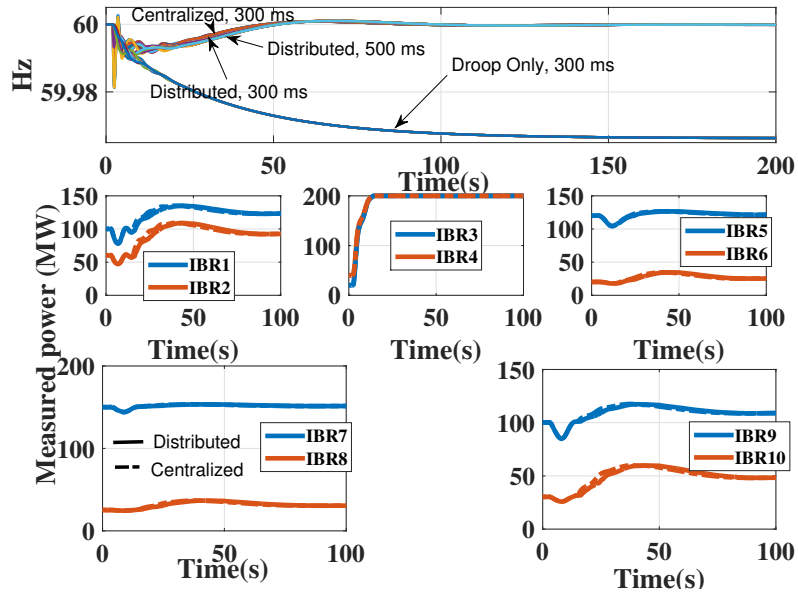


Figure 3.16: Response to 450 MW load change at bus 33.

### 3.5 Summary

We have proposed and validated through detailed simulations a control strategy that provides fast, localized frequency control by partitioning the power system into small areas, and utilizing the fast, inverter-based resources in each area to correct load imbalances originating locally. The local control loop for each LCA quickly estimates the local disturbance and compensates by re-dispatching IBRs. When required, additional power support from neighboring areas is provided from electrically close areas using a higher-level coordinated

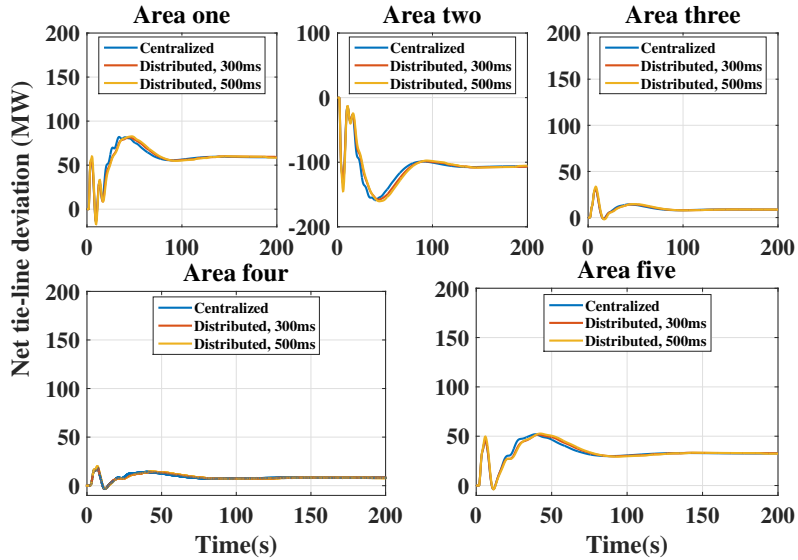


Figure 3.17: Plot of net tie-line flows following a 450 MW load change at bus 33.

dispatch scheme, and we propose a privacy-preserving implementation for this layer. The approach provides fast control action and can be retrofit onto existing systems without compromising stability. Through the LCA controllers, the scheme explicitly accounts for heterogeneity of inertial response throughout the power system.

This scheme depends heavily on the communication infrastructure for its operation, and in light of this, we offer the following observations. If communication links within a Local Control Area (LCA) fail, the local controller, having direct access to the availability of Inverter-Based Resources (IBRs), will experience a decrease in the number of accessible IBR devices. The remaining online IBRs will then be re-dispatched using the existing local optimal allocation scheme. Conversely, the global layer is more vulnerable to communication link failures, which could potentially result in a failure of centralized coordination. This could ultimately prevent additional power from being sourced from neighboring areas. In such a scenario, the local IBRs will still be maximized. However, it's important to note that there is no guarantee that the frequencies in the system can be regulated back to their nominal values under these circumstances.

# Chapter 4

## Data-Driven Extension to Hierarchical Coordinated Fast Frequency Control Framework

In this chapter, we extend our novel hierarchical coordinated fast frequency control scheme using inverter-based resources developed in Section 3 to utilize only measurement data.

### 4.1 A Data-Driven Control Approach for Area-Based Fast Frequency Control

The model-based design of Section 3 requires an explicit and accurate model of the frequency dynamics of each LCA. In practice, this requirement poses at least two major challenges. First, an appropriate class of parametric models must be selected; this step balances simplicity vs. accuracy, and will become increasingly difficult as RESs with black-box power electronic controls proliferate. Second, the parameters of the model must be selected or fit; this procedure itself is challenging, with associated bias-variance trade-offs [86].

To address these issues, in this section we develop two direct data-driven design approaches to supplant the model-based design approach described in Section 3. In essence, the idea is to replace the parametric LCA model (3.10) with a non-parametric model based on time-series data collected from the system. This time-series data is directly used

to design a disturbance estimation scheme, without passing through an explicit system identification step.

Section 4.1.2 describes our first data-driven disturbance estimation approach, which fuses ideas from linear estimator design and behavioral systems theory. The resulting disturbance estimator is described by a linear update rule, and requires tuning of only one scalar gain. To improve robustness to grid nonlinearities and inexact data collection procedures, our second design approach in Section 4.1.3 extends this linear estimation procedure with an optimization-based estimation procedure. Finally, in Section 4.1.4 we describe how these general estimation ideas are adapted for the particulars of power system frequency control and integrated into the hierarchical control framework outlined in Section 3.

### 4.1.1 Brief Background on Data-Driven System Representation

Consider the controllable finite-dimensional discrete-time linear time-invariant (LTI) model

$$\begin{aligned} x(t+1) &= Ax(t) + Bu(t) + B_d d(t) \\ y(t) &= Cx(t) + Du(t) \end{aligned} \tag{4.1}$$

with time  $t \in \mathbb{Z}_{\geq 1}$ , state  $x(t) \in \mathbb{R}^n$ , control input  $u(t) \in \mathbb{R}^m$ , disturbance input  $d(t) \in \mathbb{R}^q$ , and measured output  $y(t) \in \mathbb{R}^p$ . We assume the matrices  $(A, B, B_d, C, D)$  of (4.1) are *unknown*, and hence the model (4.1) cannot be directly used for simulation, analysis, and feedback design purposes. *Behavioral systems theory* provides a set of tools for constructing a data-based representation of the dynamic system (4.1) using input and output measurements [87].

As notation, if  $(z(1), z(2), z(3), \dots)$  is a  $\mathbb{R}^m$ -valued signal defined for positive time, we write  $z \in (\mathbb{R}^m)^{\mathbb{Z}_{\geq 1}}$ . The starting point is to diminish the role of the state, and consider all possible input-output sequences  $(u(t), d(t), y(t))$  which are compatible with (4.1), called the *behaviour*:

$$\begin{aligned} \mathcal{B} &= \{(u, d, y) \in (\mathbb{R}^{m+q+p})^{\mathbb{Z}_{\geq 1}} : \exists x \in (\mathbb{R}^n)^{\mathbb{Z}_{\geq 1}} \text{ s.t.} \\ &\quad \sigma x = Ax + Bu + B_d d, \ y = Cx + Du\}, \end{aligned} \tag{4.2}$$

where  $(\sigma x)(t) = x(t+1)$  is the shift operation. The behaviour (4.2) describes the system (4.1) as a subspace of the vector space of all possible input-output signals, and (4.1) is a *state-space representation* of  $\mathcal{B}$ . The *order* of the system, denoted by  $n(\mathcal{B})$ , is the smallest possible state dimension of the representation (4.1). Given a representation of minimal order, the *lag* of  $\mathcal{B}$ , denoted by  $\ell(\mathcal{B})$  is the smallest integer  $\ell$  such that the matrix  $\mathcal{O}_\ell = \text{col}(C, CA, \dots, CA^{\ell-1})$  has rank  $n(\mathcal{B})$ .

Let  $\mathcal{B}_T$  denote the restriction of the behaviour to trajectories of finite length  $T \in \mathbb{Z}_{\geq 1}$ , i.e., input-output sequences of length  $T$ . Suppose that we have collected  $T$ -samples of *input-output data*  $w^d = (u^d, d^d, y^d) \in \mathcal{B}_T$  from the system. This data may be directly used to create a non-parametric representation of the model (4.2). To do this, let  $L \leq T$  be a positive integer, and organize the data into the *Hankel matrix of depth  $L$* , given as

$$\mathcal{H}_L(u^d) = \begin{bmatrix} u^d(1) & \cdots & u^d(T-L+1) \\ \vdots & \ddots & \vdots \\ u^d(L) & \cdots & u^d(T) \end{bmatrix} \in \mathbb{R}^{mL \times (T-L+1)},$$

with analogous definitions for  $\mathcal{H}_L(d^d)$  and  $\mathcal{H}_L(y^d)$ . The input data  $(u^d, d^d)$  is said to be *persistently exciting of order  $L$*  if  $\text{col}(\mathcal{H}_L(u^d), \mathcal{H}_L(d^d))$  has full row rank; this captures the idea that the inputs are sufficiently rich and sufficiently long. The *Fundamental Lemma* [70] states that if the input data is persistently exciting of order  $L+n(\mathcal{B})$ , then *any possible* length  $L$  input-output sequence  $(u, d, y) \in (\mathbb{R}^{(m+q+p)})^L$  can be expressed as

$$\begin{bmatrix} \mathcal{H}_L(u^d) \\ \mathcal{H}_L(d^d) \\ \mathcal{H}_L(y^d) \end{bmatrix} g = \begin{bmatrix} u \\ d \\ y \end{bmatrix} \quad (4.3)$$

for some vector  $g \in \mathbb{R}^{T-L+1}$ . The linear equation (4.3) is a *data-based representation* of the system (4.1), and can be leveraged for prediction and control [87].

#### 4.1.2 Design #1: Linear Data-Driven Disturbance Estimator

We now consider (4.1) as a model for each LCA. We assume that  $d(t)$  is a constant unknown disturbance signal, which for us will model mismatch between generation and load. In our context,  $x(t)$  would consist of states of generators, converters, loads, and associated control systems,  $u(t)$  would be commands to IBRs, and  $y(t)$  would be available measurements such as frequency deviation. Since (4.1) would represent the system *including* the action of primary controllers, the model (4.1) will be assumed to be internally exponentially stable, i.e.,  $A$  will have eigenvalues within the unit circle.

The design goal is to produce a real-time estimate  $\hat{d}(t)$  of the unknown disturbance  $d(t)$ . Our proposed estimator design consists of two steps:

- (i) a *data-driven forward prediction*  $\hat{y}(t)$  of the output  $y(t)$ ;
- (ii) a *linear update rule* for  $\hat{d}(t)$  using  $\hat{y}(t)$  and the true system measurement  $y(t)$ .

To generate a prediction of the output for time  $t$ , we will leverage (4.3), and assume that historical data  $(u^d, d^d, y^d)$  is available. Model-based prediction using, e.g., (4.1) would require the specification of an initial condition. In the data-driven setting, the initial condition is implicitly defined by using recent online samples of input and output data [68]. Let  $T_{\text{ini}} \geq \ell(\mathcal{B})$  be the length of the initialization data, and define the vectors

$$\begin{aligned} u_{\text{ini}} &= \text{col}(u(t - T_{\text{ini}}), \dots, u(t - 1)) \\ \hat{d}_{\text{ini}} &= \text{col}(\hat{d}(t - T_{\text{ini}}), \dots, \hat{d}(t - 1)) \\ \hat{y}_{\text{ini}} &= \text{col}(\hat{y}(t - T_{\text{ini}}), \dots, \hat{y}(t - 1)). \end{aligned} \quad (4.4)$$

Note that  $\hat{d}_{\text{ini}}$  and  $\hat{y}_{\text{ini}}$  are formed based on our past *estimates* of the disturbance and output. In (4.3), we consider trajectories of length  $L = T_{\text{ini}} + 1$ . We partition  $u, d, y$  in (4.3) as

$$u = \begin{bmatrix} u_{\text{ini}} \\ u(t) \end{bmatrix}, \quad \hat{d} = \begin{bmatrix} \hat{d}_{\text{ini}} \\ \hat{d}(t) \end{bmatrix}, \quad y = \begin{bmatrix} y_{\text{ini}} \\ \hat{y}(t) \end{bmatrix},$$

and correspondingly partitioning the rows of the Hankel matrices in the same fashion as

$$\mathcal{H}_L(u^d) = \begin{bmatrix} U_{\text{ini}} \\ U_f \end{bmatrix}, \quad \mathcal{H}_L(d^d) = \begin{bmatrix} D_{\text{ini}} \\ D_f \end{bmatrix}, \quad \mathcal{H}_L(y^d) = \begin{bmatrix} Y_{\text{ini}} \\ Y_f \end{bmatrix}.$$

With these choices, (4.3) can be re-expressed as

$$\mathcal{H}_{\text{red}} g := \begin{bmatrix} U_p \\ D_p \\ Y_p \\ U_f \\ D_f \end{bmatrix} g = \begin{bmatrix} u_{\text{ini}} \\ \hat{d}_{\text{ini}} \\ \hat{y}_{\text{ini}} \\ u(t) \\ \hat{d}(t) \end{bmatrix}, \quad \hat{y}(t) = Y_f g. \quad (4.5)$$

The first set of equations is solved for the unknown  $g$ , and the prediction  $\hat{y}(t) = Y_f g$  is immediately obtained. If the underlying data-generating system is LTI and the collected data are exact, the Fundamental Lemma guarantees that (4.5) is consistent and the computed response matches the system's response exactly, provided  $T_{\text{ini}} \geq \ell(\mathcal{B})$  [70].

With the output estimate generated, the disturbance estimate is now updated according to the feedback rule

$$\hat{d}(t + 1) = \hat{d}(t) - \varepsilon L(\hat{y}(t) - y(t)),$$

where  $L \in \mathbb{R}^{q \times p}$  is the estimation gain and  $\varepsilon \in (0, 1)$  is a tunable parameter which controls the rate of adjustment. Putting everything together, we can compactly express the overall disturbance estimator as

$$\hat{y}(t) = \mathcal{P} \cdot \text{col}(u_{\text{ini}}, \hat{d}_{\text{ini}}, \hat{y}_{\text{ini}}, u(t), \hat{d}(t)) \quad (4.6a)$$

$$\hat{d}(t+1) = \hat{d}(t) - \varepsilon L(\hat{y}(t) - y(t)) \quad (4.6b)$$

where  $\mathcal{P} = Y_f \mathcal{H}_{\text{red}}^\dagger$  is the *prediction matrix* and  $\mathcal{H}_{\text{red}}^\dagger$  denotes the pseudoinverse of  $\mathcal{H}_{\text{red}}$ . As  $\mathcal{P}$  depends only on historical data, it can be computed once and stored, and thus implementing (4.6) simply amounts to matrix-vector multiplication.

The final issue to address concerns the tuning of the estimator gain  $L$  and parameter  $\varepsilon$  in (4.6). Our tuning recommendation is  $L = G(1)^\dagger$ , where  $G(1) = C(zI_n - A)^{-1}B_d|_{z=1}$  is the *DC gain* of the system (4.1) from input  $d$  to output  $y$ . This selection will be justified in our theory to follow, and while the matrix  $G(1)$  could be obtained empirically from repeated step response experiments, it can also be obtained directly from the exact same historical data used to construct the matrix  $\mathcal{P}$  in (4.6). The following result is an adaptation of [88, Thm. 4.1].

**Lemma 4.1.1 (DC Gain From Trajectory Data).** *Consider the previously defined historical data  $(u^d, y^d, d^d)$  and define*

$$\begin{aligned} y_d^{\text{diff}} &= (y^d(2) - y^d(1), \dots, y^d(T) - y^d(T-1)) \in (\mathbb{R}^p)^{T-1} \\ u_d^{\text{diff}} &= (u^d(2) - u^d(1), \dots, u^d(T) - u^d(T-1)) \in (\mathbb{R}^m)^{T-1} \end{aligned}$$

with associated Hankel matrices  $Y^{\text{diff}} = \mathcal{H}_{\ell(\mathcal{B})}(y_d^{\text{diff}})$  and  $U^{\text{diff}} = \mathcal{H}_{\ell(\mathcal{B})}(u_d^{\text{diff}})$ . Then

$$G_d(1) = Y_f \begin{bmatrix} Y^{\text{diff}} \\ U^{\text{diff}} \\ U_p \\ D_p \end{bmatrix}^\dagger \begin{bmatrix} 0 \\ 0 \\ 0 \\ I_q \end{bmatrix}.$$

We can now give a theoretical result concerning the convergence of the disturbance estimator (4.6).

**Theorem 4.1.2 (Data-Driven Disturbance Estimator).** *Consider the disturbance estimator (4.6) for the system (4.1) under all previous assumptions. Assume further that  $G(1) = C(I_n - A)^{-1}B_d$  has full column rank, and set the estimator gain as  $L = G(1)^\dagger$ . Then there exists  $\varepsilon^* > 0$  such that for all  $\varepsilon \in (0, \varepsilon^*)$ ,  $\hat{d}(t) \rightarrow d(t)$  exponentially as  $t \rightarrow \infty$ .*

The disturbance estimator (4.6) provides a *completely model-free* solution to disturbance estimation problem; the only required tuning is the single scalar parameter  $\varepsilon \in (0, 1)$ . An implication of Theorem 4.1.2 is that one may tune the estimator (4.6) by starting  $\varepsilon$  small and slowly increasing it; the proof can be found in Appendix A.2.

**Remark 4.1.3** (Singular Value Thresholding). *In practice, the system generating the data which is used to build  $\mathcal{H}_{\text{red}}$  in (4.6) may contain nonlinearity, and the measurements will be corrupted by measurement noise; this will be the case in our subsequent case studies. Both of these effects will compromise performance of the design (4.6). It has however been observed that low-rank approximations of Hankel matrices reduce the effects of noise in data-driven control, and enhance generalization [66]. In implementation, we compute the singular value decomposition of  $\mathcal{H}_{\text{red}}$  and retain only the dominant singular values and vectors, to obtain a low-rank approximation  $\tilde{\mathcal{H}}_{\text{red}}$  [89]. We then use  $\mathcal{P} = Y_f \tilde{\mathcal{H}}_{\text{red}}^\dagger$  in (4.6), which, empirically, greatly increases the robustness of the approach.  $\square$*

### 4.1.3 Design #2: Optimization-Based Data-Driven Disturbance Estimator

The advantage of (4.6) is simplicity, as it involves only linear update rules at each time step. We now outline a more flexible optimization-based disturbance estimation procedure which can achieve improved performance at the cost of higher implementation complexity. The key idea is to formulate the disturbance estimation problem as a regularized optimization problem. In particular, the use of regularization affords us more flexibility to select a better model class in terms of behaviour and complexity to better capture the dynamics of the true underlying system [87].

To begin, consider the previous development leading up to equation (4.5). Even if the system of equations (4.5) is consistent, it will generally have infinitely many solutions [68, 61]. The prediction matrix  $\mathcal{P}$  in (4.6) is given by  $\mathcal{P} = Y_f \mathcal{H}_{\text{red}}^\dagger$ , and corresponds precisely to taking the *least squares* solution of the first equation in (4.5) as

$$g^* = \underset{g}{\operatorname{argmin}} \quad \|g\|_2^2$$

$$\text{subject to } \mathcal{H}_{\text{red}} g = \operatorname{col}(u_{\text{ini}}, \hat{d}_{\text{ini}}, \hat{y}_{\text{ini}}, u(t), \hat{d}(t))$$

and then substituting to obtain  $\hat{y}(t) = Y_f g^*$ . When using noisy data from a non-LTI data-generating system, it is advantageous to robustify this least-squares problem by adding regularization [61]. To this end, for the equation  $\mathcal{H}_{\text{red}} g = \xi$ , we have

$$g = \mathcal{H}_{\text{red}}^\dagger \xi \quad \iff \quad (I - \mathcal{H}_{\text{red}}^\dagger \mathcal{H}_{\text{red}})g = 0.$$

Thus, with  $\mathcal{Q} = \mathcal{H}_{\text{red}}^\dagger \mathcal{H}_{\text{red}}$ , a least squares solution for  $g$  also arises from minimizing the objective function  $\|(I - \mathcal{Q})g\|_2^2$  subject to the linear constraint  $\mathcal{H}_{\text{red}} g = \xi$ .

Our disturbance estimation approach is now to *intentionally bias* this least squares solution, by introducing additional objective functions quantifying the prediction error along with regularization on  $g$ . This intentional biasing exploits the bias-variance trade-off from system identification [86], leading to reduced overfitting in the estimation procedure. With the same notation and set-up as in Section 4.1.2, at time  $t$  we solve the convex optimization problem

$$\begin{aligned} \min_{\hat{d}(t), \hat{y}(t), g} \quad & \|y(t) - \hat{y}(t)\|_2^2 + \lambda_1 \|(I - \mathcal{Q})g\|_2^2 + \lambda_2 \|g\|_2^2 \\ \text{s.t.} \quad & \begin{bmatrix} U_p \\ D_p \\ Y_p \\ U_f \\ D_f \\ Y_f \end{bmatrix} g = \begin{bmatrix} u_{\text{ini}} \\ \hat{d}_{\text{ini}} \\ y_{\text{ini}} \\ u(t) \\ \hat{d}(t) \\ \hat{y}(t) \end{bmatrix}, \end{aligned} \tag{4.7}$$

where  $\lambda_1, \lambda_2 \geq 0$  are tuning parameters. The problem (4.7) combines the prediction and estimation steps from (4.6) into one formulation, jointly generating the output prediction  $\hat{y}(t)$  and the disturbance estimate  $\hat{d}(t)$ . The first objective function term attempts to match the prediction  $\hat{y}(t)$  to the measured output  $y(t)$ . Increasing  $\lambda_1$  encourages a least-squares solution for  $g$ , similar to that used in (4.6), while increasing  $\lambda_2$  regularizes the solution; this reduces overfitting [86] and improves estimation robustness for noisy measurements and non-LTI dynamics. This approach is strongly justified by recent advances in regularized data-driven control [87], and performance will be extensively tested in Section 4.2.

#### 4.1.4 Specialization to Area-Based Fast Frequency Control using Inverter-Based Resources

We now describe the adaptation of our general data-driven disturbance estimation methods to the fast frequency control architecture described in Section 3. Consider a large interconnected power system which is divided into several small LCAs. Each LCA has local IBR's that can be re-dispatched by the operator, subject to their real-time capacity limits. Since each LCA is geographically small, the effect of a power imbalance within the LCA on the frequency is approximately independent of the specific nodal location of the imbalance within the LCA. Therefore, it is assumed that power disturbances and generation are aggregate, and effectively lumped at a single bus. Put differently, disturbance and control signals enter through the same channel, and thus  $B = B_d \in \mathbb{R}^{n \times 1}$  in (4.1).

The following selections are made for inputs and outputs: the measurement  $y(t) = \Delta\omega(t) \in \mathbb{R}$  is a single local measurement of frequency deviation, and the disturbance  $d(t) = \Delta P_u \in \mathbb{R}$  models aggregate unmeasured generation-load imbalance within the LCA. The input  $u(t)$  to the system consists of the measured tie-line flow  $\Delta P_{\text{tie}}(t)$  out of the LCA, as well as the sum of all IBR power set-points  $\Delta P_{\text{ibr}}(t)$ .

Historical data must be used to build the Hankel matrices used in both estimators. As the control and disturbance channels are lumped, during the collection of historical data, the sum of IBR set-point changes, exogenous load/generation changes, and inter-LCA tie-line flow changes must be recorded. Further discussion of options for data collection is deferred to Section 4.2.1.

As a result of the above, the estimator (4.6) simplifies to

$$\Delta \hat{f}(t) = \mathcal{P} \cdot \text{col}(\Delta v_{\text{ini}}, \Delta \hat{f}_{\text{ini}}, \Delta v(t)) \quad (4.8a)$$

$$\Delta \hat{P}_u(t+1) = \Delta \hat{P}_u(t) - \varepsilon L(\Delta \hat{f}(t) - \Delta f(t)), \quad (4.8b)$$

where  $\Delta v = \Delta P_{\text{ibr}} - \Delta P_{\text{tie}} - \Delta P_u$ , is the aggregated input,  $\mathcal{P} = Y_f [U_p; Y_p; U_f]^\dagger$ , is the prediction matrix, and  $L \in \mathbb{R}$  is now a scalar. Analogously, the optimization-based estimator (4.7) becomes

$$\begin{aligned} \min \quad & \|\Delta f(t) - \Delta \hat{f}(t)\|_2^2 + \lambda_1 \|(I - \mathcal{Q})g\|_2^2 + \lambda_2 \|g\|_2^2 \\ \text{s.t.} \quad & \begin{bmatrix} U_p \\ Y_p \\ U_f \\ Y_f \end{bmatrix} g = \begin{bmatrix} \Delta P_{\text{ibr,ini}} - \Delta P_{\text{tie,ini}} - \Delta \hat{P}_{u,\text{ini}} \\ \Delta f_{\text{ini}} \\ \Delta P_{\text{ibr}}(t) - \Delta P_{\text{tie}}(t) - \Delta \hat{P}_u(t) \\ \Delta \hat{f}(t), \end{bmatrix}, \end{aligned} \quad (4.9)$$

The imbalance estimate  $\Delta \hat{P}_u(t)$  from either method is then used to redispatch the local IBRs in the LCA via the optimal power allocation algorithm presented in [90].

## 4.2 Simulation Studies

We validate our designs by applying them to the three-area nonlinear test system illustrated in Figure 4.1. Each LCA of the test system is based on the the IEEE 3-machine 9-bus system given in [21], with the interconnection parameters and active power dispatch info similar to [90]. In the modified test model, two synchronous generators (SGs) in area one have been replaced with a photovoltaic (PV) array and a Wind (WT) plant. Similarly, one SG each in areas two and three are replaced with a PV farm. The PV array and

wind turbine plant are simplified models represented by non-dispatchable converter-based units, which are parameterized using wind power and solar irradiance data from [2, 1]. To facilitate frequency control, two dispatchable IBRs have been added in each LCA. In addition, static var compensators (SVCs) and synchronous condensers have been added to areas 1 and 2/3 to support the voltage. All SGs and dispatchable IBRs in the system are set to have a 5% speed droop curve on their respective bases, with a 36 mHz primary control deadband. The pre-disturbance generation/demand in the system is approximately 800 MW.

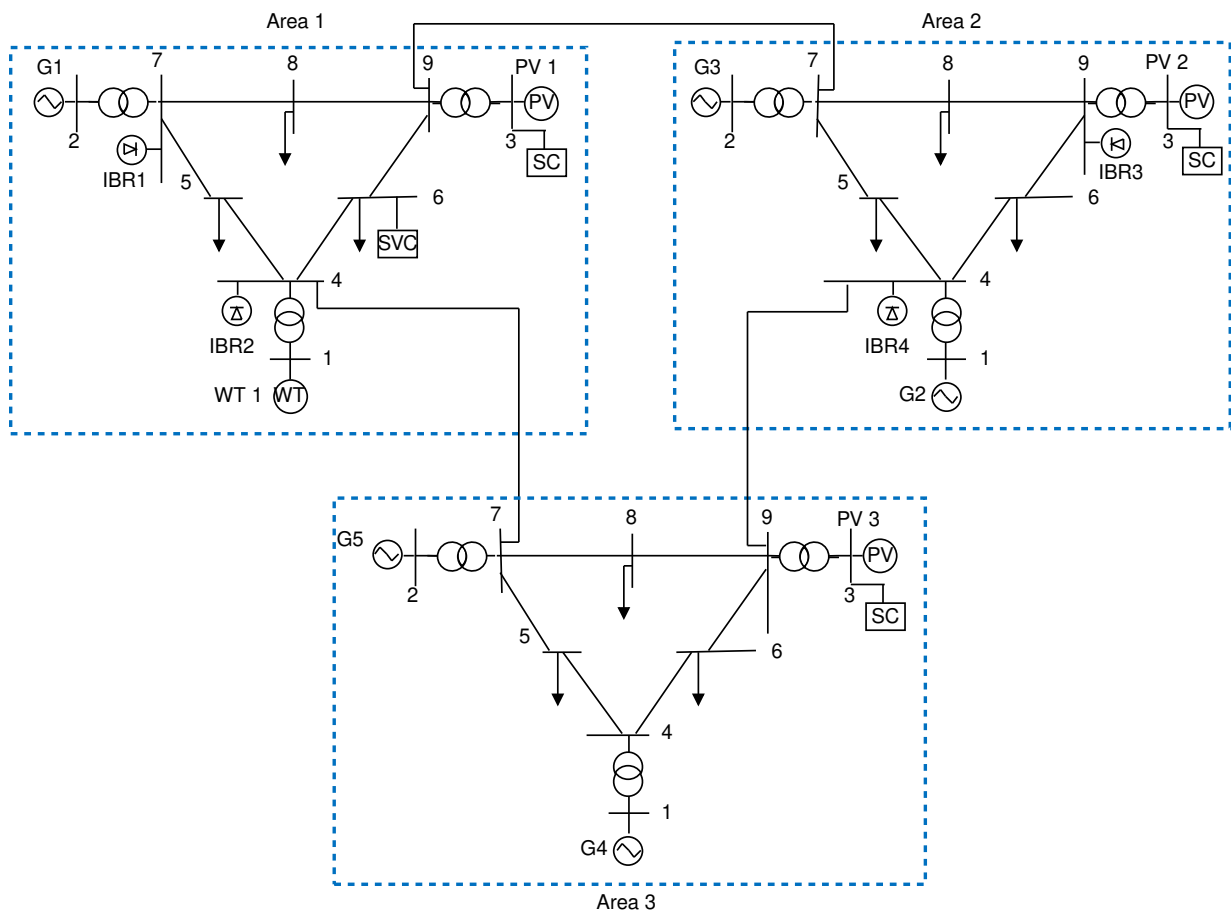


Figure 4.1: Three-LCA test system.

### 4.2.1 Offline Data Collection and Controller Tuning

As described in Section 3.2, our estimators require a library of historical data generated from a *persistently exciting input* that must be collected *before* the online implementation of the control. Examples of common persistently exciting inputs from the literature include, pseudo random binary sequence, autoregressive moving average sequence, sum of sinusoids, and white noise [91, 92]. Among these, white-noise derivatives are most commonly used in power system identification studies, such as measured ambient power fluctuations [93], and low-power injected probing signals such as the low-level pseudo-random noise (LLPRN) in [94] and the band-limited white noise in [95]. In terms of what sources should be actuated for this data collection, there are several theoretically-equivalent options for the purposes of this work, including

- (i) apply low-power probing modulations to IBRs during calm system conditions (i.e., during times of minimal unmeasured generation/load changes), and meter the resulting frequency and tie-line power changes,
- (ii) hold IBR set-points constant, record ambient load power consumption changes (or injected pseudo random white noise that mimics such changes), and meter the resulting frequency and tie-line power changes,

or obvious variations/combinations of these. In our testing to follow, we pursue option (i); we refer the reader to Remark 3.3.1 in Section 3 for a discussion on the feasibility and market incentives that makes this choice viable.

We now turn to the design of the low-power probing signal for IBR set-point changes. In this work, we modeled our probing injection signal after the LLPRN in [94], where we have combined a sum of sinusoids and band-limited white noise. Each IBR within each LCA is commanded with the set-point changes shown in Figure 4.2, given by

$$\Delta P_{\text{ibr}}(t) = \sin(12\pi t) + w(t) \quad (\text{in MW}). \quad (4.10)$$

The signal consists of a sinusoidal perturbation of 1 MW ( $1.76 \times 10^{-3}$  p.u.), with band-limited white noise  $w(t)$  with noise power of  $\approx 0.2 \times 10^{-3}$  p.u.

While we stress that the choice of probing signal is not unique, with our choice of signal, we are able to utilize the aggregated power input  $u = \Delta P_{\text{ibr}} - \Delta P_{\text{tie}}$  and output  $y = \Delta \omega$  data for each LCA recorded for only 10 seconds at a sampling rate of 0.1 seconds, which is significantly shorter than the duration of 1200 seconds for ambient data and 600 seconds for LLPRN reported in the literature [94].

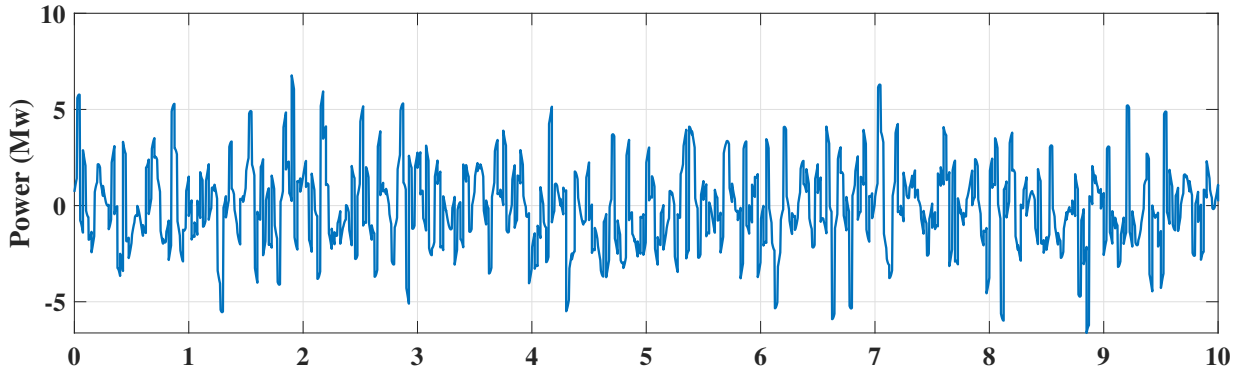


Figure 4.2: Persistently exciting IBR set-point change for data collection phase.

Regarding the tuning parameters, we used  $T = 101$  historical data points for each LCA, collected sequentially with only one LCA being excited at a time. The length of recent past data used in (4.8) and (4.9) was  $T_{\text{ini}} = 7$ ; larger values were found to produce no benefit. The controller gain  $\varepsilon$  in (4.8) was set via tuning to  $\varepsilon = 0.2$  by starting from a small value and increasing until satisfactory performance was reached. For the penalty parameters in (4.9), we set  $\lambda_1$  to a large value of  $1 \times 10^8$ , according to the insights from Section 4.1.3, and  $\lambda_2 = 1 \times 10^2$  was set via tuning by gradually increasing its value until no noticeable improvement in performance was observed.

## 4.2.2 Simulation Scenarios

We consider four different testing scenarios, which aim to highlight the diverse challenges that can arise in a power system, including renewable resource variability, sudden changes in load demand, and equipment failures. The scenarios are

- (1) response to sudden load changes of different sizes,
- (2) response to solar and wind farm variability,
- (3) response to a three-phase-to-ground fault, and
- (4) response after loss of a conventional generation unit.

For all scenarios, we integrate our disturbance estimators into the hierarchical fast frequency control architecture proposed in Section 3 and compare the model-based disturbance estimator of that Section against the data-driven disturbance estimators presented

here. We term the controller described in (4.8) as the Linear Data-Driven Disturbance Estimator (LDDE) and that in (4.9) as the Optimization-Based Data-Driven Disturbance Estimator (ODDE); the ODDE is the default data-driven controller presented in the figures when no other context is given. As a baseline, we compare to the response without any supplementary control scheme, where frequency support is provided only through the primary droop control action of both generators and IBRs. Additionally, we compare against the response obtained by implementing standard automatic generation control (AGC) on the three-area system in Figure 4.1. In Scenario #1, we have compared the ODDE against all the alternatives listed above, and demonstrate its performance premium relative to the LDDE. In the remainder of the scenarios, we focus the plots on comparing the better estimator (ODDE) against the model-based approach presented in Section 3. Finally, the data collection and real-time simulation steps include measurement noise, modelled as zero-mean white noise of standard deviation  $10^{-6}$  p.u. for frequency deviation and  $2 \times 10^{-2}$  p.u. for inter-area power flow measurements; these represent realistic noise on the variables scaled for their typical values (e.g., [95]).

### 4.2.3 Scenario #1: Step Load Changes

This scenario evaluates the performance of our controller in response to step load changes of varying magnitudes – 14 MW and 60 MW – applied in Area 2.

At  $t = 10$ s, a small load change of 14 MW is applied at bus 8 in area two. The size of the disturbance is chosen such that the resulting frequency deviation is below the 36 mHz deadband of the generator primary control systems. The frequency response and disturbance estimate of the system are plotted in Figure 4.3, while the net-tie line deviations and IBR power outputs are displayed in Figure 4.5. For clarity in differentiating the alternative approaches, a zoomed-in frequency response plot is shown in Figure 4.4.

Using both the model-based and data-driven disturbance estimators, the disturbance was quickly identified to originate in Area 2 and promptly corrected by adjusting the setpoints of the local IBRs, with minimal impact on other areas. Overall, the frequency was restored quickly, and the variables in the non-contingent areas returned to their pre-disturbance state due to the decentralized nature of the control scheme. The plots also demonstrate that the proposed optimization-based data-driven estimator outperforms the linear data-driven and model-based estimators in terms of a higher nadir and faster settling time for the post-contingency frequency. We believe the improved performance of the optimization-based estimator relative to the linear estimator is due to its ability to better capture the dynamics of the true underlying system in terms of behaviour and complexity.

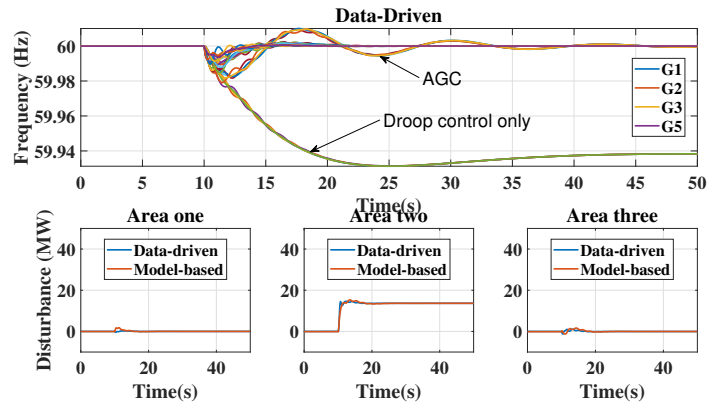


Figure 4.3: Frequency and disturbance estimate during a 14 MW load change at bus 8 in Area 2.

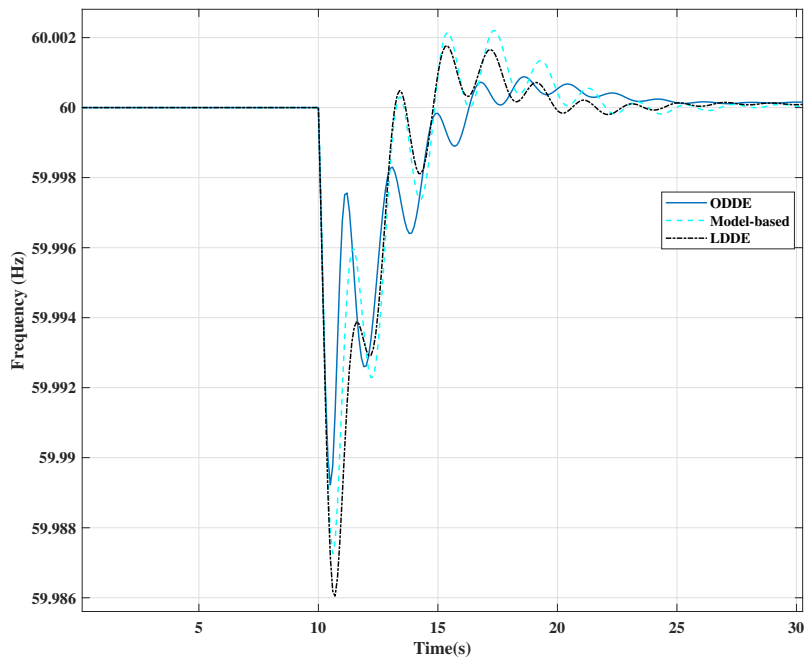


Figure 4.4: Zoomed-in frequency plot of the contingent area showing the control alternatives during a 14 MW load change at bus 8 in Area 2.

The plots in Figures 4.6, 4.7, and 4.8, which display the frequency response, disturbance estimate, net tie-line deviations, and IBR outputs in response to a step load change of 60 MW applied at bus 8 in Area 2 at  $t = 10s$ , lead to the same conclusion about the controller's

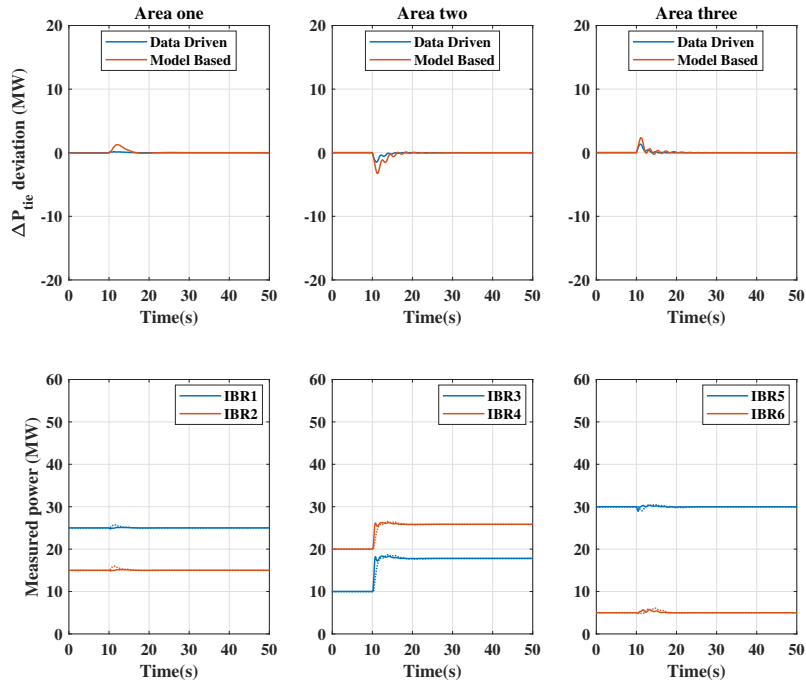


Figure 4.5: Tie-line deviation and active power profiles during a 14 MW load change; dashed lines in the lower plots indicate the responses under model-based estimation. performance as the previous scenario with a 14 MW load change. This demonstrates that the proposed controller exhibits superior performance for step load changes both inside and outside the governor deadband range.

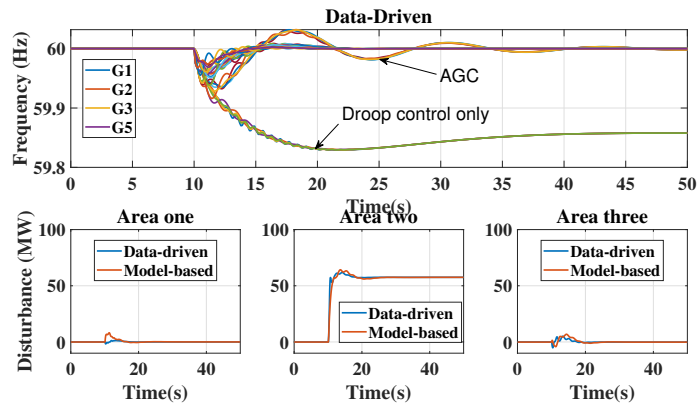


Figure 4.6: Frequency and disturbance estimate during a 60 MW load change at bus 8 in Area 2.

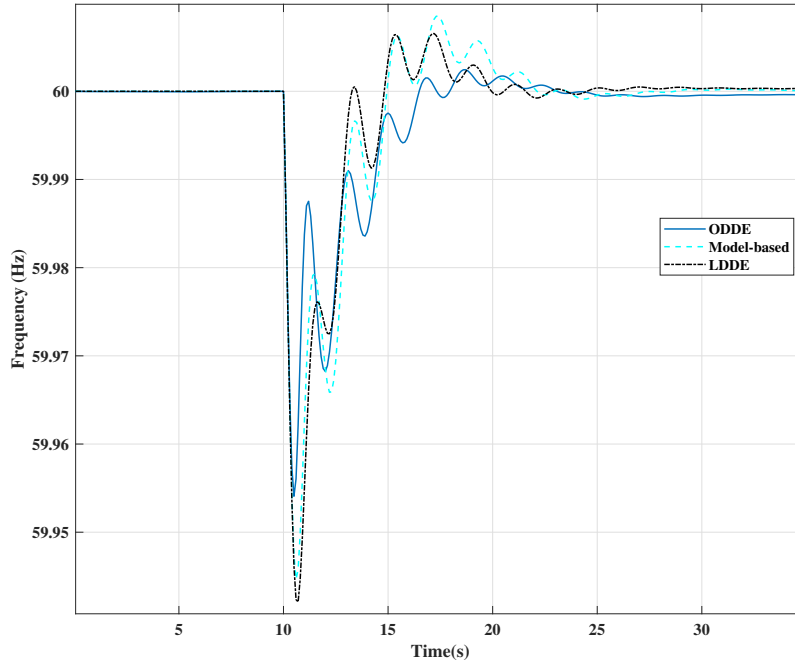


Figure 4.7: Zoomed-in frequency plot of the contingent area showing the control alternatives during a 60 MW load change at bus 8 in Area 2.

In general, the results show that the robust data-driven approach presented in this study outperforms the model-based approach and other alternatives, quickly localizing and compensating for large and small disturbances.

#### 4.2.4 Scenario #2: High Renewable Resource Fluctuations

In this scenario, we aim to demonstrate the effectiveness of our data-driven approach in the presence of renewable variability using realistic wind and solar irradiance data. To simulate the solar irradiance component, we use data from the Oahu solar measurement grid 1-year archive [1], containing 1-second measurements of solar irradiance. We select a slice of data from July 31, 2010 (see Figure 4.9). These values are used to simulate a converter-interfaced PV farm in Area 2.

For the wind farm component, we use 4-second resolution wind power measurements from the wind power dataset accessible at [2], originally obtained from the Australian Energy Market Operator (AEMO). We select a slice of data from August 15, 2019 (see Figure 4.9). These values are used to simulate a converter-interfaced wind farm in Area 1.

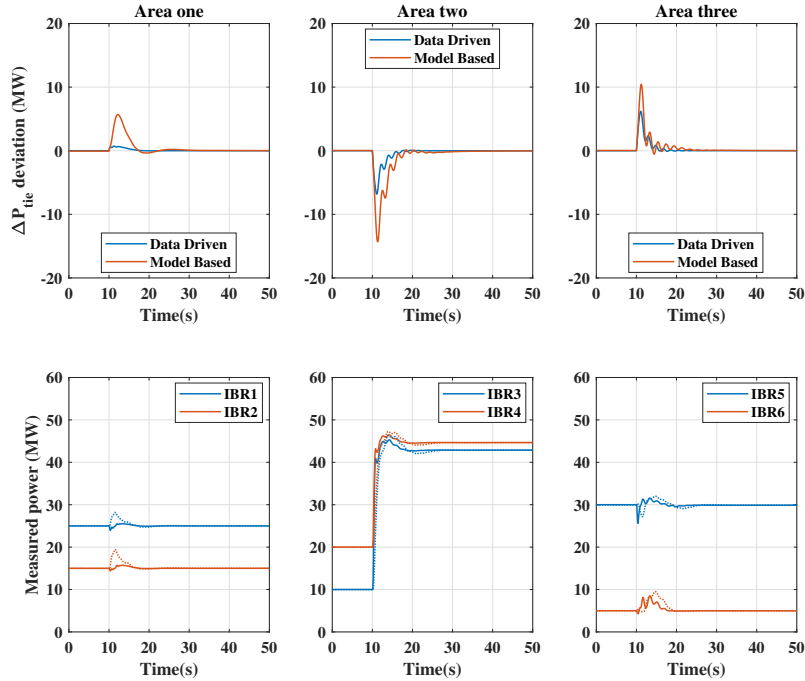


Figure 4.8: Tie-line deviation and active power profiles during a 60 MW load change; dashed lines in the lower plots indicate the responses under model-based estimation.

At  $t = 10s$ , we introduce a step load change of 40 MW in Area 2 and simultaneously introduce the new the solar irradiance levels and wind power in accordance with the real-world data. The frequency response, disturbance estimate, net tie-line deviations, and IBR outputs of the power system for this scenario are displayed in Figures 4.10, 4.11, and 4.12.

The simulation results show that the optimization-based data-driven estimator is able to quickly estimate the highly variable power imbalance in real-time, allowing the frequency to be kept close to the nominal value throughout the simulation period. The performance of our designed data-driven estimator is quantified in Table 4.1, which shows the root mean squared frequency deviation for each generator in the system. The results show that the data-driven disturbance estimator with regularization performs the best.

### 4.2.5 Scenario #3: Symmetric Three-Phase Fault

The essence of this scenario is to assess the performance of our control approach under a severe contingency like a symmetrical three-phase line-to-ground fault. The response of the system during the fault introduced at bus 8 in Area 2 at  $t = 2s$  and cleared after 0.1s is

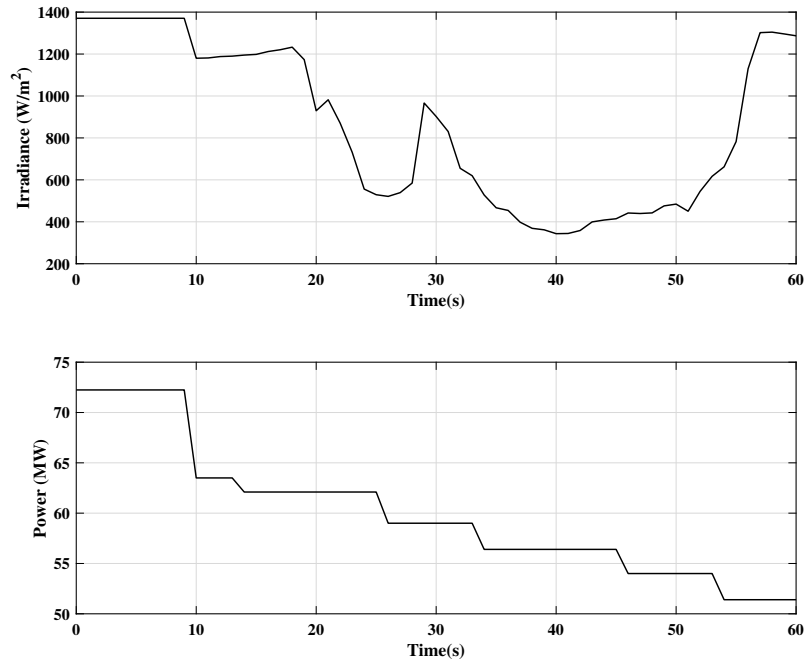


Figure 4.9: Solar irradiance and wind power data representing suitably scaled slices of data on 31 July 2010 and 15 Aug 2019 from [1] and [2] repositories.

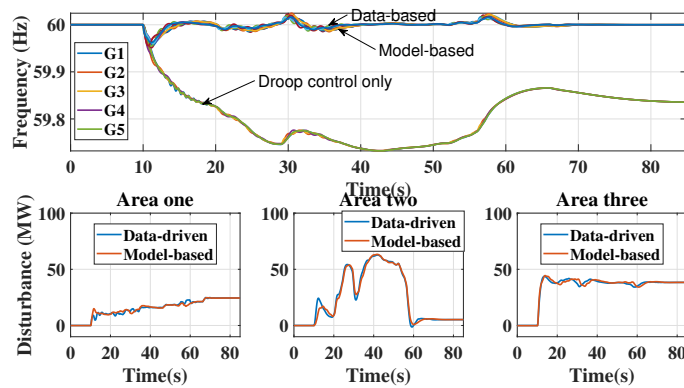


Figure 4.10: Frequency and disturbance estimate during high renewable resource fluctuations in multiple areas.

shown in Figures 4.13 and 4.14. Note that despite the transients, the controller is able to discern that there is no net load imbalance within the area. The results indicate that the controller is able to effectively detect and respond to frequency events, and the data-driven

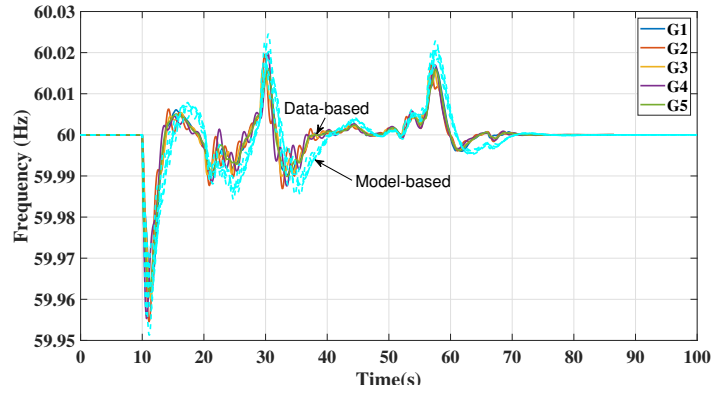


Figure 4.11: Zoomed-in frequency plot during high renewable resource fluctuations in multiple areas.

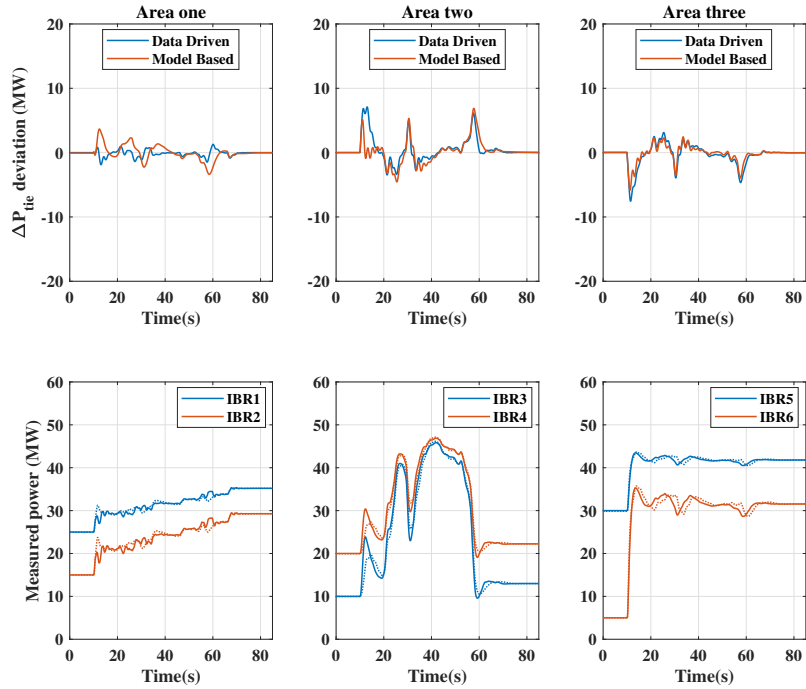


Figure 4.12: Tie-line deviation and active power profiles during high renewable resource fluctuations in multiple areas.; dashed lines in the lower plots indicate the responses under model-based estimation.

estimator’s performance is satisfactory and similar to the model-based estimator.

Control type	RMSE (Hz)					Total (Hz)
	G1	G2	G3	G4	G5	
Data-based w/ reg.	0.0065	0.0065	0.0064	0.0066	0.0065	<b>0.0325</b>
Data-based w/o reg.	0.0071	0.0073	0.0072	0.0074	0.0073	0.0365
Model-based	0.0081	0.0081	0.0080	0.0080	0.0081	0.0403
AGC	0.0236	0.0225	0.0233	0.0225	0.0233	0.1151
Droop only	0.1885	0.1883	0.1884	0.1884	0.1884	0.9420

Table 4.1: Root Mean Square Error for Control Alternatives.

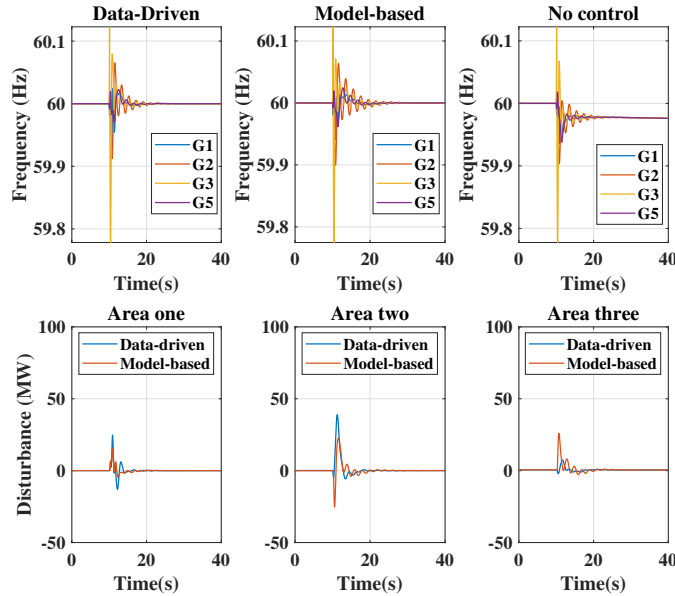


Figure 4.13: Frequency and disturbance estimate during a three-phase fault in Area 2.

#### 4.2.6 Scenario #4: Loss of Generator

This scenario assesses the performance of our control approach under the loss of generator G2 in area 2 at  $t = 10s$ . When the generator G2 is lost, the system experiences a disturbance, and the controllers respond to correct the resulting power imbalance. The response of the system under both the model-based and data-driven control is plotted in Figure 4.15. According to the findings, the data-driven controller outperforms the model-based controller, as demonstrated by its faster frequency settling time and lower overshoot. Importantly, despite the data used to design the LCA controller having been collected while

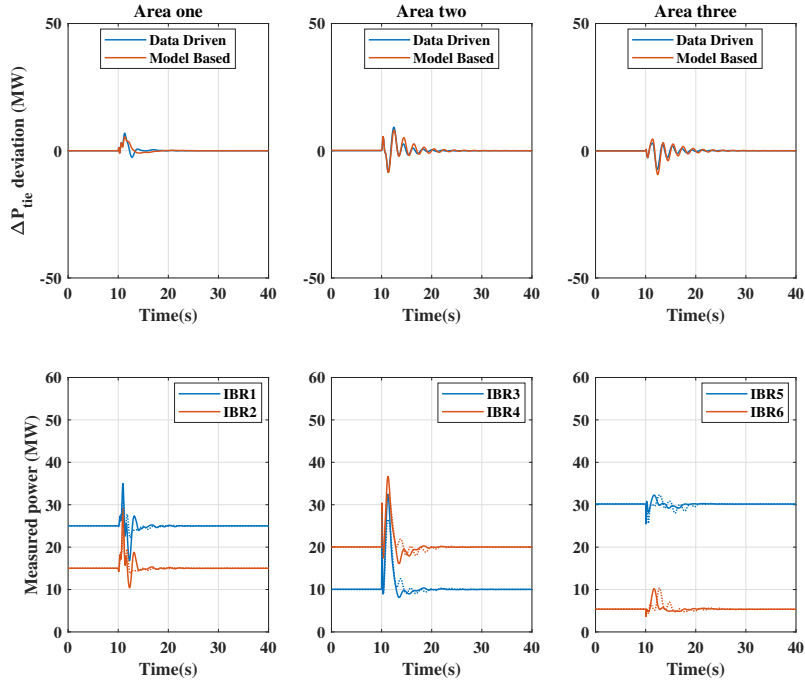


Figure 4.14: Tie-line deviation and active power profiles during a three- phrase fault in Area 2; dashed lines in the lower plots indicate the responses under model-based estimation.

G2 was online, the response indicates that the data-driven controller is effective even in the face of significant changes in power system composition and frequency response dynamics. This illustrates the robustness of the design, and provides flexibility for system operators in deciding how frequently they wish to collect new data to update the controller.

### 4.3 Summary

We have proposed and validated through detailed simulations a robust data-driven disturbance estimator that allows us to reliably compute the real-time power imbalance in a highly nonlinear power system, and in the presence of measurement noise. This data-driven estimate has been integrated into the hierarchical frequency control architecture initially proposed in Section 3, to provide a completely model-free approach to provide fast, localized frequency regulation in the power system.

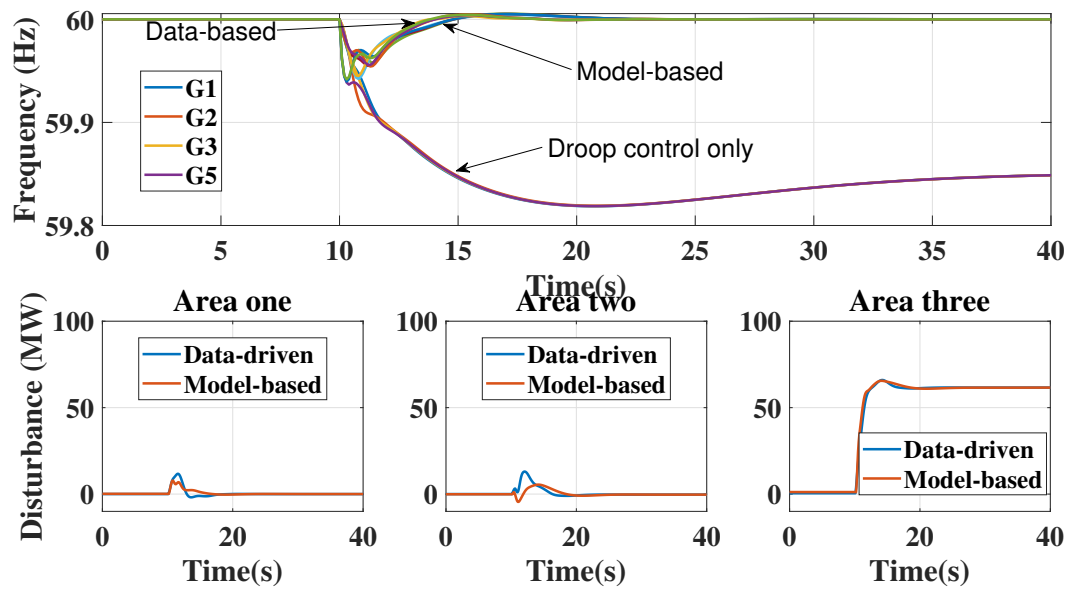


Figure 4.15: Frequency and disturbance estimate during a generator G4 loss in Area 3.

# Chapter 5

## Conclusion

### 5.1 Summary

This work is centered on next-generation grids, where the increased integration of inverter-based resources (IBRs) will play a crucial role in power system control, and where generation may even consist entirely of inverter-connected renewable resources (RESs). In these grids, the sensing ability and control authority will be dispersed over many more devices than previously, necessitating increased decentralization to manage the resulting information flows and respond to them swiftly. When this is combined with the load variability and uncertainty introduced by these IBRs, the need for control paradigms that incorporate rapid localized control with high-bandwidth wide-area coordination becomes increasingly important.

The first novelty of our approach lies in the layered control architecture, providing fast, localized control in response to local power imbalances, supplemented by wide-area coordination. Traditionally, the automatic generation control (AGC) system uses a centralized approach to keep average frequency deviations within acceptable limits for each balancing authority area. However, due to the extensive size of these areas, maintaining an accurate dynamic system model becomes a challenging task. As a result, the AGC system relies on classical frequency bias constant methods, which, while somewhat effective, limit its speed and efficacy for rapid frequency control. In contrast, our architecture divides a power system into smaller local control areas (LCAs), within which high-bandwidth, low-latency measurements are available for local decision-making. A higher coordinating layer manages these LCAs to ensure a continued global power balance during contingencies where the local capacity might be insufficient. This reduction in spatial scale enables

increased decentralization of control actions and allows for the use of a dynamic model representation of the area for design purposes. Overall, this layered control architecture allows greater flexibility in designing the individual layers, and local handling of information leads to faster and more efficient control responses, greater data privacy, reduced latency, and smaller communication payload.

The second novelty lies in the coordination and control of fast-acting IBRs to correct local power imbalances from so-called frequency events. An approach to fast frequency control suggested in the literature [96, 97, 98] is the use of distributed averaging (consensus-based) methods. In these, distributed energy resources act as multi-agent systems that support frequency regulation while fulfilling system-wide objectives, especially in primary droop control scenarios. This technique is promising due to its relatively low implementation complexity. However, it necessitates a comprehensive peer-to-peer communication architecture, which could introduce more time delays. This is particularly relevant as the number of distributed energy resources in the grid is projected to increase in the future. Although several authors [99, 100, 83, 84, 101, 102] have taken another approach towards proposing fast frequency response (FFR) methods for low-inertia systems, which aim to provide controlled frequency support to the system by acting rapidly on a frequency measure to compensate for the lost inertial and governor-turbine response from conventional synchronous generators, most of these focus on the potential of utilizing a range of emerging technologies in providing FFRs, and on the specific technology or energy source being considered. However, as the grid and its associated technologies are still evolving, there is a need for a technology-agnostic, modular framework that provides fast frequency control while optimally coordinating the available grid resources. Our disturbance estimation and rejection techniques, in addition to the layered control architecture, provide this modular framework. For each LCA in our scheme, we designed a fast local disturbance estimation and rejection control loop. This loop processes local measurements and quickly re-dispatches local IBRs and other legacy power sources to balance local generation and net-load. While fast-acting IBRs can currently provide droop support and virtual inertia emulation, our scheme offers additional supplementary power injection on a fast time scale, acting as an additional fast primary and secondary control, which we believe will become increasingly important in future IBR-dominated grids, as they are expected to face more frequent and severe frequency excursions.

Designing our fast local disturbance estimation and rejection control loops to provide optimal dynamic performance requires a rich, and reasonably accurate, representative model of the LCAs. However, due to the increasing scale, complexity, and changing dynamics of power systems, ensuring the accuracy of system models is a significant challenge. To address this, we have presented novel designs for data-driven disturbance estimators,

which allow us to produce real-time estimates of the net real power imbalance within an LCA using only historical data sequences and online measurements.

The combination of our data-driven local disturbance estimation and rejection techniques and the proposed layered architecture has allowed us to propose an effective approach to fast frequency control for next-generation IBR-dominated grids. We have extensively validated our scheme through simulations on detailed nonlinear multi-LCA test power systems. The tests indicate that the scheme offers fast, localized, and non-oscillatory frequency control for the bulk grid.

## 5.2 Future Research Directions

Our near-term future work will focus on enhancing the current scheme. Specifically, we aim to improve the implementation of the global power balancing layer in terms of decentralized power support and speed of convergence. We plan to examine the feasibility of using a peer-to-peer strategy for additional power-sourcing support, quantify its performance limits, and assess its communication and measurement requirements. Moreover, we will conduct investigations into the design of improved excitation input signals with the goal of minimizing system disruption during the data collection phase.

The logical next step for our decentralized hierarchical control scheme is to facilitate the participation of active power sources at the distribution level, thereby creating an integrated approach that coordinates both transmission and distribution assets. However, beyond the optimal coordination of distributed energy resources (DERs) at the distribution level, we also need to address the issue of aggregation. Optimal aggregations that can manage the operations of small-scale DERs, optimize their performance, and interact with the higher-level controller at the transmission level will need to be investigated. Moreover, as the underlying communication infrastructure for information flows between the spatially disparate DER units is integral, we should consider redesigning the scheme from the ground up as a coordination strategy for a cyber-physical system. Here, issues such as cybersecurity and network packet loss need to be studied and addressed. The successful integration of this system not only involves technical challenges but also regulatory and market hurdles. For instance, it's vital to address issues such as the necessary incentives required to promote a thriving market for auxiliary services that are IBR and DER friendly. Lastly, it will be essential to develop new simulation tools for the large-scale cyber-physical grid to aid validation and explore the unavoidable trade-offs required.

Thirdly, we plan to explore the potential integrated multi-input and multi-output (MIMO) control design formulation that simultaneously addresses the joint frequency and

voltage control issues. As frequency control becomes faster, the interactions with system voltage dynamics increase. This interaction, particularly important in the context of voltage-dependent power consumption of loads such as impedance-type loads, is documented in our previous work [17].

# References

- [1] M. Sengupta and A. Andreas, “Oahu solar measurement grid (1-year archive): 1-second solar irradiance; oahu, hawaii (data),” tech. rep., National Renewable Energy Lab.(NREL), Golden, CO (United States), 2010.
- [2] R. Godahewa, C. Bergmeir, G. Webb, M. Abolghasemi, R. Hyndman, and P. Montero-Manso, “Wind power dataset (4 seconds observations),” 8 2020.
- [3] D. Gielen, F. Boshell, D. Saygin, M. D. Bazilian, N. Wagner, and R. Gorini, “The role of renewable energy in the global energy transformation,” *Energy Strategy Reviews*, vol. 24, pp. 38–50, 2019.
- [4] IRENA, “Global energy transformation: A roadmap to 2050,” 2018.
- [5] C. B. Vellaithurai, S. S. Biswas, R. Liu, and A. Srivastava, “Real time modeling and simulation of cyber-power system,” in *Cyber physical systems approach to smart electric power grid*, pp. 43–74, Springer, 2015.
- [6] E. Ekomwenrenren, H. Alharbi, T. Elgorashi, J. Elmirghani, and P. Aristidou, “Stabilising control strategy for cyber-physical power systems,” *IET Cyber-Physical Systems: Theory & Applications*, vol. 4, no. 3, pp. 265–275, 2019.
- [7] V. C. Gungor, D. Sahin, T. Kocak, S. Ergut, C. Buccella, C. Cecati, and G. P. Hancke, “A survey on smart grid potential applications and communication requirements,” *IEEE Transactions on industrial informatics*, vol. 9, no. 1, pp. 28–42, 2012.
- [8] J. Kosowatz, “Energy storage smooths the duck curve,” *Mechanical Engineering*, vol. 140, no. 06, pp. 30–35, 2018.
- [9] A. Ulbig, T. S. Borsche, and G. Andersson, “Impact of Low Rotational Inertia on Power System Stability and Operation,” vol. 47, (Cape Town, South Africa), pp. 7290–7297, Aug. 2014.

- [10] F. Milano, F. Dörfler, G. Hug, D. J. Hill, and G. Verbič, “Foundations and challenges of low-inertia systems,” pp. 1–25, 2018.
- [11] B. K. Poolla, S. Bolognani, and F. Dörfler, “Optimal placement of virtual inertia in power grids,” vol. 62, no. 12, pp. 6209–6220, 2017.
- [12] Q. Hong, M. Nedd, S. Norris, I. Abdulhadi, M. Karimi, V. Terzija, B. Marshall, K. Bell, and C. Booth, “Fast frequency response for effective frequency control in power systems with low inertia,” vol. 2019, no. 16, pp. 1696–1702, 2019.
- [13] A. Chakraborty, “Wide-area communication and control: A cyber-physical perspective,” in *Smart Grid Control*, pp. 139–164, Springer, 2019.
- [14] Y. Zhao, T. Liu, and D. J. Hill, “A data-enabled predictive control method for frequency regulation of power systems,” in *IEEE PES Innovative Smart Grid Technologies Conference Europe*, pp. 01–06, IEEE, 2021.
- [15] Z. Tang, E. Ekomwenrenren, J. W. Simpson-Porco, E. Farantatos, M. Patel, and H. Hooshyar, “Measurement-based fast coordinated voltage control for transmission grids,” *IEEE Transactions on Power Systems*, vol. 36, no. 4, pp. 3416–3429, 2020.
- [16] Z. Tang, E. Ekomwenrenren, J. W. Simpson-Porco, E. Farantatos, M. Patel, A. Haddadi, and H. Hooshyar, “Data-driven extension of “measurement-based fast coordinated voltage control for transmission grids”,” *IEEE Transactions on Power Systems*, vol. 38, no. 1, pp. 948–951, 2022.
- [17] E. Ekomwenrenren, Z. Tang, J. W. Simpson-Porco, E. Farantatos, M. Patel, H. Hooshyar, and A. Haddadi, “An integrated frequency-voltage controller for next-generation power systems,” in *2022 IEEE PES Innovative Smart Grid Technologies Conference Europe (ISGT-Europe)*, pp. 1–6, IEEE, 2022.
- [18] L. Bird, M. Milligan, and D. Lew, “Integrating variable renewable energy: Challenges and solutions,” tech. rep., National Renewable Energy Lab.(NREL), Golden, CO (United States), 2013.
- [19] R. Yan, T. K. Saha, F. Bai, H. Gu, *et al.*, “The anatomy of the 2016 south australia blackout: A catastrophic event in a high renewable network,” vol. 33, no. 5, pp. 5374–5388, 2018.
- [20] J. Gilmore, T. Nolan, and P. Simshauser, “The levelised cost of frequency control ancillary services in australia’s national electricity market,” 2022.

- [21] P. M. Anderson and A. A. Fouad, *Power system control and stability*. John Wiley & Sons, 2008.
- [22] P. Kundur, N. J. Balu, and M. G. Lauby, *Power system stability and control*, vol. 7. McGraw-hill New York, 1994.
- [23] O. Stanojev, U. Markovic, P. Aristidou, G. Hug, D. Callaway, and E. Vrettos, “Mpc-based fast frequency control of voltage source converters in low-inertia power systems,” *IEEE Transactions on Power Systems*, vol. 37, no. 4, pp. 3209–3220, 2020.
- [24] J. Matevosyan, J. MacDowell, N. Miller, B. Badrzadeh, D. Ramasubramanian, A. Isaacs, R. Quint, E. Quitmann, R. Pfeiffer, H. Urdal, *et al.*, “A future with inverter-based resources: Finding strength from traditional weakness,” *IEEE Power and Energy Magazine*, vol. 19, no. 6, pp. 18–28, 2021.
- [25] F. Van Hulle, H. Holttinen, J. Kiviluoma, M. Faiella, P. Kreutzkamp, N. Cutululis, M. Rekinge, A. Gubina, F. Chapalain, B. Ernst, S. Wachtel, G. Quinonez Varela, D. Craciun, I. Pineda, B. Stoffer, J. Corbett, and A. Flament, *Grid support services by wind and solar PV: a review of system needs, technology options, economic benefits and suitable market mechanisms: Synthesis report of the REserviceS project*. 2014.
- [26] J. Aho, A. Buckspan, J. Laks, P. Fleming, Y. Jeong, F. Dunne, M. Churchfield, L. Pao, and K. Johnson, “A tutorial of wind turbine control for supporting grid frequency through active power control,” in *2012 American Control Conference (ACC)*, pp. 3120–3131, IEEE, 2012.
- [27] Elkraft System and Eltra, “Wind Turbines Connected to Grids with Voltages Above 100kV: Technical regulation for the properties and the regulation for wind turbines,” tech. rep., Erritsø, Denmark, 2003.
- [28] J. Aho, L. Pao, and P. Fleming, “An active power control system for wind turbines capable of primary and secondary frequency control for supporting grid reliability,” in *51st AIAA Aerospace Sciences Meeting including the New Horizons Forum and Aerospace Exposition*, p. 456, 2013.
- [29] A. D. Hansen, “Evaluation of power control with different electrical and control concept of wind farm: Part 2–large systems,” 2010.
- [30] R. E. de España *et al.*, “Transmission system operation with a large penetration of wind and other renewable electricity sources in electricity networks using innovative

tools and integrated energy solutions (twenties),” tech. rep., Madrid, Spain, Final Rep., Oct, 2013.

- [31] M. Dreidy, H. Mokhlis, and S. Mekhilef, “Inertia response and frequency control techniques for renewable energy sources: A review,” *Renewable and Sustainable Energy Reviews*, vol. 69, pp. 144–155, Mar. 2017.
- [32] A. Banshwar, N. K. Sharma, Y. R. Sood, and R. Shrivastava, “Renewable energy sources as a new participant in ancillary service markets,” *Energy strategy reviews*, vol. 18, pp. 106–120, 2017.
- [33] A. D. Papalexopoulos and P. E. Andrianesis, “Performance-based pricing of frequency regulation in electricity markets,” *IEEE Transactions on Power systems*, vol. 29, no. 1, pp. 441–449, 2012.
- [34] M. Braun, *Provision of Ancillary Services by Distributed Generators: Technological and Economic Perspective*. Erneuerbare Energien und Energieeffizienz, Kassel University Press, 2009.
- [35] E. Ela, V. Gevorgian, A. Tuohy, B. Kirby, M. Milligan, and M. O’Malley, “Market designs for the primary frequency response ancillary service—part i: Motivation and design,” *IEEE Transactions on Power Systems*, vol. 29, no. 1, pp. 421–431, 2013.
- [36] Y. G. Rebours, D. S. Kirschen, M. Trotignon, and S. Rossignol, “A survey of frequency and voltage control ancillary services—part ii: Economic features,” *IEEE Transactions on power systems*, vol. 22, no. 1, pp. 358–366, 2007.
- [37] R. Chakraborty, A. Chakraborty, E. Farantatos, M. Patel, H. Hooshyar, and A. Darvishi, “Hierarchical frequency and voltage control using prioritized utilization of inverter based resources,” *International Journal of Electrical Power & Energy Systems*, vol. 144, p. 108527, 2023.
- [38] P. Denholm, M. O’Connell, G. Brinkman, and J. Jorgenson, “Overgeneration from solar energy in california. a field guide to the duck chart,” 11 2015.
- [39] N. Jaleeli and L. S. VanSlyck, “Nerc’s new control performance standards,” *IEEE Transactions on Power Systems*, vol. 14, no. 3, pp. 1092–1099, 1999.
- [40] M. Yao, R. R. Shoults, and R. Kelm, “AGC logic based on NERC’s new control performance standard and disturbance control standard,” *IEEE Transactions on Power Systems*, vol. 15, no. 2, pp. 852–857, 2000.

- [41] P. Vorobev, D. M. Greenwood, J. H. Bell, J. W. Bialek, P. C. Taylor, and K. Turitsyn, “Deadbands, droop, and inertia impact on power system frequency distribution,” *IEEE Transactions on Power Systems*, vol. 34, no. 4, pp. 3098–3108, 2019.
- [42] E. Ekomwenrenren, “Co-simulation and stability analysis of the cyber-physical power grid,” Master’s thesis, University of Leeds, School of Electronic and Electrical Engineering, 2017.
- [43] S. Baros, Y. C. Chen, and S. V. Dhople, “Examining the economic optimality of automatic generation control,” *IEEE Transactions on Power Systems*, vol. 36, no. 5, pp. 4611–4620, 2021.
- [44] A. N. Venkat, I. A. Hiskens, J. B. Rawlings, and S. J. Wright, “Distributed mpc strategies with application to power system automatic generation control,” vol. 16, no. 6, pp. 1192–1206, 2008.
- [45] A. M. Ersdal, L. Imsland, and K. Uhlen, “Model predictive load-frequency control,” vol. 31, no. 1, pp. 777–785, 2015.
- [46] J. Köhler, M. A. Müller, N. Li, and F. Allgöwer, “Real time economic dispatch for power networks: A distributed economic model predictive control approach,” (Melbourne, Australia), pp. 6340–6345, 2017.
- [47] P. R. B. Monasterios and P. Trodden, “Low-complexity distributed predictive automatic generation control with guaranteed properties,” vol. 8, no. 6, pp. 3045–3054, 2017.
- [48] N. Li, C. Zhao, and L. Chen, “Connecting automatic generation control and economic dispatch from an optimization view,” vol. 3, pp. 254–264, Sept. 2016.
- [49] D. Apostolopoulou, P. W. Sauer, and A. D. Domuez-García, “Balancing authority area model and its application to the design of adaptive AGC systems,” vol. 31, no. 5, pp. 3756–3764, 2016.
- [50] L. Olmos, J. I. de la Fuente, J. Z. Macho, R. R. Pecharromán, A. M. Calmarza, and J. Moreno, “New design for the spanish agc scheme using an adaptive gain controller,” *IEEE Transactions on Power Systems*, vol. 19, no. 3, pp. 1528–1537, 2004.
- [51] L. Dong, Y. Tang, H. He, and C. Sun, “An event-triggered approach for load frequency control with supplementary adp,” *IEEE Transactions on Power Systems*, vol. 32, no. 1, pp. 581–589, 2016.

- [52] A. Pappachen and A. P. Fathima, “Critical research areas on load frequency control issues in a deregulated power system: A state-of-the-art-of-review,” *Renewable and Sustainable Energy Reviews*, vol. 72, pp. 163–177, 2017.
- [53] B. D. Anderson *et al.*, “Failures of adaptive control theory and their resolution,” *Communications in Information & Systems*, vol. 5, no. 1, pp. 1–20, 2005.
- [54] E. Dall-Anese, C. Zhao, S. Guggilam, S. V. Dhople, Y. C. Chen, and C. Zhao, “Engineering inertial and primary-frequency response for distributed energy resources,” tech. rep., National Renewable Energy Lab.(NREL), Golden, CO (United States), 2017.
- [55] V. Gevorgian, Y. Zhang, and E. Ela, “Investigating the impacts of wind generation participation in interconnection frequency response,” *IEEE transactions on Sustainable Energy*, vol. 6, no. 3, pp. 1004–1012, 2014.
- [56] A. Kyriacou, P. Demetriou, C. Panayiotou, and E. Kyriakides, “Controlled islanding solution for large-scale power systems,” *IEEE Transactions on Power Systems*, vol. 33, no. 2, pp. 1591–1602, 2017.
- [57] P. Wall, N. Shams, V. Terzija, V. Hamidi, C. Grant, D. Wilson, S. Norris, K. Maleka, C. Booth, Q. Hong, *et al.*, “Smart frequency control for the future gb power system,” pp. 1–6, 2016.
- [58] A. M. Prostejovsky, M. Marinelli, M. Rezkalla, M. H. Syed, and E. Guillo-Sansano, “Tuningless load frequency control through active engagement of distributed resources,” *IEEE Transactions on Power Systems*, vol. 33, no. 3, pp. 2929–2939, 2017.
- [59] W. Liu, G. Geng, Q. Jiang, H. Fan, and J. Yu, “Model-free fast frequency control support with energy storage system,” *IEEE Transactions on Power Systems*, vol. 35, no. 4, pp. 3078–3086, 2019.
- [60] P. Hidalgo-Gonzalez, R. Henriquez-Auba, D. S. Callaway, and C. J. Tomlin, “Frequency regulation using data-driven controllers in power grids with variable inertia due to renewable energy,” in *IEEE Power & Energy Society General Meeting*, 2019.
- [61] F. Dorfler, J. Coulson, and I. Markovsky, “Bridging direct & indirect data-driven control formulations via regularizations and relaxations,” *IEEE Transactions on Automatic Control*, vol. 68, no. 2, pp. 883–897, 2022.

- [62] C. Chen, M. Cui, F. Li, S. Yin, and X. Wang, “Model-free emergency frequency control based on reinforcement learning,” *IEEE Transactions on Industrial Informatics*, vol. 17, no. 4, pp. 2336–2346, 2020.
- [63] T. Yu, B. Zhou, K. W. Chan, L. Chen, and B. Yang, “Stochastic optimal relaxed automatic generation control in non-markov environment based on multi-step  $Q(\lambda)$  learning,” *IEEE Transactions on Power Systems*, vol. 26, no. 3, pp. 1272–1282, 2011.
- [64] Z. Yan and Y. Xu, “Data-driven load frequency control for stochastic power systems: A deep reinforcement learning method with continuous action search,” *IEEE Transactions on Power Systems*, vol. 34, no. 2, pp. 1653–1656, 2018.
- [65] Z. Yan and Y. Xu, “A multi-agent deep reinforcement learning method for cooperative load frequency control of a multi-area power system,” *IEEE Transactions on Power Systems*, vol. 35, no. 6, pp. 4599–4608, 2020.
- [66] J. Coulson, J. Lygeros, and F. Dörfler, “Data-enabled predictive control: In the shallows of the deepc,” in *2019 18th European Control Conference (ECC)*, pp. 307–312, IEEE, 2019.
- [67] L. Buşoniu, T. de Bruin, D. Tolić, J. Kober, and I. Palunko, “Reinforcement learning for control: Performance, stability, and deep approximators,” *Annual Reviews in Control*, vol. 46, pp. 8–28, 2018.
- [68] I. Markovskiy and P. Rapisarda, “Data-driven simulation and control,” *International Journal of Control*, vol. 81, no. 12, pp. 1946–1959, 2008.
- [69] C. De Persis and P. Tesi, “Formulas for data-driven control: Stabilization, optimality, and robustness,” *IEEE Transactions on Automatic Control*, vol. 65, no. 3, pp. 909–924, 2019.
- [70] J. C. Willems, P. Rapisarda, I. Markovskiy, and B. L. De Moor, “A note on persistency of excitation,” *Systems & Control Letters*, vol. 54, no. 4, pp. 325–329, 2005.
- [71] J. C. Willems and J. W. Polderman, *Introduction to mathematical systems theory: a behavioral approach*, vol. 26. Springer Science & Business Media, 1997.
- [72] M. Morari and E. Zafiriou, *Robust process control*. Chemical Engineering Research and Design, Prentice Hall, 1987.
- [73] E. Davison, “The robust control of a servomechanism problem for linear time-invariant multivariable systems,” vol. 21, no. 1, pp. 25–34, 1976.

- [74] A. Isidori, *Lectures in feedback design for multivariable systems*, vol. 3. Springer, 2017.
- [75] W. S. Levine, *The Control Systems Handbook: Control System Advanced Methods*. CRC press, 2018.
- [76] P. M. Anderson and M. Mirheydar, “A low-order system frequency response model,” vol. 5, no. 3, pp. 720–729, 1990.
- [77] H. Min, F. Paganini, and E. Mallada, “Accurate reduced order models for coherent synchronous generators,” in *2019 57th Annual Allerton Conference on Communication, Control, and Computing (Allerton)*, pp. 316–317, IEEE, 2019.
- [78] U. Markovic, Z. Chu, P. Aristidou, and G. Hug, “Lqr-based adaptive virtual synchronous machine for power systems with high inverter penetration,” *IEEE Transactions on Sustainable Energy*, vol. 10, no. 3, pp. 1501–1512, 2018.
- [79] J. Veenman, C. W. Scherer, and H. Köroğlu, “Robust stability and performance analysis based on integral quadratic constraints,” vol. 31, pp. 1–32, 2016.
- [80] F. Dörfler and F. Bullo, “Kron reduction of graphs with applications to electrical networks,” vol. 60, no. 1, pp. 150–163, 2012.
- [81] D. K. Molzahn, F. Dörfler, H. Sandberg, S. H. Low, S. Chakrabarti, R. Baldick, and J. Lavaei, “A survey of distributed optimization and control algorithms for electric power systems,” vol. 8, no. 6, pp. 2941–2962, 2017.
- [82] S. Teleke, M. E. Baran, S. Bhattacharya, and A. Q. Huang, “Rule-based control of battery energy storage for dispatching intermittent renewable sources,” *IEEE Transactions on Sustainable Energy*, vol. 1, no. 3, pp. 117–124, 2010.
- [83] H. Xin, Y. Liu, Z. Wang, D. Gan, and T. Yang, “A new frequency regulation strategy for photovoltaic systems without energy storage,” *IEEE Transactions on Sustainable Energy*, vol. 4, no. 4, pp. 985–993, 2013.
- [84] A. F. Hoke, M. Shirazi, S. Chakraborty, E. Muljadi, and D. Maksimovic, “Rapid active power control of photovoltaic systems for grid frequency support,” *IEEE Journal of Emerging and Selected Topics in Power Electronics*, vol. 5, no. 3, pp. 1154–1163, 2017.
- [85] B. Pal and B. Chaudhuri, *Robust control in power systems*. Springer Science & Business Media, 2006.

- [86] L. Ljung, T. Chen, and B. Mu, “A shift in paradigm for system identification,” *International Journal of Control*, vol. 93, no. 2, pp. 173–180, 2020.
- [87] I. Markovskiy and F. Dörfler, “Behavioral systems theory in data-driven analysis, signal processing, and control,” *Annual Reviews in Control*, vol. 52, pp. 42–64, 2021.
- [88] G. Bianchin, M. Vaquero, J. Cortés, and E. Dall’Anese, “Data-driven synthesis of optimization-based controllers for regulation of unknown linear systems,” in *IEEE Conf. on Decision and Control*, (Austin, TX, USA), pp. 5783–5788, 2021.
- [89] G. H. Golub and C. F. Van Loan, *Matrix computations*. JHU press, 2013.
- [90] E. Ekomwenrenren, Z. Tang, J. W. Simpson-Porco, E. Farantatos, M. Patel, and H. Hooshyar, “Hierarchical coordinated fast frequency control using inverter-based resources,” *IEEE Transactions on Power Systems*, vol. 36, no. 6, pp. 4992–5005, 2021.
- [91] T. Söderström and P. Stoica, *System identification*. Prentice-Hall International, 1989.
- [92] L. Ljung, *System Identification: Theory for the User*. Upper Saddle River, NJ: Prentice-Hall, 1999.
- [93] R. W. Wies, J. W. Pierre, and D. J. Trudnowski, “Use of ARMA block processing for estimating stationary low-frequency electromechanical modes of power systems,” *IEEE Transactions on Power Systems*, vol. 18, no. 1, pp. 167–173, 2003.
- [94] N. Zhou, J. W. Pierre, and J. F. Hauer, “Initial results in power system identification from injected probing signals using a subspace method,” *IEEE Transactions on Power Systems*, vol. 21, no. 3, pp. 1296–1302, 2006.
- [95] L. Huang, J. Coulson, J. Lygeros, and F. Dörfler, “Decentralized data-enabled predictive control for power system oscillation damping,” *IEEE Transactions on Control Systems Technology*, vol. 30, no. 3, pp. 1065–1077, 2021.
- [96] J. W. Simpson-Porco, F. Dörfler, and F. Bullo, “Synchronization and power sharing for droop-controlled inverters in islanded microgrids,” *Automatica*, vol. 49, no. 9, pp. 2603–2611, 2013.
- [97] M. Andreasson, D. V. Dimarogonas, K. H. Johansson, and H. Sandberg, “Distributed vs. centralized power systems frequency control,” in *2013 European Control Conference (ECC)*, pp. 3524–3529, IEEE, 2013.

- [98] M. Andreasson, H. Sandberg, D. V. Dimarogonas, and K. H. Johansson, “Distributed integral action: Stability analysis and frequency control of power systems,” in *2012 IEEE 51st IEEE Conference on Decision and Control (CDC)*, pp. 2077–2083, IEEE, 2012.
- [99] A. E. Leon, “Short-term frequency regulation and inertia emulation using an mmc-based mtdc system,” *IEEE Transactions on Power Systems*, vol. 33, no. 3, pp. 2854–2863, 2017.
- [100] O. D. Adeuyi, M. Cheah-Mane, J. Liang, and N. Jenkins, “Fast frequency response from offshore multiterminal vsc–hvdc schemes,” *IEEE Transactions on Power Delivery*, vol. 32, no. 6, pp. 2442–2452, 2016.
- [101] D. Yang, J. Kim, Y. C. Kang, E. Muljadi, N. Zhang, J. Hong, S.-H. Song, and T. Zheng, “Temporary frequency support of a dfig for high wind power penetration,” *IEEE Transactions on Power Systems*, vol. 33, no. 3, pp. 3428–3437, 2018.
- [102] Y. Tan, K. M. Muttaqi, P. Ciufu, L. Meegahapola, X. Guo, B. Chen, and H. Chen, “Enhanced frequency regulation using multilevel energy storage in remote area power supply systems,” *IEEE Transactions on Power Systems*, vol. 34, no. 1, pp. 163–170, 2018.
- [103] C.-T. Chen, *Linear system theory and design*. Saunders college publishing, 1984.

# APPENDICES

# Appendix A

## Proofs

### A.1 Proofs From Section 3

*Proof of Proposition 3.2.1:* A minimal state-space realization of an  $n$ -step time delay has matrices of the general form

$$A_m = \begin{bmatrix} 0 & \cdots & \cdots & 0 \\ I & \ddots & 0 & \vdots \\ & \ddots & \ddots & \vdots \\ & & I & 0 \end{bmatrix}, \quad B_m = \begin{bmatrix} I \\ 0 \\ \vdots \\ 0 \end{bmatrix}, \quad C_m = \begin{bmatrix} 0 \\ \vdots \\ 0 \\ I \end{bmatrix}^T,$$

Note that all eigenvalues of  $A_m$  are zero. By the PBH test [74], detectability of  $(C, A)$  is equivalent to the matrix  $M := \begin{bmatrix} A - \lambda I \\ C \end{bmatrix}$  having full rank for all  $\lambda \in \mathbb{C}$  with  $|\lambda| \geq 1$ . Direct substitution yields

$$M = \begin{bmatrix} A - \lambda I & B_2 & B_1 C_c & 0 \\ 0 & (1 - \lambda) & 0 & 0 \\ 0 & 0 & \mathcal{G}_1 & 0 \\ \begin{bmatrix} C \\ 0 \\ \vdots \\ 0 \end{bmatrix} & 0 & 0 & \mathcal{G}_2 \\ 0 & 0 & 0 & [0 \ 0 \ \cdots \ 0 \ I] \end{bmatrix}$$

where

$$\mathcal{G}_1 = \mathcal{G}_2 := \begin{bmatrix} -\lambda I & 0 & \cdots & 0 \\ I & -\lambda I & \ddots & \vdots \\ \vdots & \ddots & \ddots & 0 \\ 0 & \cdots & I & -\lambda I \end{bmatrix}.$$

Using elementary row operations on the sub-matrices comprising of the 4<sup>th</sup> and 5<sup>th</sup> rows of  $M$ , we obtain

$$M \sim \begin{bmatrix} A - \lambda I & B_3 & B_1 C_c & 0 \\ 0 & (1 - \lambda) & 0 & 0 \\ 0 & 0 & \mathcal{G}_1 & 0 \\ C & 0 & 0 & 0 \\ 0 & 0 & 0 & I \end{bmatrix}.$$

Similarly,  $[0 \ 0 \ \mathcal{G}_1 \ 0]$  can be row reduced to  $[0 \ 0 \ I \ 0]$ . By further interchanging the rows of the matrix, we obtain

$$M \sim \begin{bmatrix} A - \lambda I & B_2 & B_1 C_c & 0 \\ C & 0 & 0 & 0 \\ 0 & (1 - \lambda)I & 0 & 0 \\ 0 & 0 & I & 0 \\ 0 & 0 & 0 & I \end{bmatrix}$$

If  $\lambda \neq 1$  but  $|\lambda| > 1$ , then the columns of the matrix are linearly independent if and only if  $\begin{bmatrix} A - \lambda I \\ C \end{bmatrix}$  has full rank, which holds since  $A$  is Schur stable. If  $\lambda = 1$ , then  $M$  has full rank if and only if the submatrix  $\begin{bmatrix} A - I & B_2 \\ C & 0 \end{bmatrix}$  has full rank, which holds by assumption.  $\square$

*Proof of Theorem 3.2.3:* Let  $e_i = \widehat{\Delta P}_{u,i} - \Delta P_{u,i}$  denote the local estimation error with  $e$  and  $\Delta P_u$  denoting the stacked vectors of errors and net-load disturbances. At the sampling instants, the closed-loop system with disturbance input  $\Delta P_u$  and estimation error output  $e$  is described by a state-space model  $(A_F, B_F, C_F, D_F)$  where  $A_F$  is Schur stable, with associated  $N \times N$  BIBO stable transfer matrix  $H(z) = C_F(zI - A_F)^{-1}B_F + D_F$ . It follows from the final value theorem that

$$\lim_{k \rightarrow \infty} e^k = \lim_{z \rightarrow 1} \frac{z-1}{z} H(z) \frac{z}{z-1} \Delta P_u = H(1) \Delta P_u.$$

We conclude that  $\widehat{\Delta P}_{u,i}^k \rightarrow \Delta P_{u,i}$  as  $k \rightarrow \infty$  for each  $i \in \mathcal{A}$  and for any constant disturbances  $\Delta P_{u,i}$  if and only if  $H(1) = 0$ . Define the Rosenbrock matrix  $R(z) = \begin{bmatrix} zI - A_F & -B_F \\ C_F & D_F \end{bmatrix}$ ,

and note the simple identity

$$\begin{bmatrix} I & 0 \\ -C_F(I - A_F)^{-1} & I \end{bmatrix} R(1) = \begin{bmatrix} I - A_F & -B_F \\ 0 & H(1) \end{bmatrix},$$

where the first matrix on the left is invertible (and well-defined since  $A_F$  is Schur stable). Since  $I - A_F$  is invertible, it follows that  $H(1) = 0$  if and only if  $\text{rank}(R(1)) = \text{size}(A_F)$ . Therefore, to establish our claim, we are going to show that  $R(z)$  drops rank by  $N$  at  $z = 1$ .

Consider now the estimator (3.8) designed for the augmented dynamic LCA model (3.7). Without loss of generality, we neglect communication delays and remove the associated states. To further simplify the remainder of the proof, we neglect any IBR dynamics, which further implies that  $B_i^1 = -B_i^2$ . Under these assumptions, the estimator is written as

$$\begin{bmatrix} \Delta \hat{x}_i^{k+1} \\ \Delta \hat{P}_{u,i}^{k+1} \end{bmatrix} = A_{o,i} \begin{bmatrix} \Delta \hat{x}_i^k \\ \Delta \hat{P}_{u,i}^k \end{bmatrix} + B_{o,i} \begin{bmatrix} \Delta P_{\text{tie},i}^k \\ \Delta P_{\text{ibr,tot},i}^k \end{bmatrix} - \begin{bmatrix} L_i^1 \\ L_i^2 \end{bmatrix} \Delta \bar{y}_i^k$$

where

$$A_{o,i} = \begin{bmatrix} A_i & B_i^2 \\ 0 & 1 \end{bmatrix} + \begin{bmatrix} L_i^1 \\ L_i^2 \end{bmatrix} [C_i \ 0], \quad B_{o,i} = \begin{bmatrix} B_i^2 & B_i^1 \\ 0 & 0 \end{bmatrix}$$

We let  $C_{o,i} = [0 \ 1]$ . The interconnected power system from the setup is represented as

$$\begin{aligned} \Delta x_p^{k+1} &= A_p \Delta x_p^k + \sum_{i \in \mathcal{S}} B_{p_i} (\Delta \hat{P}_{u,i}^k - \Delta P_{u,i}) \\ \Delta y_{p,i}^k &= (\Delta P_{\text{tie},i}^k, \Delta \bar{y}_i^k) = \begin{bmatrix} C_{p_i}^1 \\ C_{p_i}^2 \end{bmatrix} \Delta x_p^k, \end{aligned}$$

where we have made explicit the measurements used by the local estimators. Combining the equations, the closed-loop system matrices are given by

$$\begin{aligned} A_F &= \begin{bmatrix} A_p & [0 \ B_{p1}] & \cdots & [0 \ B_{pN}] \\ B_{e1} & A_{e1} & \cdots & \vdots \\ \vdots & \vdots & \ddots & 0 \\ B_{eN} & 0 & 0 & A_{eN} \end{bmatrix}, \quad D_F = -I_N \\ B_F &= \begin{bmatrix} -B_{p1} & \cdots & -B_{pN} \\ 0 & 0 & 0 \\ \vdots & \vdots & \vdots \\ 0 & 0 & 0 \end{bmatrix}, \quad C_F = \begin{bmatrix} 0 & C_{o1} & \cdots & 0 \\ 0 & \vdots & \ddots & \vdots \\ 0 & 0 & \cdots & C_{oN} \end{bmatrix} \end{aligned}$$

where  $B_{e_i} = \begin{bmatrix} B_i^2 \\ 0 \end{bmatrix} C_{p_i}^1 - \begin{bmatrix} L_i^1 \\ L_i^2 \end{bmatrix} C_{p_i}^2$  and

$$A_{e_i} = A_{o,i} + \begin{bmatrix} B_i^1 \\ 0 \end{bmatrix} C_{o_i} = \begin{bmatrix} A_i + L_i^1 C_i & 0 \\ L_i^2 C_i & 1 \end{bmatrix},$$

where we have used that  $B_i^1 = -B_i^2$ . Substitution now shows that  $R(1)$  is given by

$$\left[ \begin{array}{cccc|ccc} I - A_p & [0 \ -B_{p_1}] & \cdots & [0 \ -B_{p_N}] & B_{p_1} & \cdots & B_{p_N} \\ -B_{e_1} & J_1 & \cdots & 0 & 0 & \cdots & 0 \\ \vdots & \vdots & \ddots & 0 & \vdots & \vdots & \vdots \\ -B_{e_N} & 0 & 0 & J_N & 0 & 0 & 0 \\ \hline 0 & [0 \ 1] & \cdots & 0 & -1 & \cdots & 0 \\ 0 & \vdots & \ddots & \vdots & \cdots & \ddots & \vdots \\ 0 & 0 & \cdots & [0 \ -1] & 0 & \cdots & -1 \end{array} \right]$$

where  $J_i = I - A_{e_i} = \begin{bmatrix} I - (A_i + L_i^1 C_i) & 0 \\ L_i^2 C_i & 0 \end{bmatrix}$ . By direct inspection, the third block column of the above is  $-1$  times the  $2N + 2$ nd block column, the fifth block column is  $-1$  times  $2N + 3$ rd block column, and so forth. It follows that the final  $N$  columns are redundant, which completes the proof.  $\square$

## A.2 Proofs From Section 4

*Proof of Theorem 4.1.2:* Under the stated assumptions of controllability, input data persistency of excitation of order  $T_{\text{ini}} + 1 + n(\mathcal{B})$ , and sufficient initialization length  $T_{\text{ini}} \geq \ell(\mathcal{B})$ , it follows from [68, Prop. 6] that the output predictor (4.6a) produces precisely the same values  $\hat{y}(t)$  as the LTI system

$$\begin{aligned} \hat{x}(t+1) &= A\hat{x}(t) + Bu(t) + B_d \hat{d}(t) \\ \hat{y}(t) &= C\hat{x}(t) + Du(t) \end{aligned} \tag{A.1}$$

where the matrices may be taken to be the same as those in (4.1). The disturbance estimator (4.6) may therefore be expressed as (A.1) with (4.6b), which we rewrite together as

$$\begin{aligned} \begin{bmatrix} \hat{x}(t+1) \\ \hat{d}(t+1) \end{bmatrix} &= \underbrace{\begin{bmatrix} A & B_d \\ 0 & I_q \end{bmatrix}}_{:=\mathcal{A}} \begin{bmatrix} \hat{x}(t) \\ \hat{d}(t) \end{bmatrix} + \begin{bmatrix} B \\ 0 \end{bmatrix} u(t) - \underbrace{\begin{bmatrix} 0 \\ \varepsilon L \end{bmatrix}}_{:=\varepsilon\mathcal{L}} (\hat{y}(t) - y(t)) \\ \hat{y}(t) &= \underbrace{\begin{bmatrix} C & 0 \end{bmatrix}}_{:=\mathcal{C}} \begin{bmatrix} \hat{x}(t) \\ \hat{d}(t) \end{bmatrix} + Du(t) \end{aligned}$$

where  $y(t)$  is the measured output of (4.1). The above has the form of a Luenberger observer, and standard estimation error analysis (e.g., [103]) implies that we will have  $\hat{d}(t) \rightarrow d(t)$  exponentially, and irrespective of the initial conditions, if

$$\mathcal{A} - \varepsilon \mathcal{L}C = \begin{bmatrix} A & B_d \\ -\varepsilon LC & I_q \end{bmatrix}$$

is Schur stable. Recall that, by assumption,  $A$  is Schur stable, so  $I_n - A$  is invertible; based on this define the invertible matrix

$$T = \begin{bmatrix} I_n & (I_n - A)^{-1}B_d \\ 0 & I_q \end{bmatrix}.$$

By similarity,  $\mathcal{A} - \varepsilon \mathcal{L}C$  is Schur stable if and only if  $\mathcal{M}(\varepsilon) := T(\mathcal{A} - \varepsilon \mathcal{L}C)T^{-1}$  is as well. Simple calculations show that  $\mathcal{M}(\varepsilon)$  evaluates to

$$\mathcal{M}(\varepsilon) = \begin{bmatrix} A + \varepsilon M_1 & \varepsilon M_2 \\ \varepsilon M_3 & I_q - \varepsilon LG(1) \end{bmatrix},$$

where  $M_1, M_2, M_3$  are constant matrices and  $G(1) = C(I_n - A)^{-1}B_d$ . By assumption,  $G(1)$  has full column rank and  $L = G(1)^\dagger$ ; thus, we have that  $LG(1) = I_q$ , and the (2, 2) block of the above simplifies to  $(1 - \varepsilon)I_q$ . Since  $A$  is Schur stable, by standard linear Lyapunov theory there exists a matrix  $P \succ 0$  such that  $A^\top P A - P \prec 0$ . Defining  $\mathcal{P} = \text{diag}(P, I_q)$ , straightforward calculations and a use of the Schur complement lemma show that  $\mathcal{M}(\varepsilon)^\top \mathcal{P} \mathcal{M}(\varepsilon) - \mathcal{P} \prec 0$  for all sufficiently small  $\varepsilon > 0$ , which establishes that  $\mathcal{M}(\varepsilon)$  is Schur stable and completes the proof.  $\square$

## Appendix B

### Example to Clarify the Allocation Based on Electrical Distance in Section 3.3.2

Let the grid below represent the electrical distances between 3 hypothetical LCAs.

Electrical distance  
(Impedance)  
A1   A2   A3

Area 1	0	10	20
Area 2	10	0	30
Area 3	20	30	0

Assume that Area 2 is the disturbed area, with estimated disturbances given as

$$\Delta \hat{P}_{u,1} = 2 \text{ MW}, \quad \Delta \hat{P}_{u,2} = 60 \text{ MW}, \quad \Delta \hat{P}_{u,3} = 0.1 \text{ MW}, \quad \text{and} \quad \sum_{k \in \mathcal{A}} \Delta \hat{P}_{u,k} = 62.1 \text{ MW}.$$

Here  $w_j$  for each area  $j$  in the 3-area system are computed as

$$w_1 = \frac{2}{62.1} = 0.032, \quad w_2 = \frac{60}{62.1} = 0.966, \quad w_3 = \frac{0.1}{62.1} = 0.002.$$

The weights in the objective function of (3.12) are then

$$\begin{aligned}q_1 &= 0 \times 0.032 + 10 \times 0.966 + 20 \times 0.002 = 9.7, \\q_2 &= 0.38, \\q_3 &= 29.62.\end{aligned}$$

Therefore, (3.12a) becomes

$$9.7a_1^2 + 0.38a_2^2 + 29.62a_3^2$$

Since Area 2 is the contingent area, whose resources have been maxed out, the majority of the extra supply will be sourced from area 1, which has the lowest weight in the cost function because it is electrically closest to the contingent area.